Noise dynamics in multi-Stokes Brillouin laser

Ananthu Sebastian

UNIVERSITÉ DE RENNES 1

THESE DE DOCTORAT DE

L'UNIVERSITE DE RENNES 1

ECOLE DOCTORALE N° 596
Matière, Molécules, Matériaux
Spécialité : « *Photonique* »

Par
Ananthu SEBASTIAN

Noise dynamics in multi-Stokes Brillouin laser

Thèse présentée et soutenue à Lannion, le 18 décembre 2020
Unité de recherche : INSTITUT FOTON (UMR 6082/CNRS)

Rapporteurs avant soutenance :

Yves JAOUEN Professeur, Telecom Paris Tech
Olivier LLOPIS Directeur de recherche CNRS, LAAS-CNRS

Composition du Jury :

Présidente :	Medhi ALOUINI	Professeur, Université de Rennes 1/ Institut Foton
Examinateurs :	Anne AMY-KLEIN	Professeure, Université Sorbonne Paris Nord/ LPL
	Jean-Charles BEUGNOT	Chargé de recherche, Institut Femto-ST
	Carlos ALONSO-RAMOS	Chargé de recherche CNRS, C2N
Dir. de thèse :	Pascal BESNARD	Professeur, ENSSAT(Université de Rennes1)/ Institut Foton
Co-dir. de thèse :	Stéphane TREBAOL	Maitre de conférences, ENSSAT(Université de Rennes1)/ Institut Foton

Acknowledgement

I would like to extend my sincere gratitude towards the remarkable individuals who have supported and helped me throughout my PhD at Institut FOTON. It has been a time of intense learning for me, not only in the scientific field but also on a personal level.

First and foremost, I wish to thank my principal supervisor Pascal BESNARD for giving me the opportunity to pursue my PhD at the University of Rennes1, France. His excellent guidance, confidence, supervision and continuous encouragement have been a constant inspiration that made so many things possible throughout my research. Pascal always trusted me and find time to discuss during heavy administrative tasks incumbent on him. In addition, I would like to thank my co-supervisor, Stephane TREBAOL for his guidance, friendship, and extended support in the course of my research. All my supervisor's motivation and immense knowledge always helped me during my PhD and writing this thesis.

Besides supervisors, I would like to acknowledge my jury members Yves JAOUEN and Olivier LLOPIS for accepting to be the reporter of this manuscript. Many thanks for their very relevant remarks. I thank Anne AMY-KLEIN from LPL, Jean-Charles BEUGNOT from Institut Femto-ST, Carlos ALONSO-RAMOS from C2N and Medhi ALOUINI from Institut Foton for their constructive questions during the defense.

With a special mention to Irina V Balakireva, who contributed the numerical simulations and theoretical model for noise analysis. I would like to acknowledge the valuable inputs from Schadrac Fresnel and Mohamed Omar Sahni, who contributed to many fruitful discussions and showed me all the details of experimental physics in the initial phase of my PhD, which always helped me to achieve valuable insights into Brillouin laser.

I would also like to thank all of the academic and support staff of the Institut FOTON and ENSSAT for their fruitful discussions and assistance throughout my research period. I would also thank all my colleagues and friends, Antoine Congar, Dominique

Mammez, Nessim Jebali, Joseph Slim, Georges Perin, Louis Ruel, Rasool Saleem and Amith Karuvath, who made my life simple, enjoyable and memorable at FOTON. It was a great pleasure to work with you and thank you so much for your friendship and for all the good times!

Finally, I could not conclude these thanks without having thought of my inspiring parents and sister, fantastically supportive family members, and my enchanting friends.

Thank you

Ananthu SEBASTIAN

Abstract

Stimulated Brillouin Scattering (SBS) is a coherent interaction process in which light is scattered from optically generated acoustic waves. It is a powerful tool for microwave and optical signal processing, distributed sensing and spectroscopy. Brillouin lasers are attracting a lot of interest for their ability to produce ultra coherent linewidths.

This thesis is devoted to the understanding of noise properties of Brillouin fiber ring lasers, operating with multiple Stokes orders. First, we present a technique based on the cavity ringdown method, which allows to characterize the Brillouin gain coefficient directly from probing the laser cavity. Its advantages are to obtain parameters from a single experiment with low optical powers (some 10 milliwatts) for short cavities (a few meters long, or integrated cavities).

Secondly, it is shown that an intrinsic linewidth of a few tens of mHz can be easily obtained by cascading two non-resonant Brillouin lasers (for which the pump performs a single pass inside the cavity). In order to obtain these results, the long-term stability has been improved by using a Pound-Drever-Hall servo loop, which allows us to compare our analytical and experimental results. Unfortunately, we were unable to explore the fundamental limits of noise reduction due to the noise floor of our bench.

Thirdly, one of the major works of this thesis is the theoretical and experimental study of the noise properties, including frequency noise and relative intensity noise, of a resonant Brillouin laser (for which pump and Stokes waves are resonant inside the cavity). In particular, the impacts of the fiber-ring-cavity quality factor, Brillouin gain detuning, are evaluated very precisely on the laser RIN features such as amplitude noise reduction and relaxation frequency.

We emphasize the fact that many characteristics of the frequency noise are related to the RIN properties by a coupling between intensity and phase. We show that the cascade process modifies the dynamics of the Brillouin laser when compared to those of a

single-mode Brillouin laser with a single first-order Stokes component. Our experimental results are in excellent agreement with our numerical simulations, obtained thanks to our non-linear system describing the operation of a multi-Stokes Brillouin laser. This good match is mainly due to our ability:

- to obtain very precise values of the cavity parameters and the Brillouin gain coefficient using the CRDM technique ;
- to achieve long-term stability (hours);
- to finely control the detuning between the laser Stokes resonance and the frequency of the Brillouin gain maximum.

We demonstrate experimentally for the first time that frequency noise is degraded in the presence of anti-Stokes Brillouin scattering. We also show that a gain detuning of the order of a few hundred kHz can degrade the intensity noise reduction or also increase the linewidth by amplitude-phase coupling. All these very fine observations thus allow us to set the fundamental limits of such laser systems such as: the increase in noise due to anti-Stokes orders; the role of pump noise and its possible interrelation with cavity finesse; the effect of the detuning inherent to higher Stokes orders.

All these conclusions are key to the design and engineering of these Brillouin fiber lasers, which are currently attracting a great deal of interest as evidenced by the work in progress in the scientific community. This PhD thesis contributes to a better understanding of multi-Stokes Brillouin lasers.

Keywords : Nonlinear optics, Stimulated Brillouin Scattering, Brillouin laser, frequency noise, relative intensity noise, laser linewidth, optical resonator, cavity ring down spectroscopy, frequency stabilization.

Résumé

La diffusion Brillouin stimulée (SBS) est un processus d'interaction cohérent, pour lequel la lumière est diffusée à partir des ondes acoustiques générées optiquement. C'est un outil puissant pour le traitement des micro-ondes et des signaux optiques, la détection distribuée et la spectroscopie. Les lasers Brillouin suscitent un très grand intérêt pour leur capacité à produire des largeurs de raie ultra cohérentes.

Cette thèse est consacrée à la compréhension des propriétés de bruit des lasers à fibre Brillouin en anneau, fonctionnant avec de multiples ordres de Stokes. Tout d'abord, nous présentons une technique basée sur la méthode de ringdown de la cavité, qui permet de caractériser le coefficient de gain Brillouin directement à partir du sondage de la cavité laser. Ses avantages sont d'obtenir des paramètres à partir d'une seule expérience avec de faibles puissances optiques (quelques 10 milliwatts) pour des cavités courtes (quelques mètres de long, ou cavités intégrées).

Deuxièmement, il est démontré qu'une largeur de raie intrinsèque de quelques dizaines de mHz peut être facilement obtenue en cascadant deux lasers Brillouin non résonants (pour lesquels la pompe effectue un seul passage à l'intérieur de la cavité). Afin d'obtenir ces résultats, la stabilité à long terme a été améliorée en utilisant une boucle d'asservissement de type Pound Drever Hall, ce qui nous permet de comparer nos résultats analytiques et expérimentaux. Malheureusement, nous n'avons pas exploré les limites fondamentales de la réduction du bruit en raison du plancher de bruit de notre banc de mesure.

Troisièmement, un des travaux majeurs de cette thèse est l'étude analytique et expérimentale des propriétés du bruit, y compris le bruit de fréquence et le bruit relatif d'intensité, d'un laser Brillouin résonant (pour lequel, les ondes de pompe et de Stokes sont résonantes à l'intérieur de la cavité). En particulier, les impacts du facteur de qualité de la cavité fibrée en anneau, le désaccord de gain Brillouin ont été évalués très précisément sur les caractéristiques du RIN du laser telles que la réduction de l'amplitude du

bruit et la fréquence de relaxation.

Nous soulignons le fait que de nombreuses caractéristiques du bruit de fréquence sont liées aux propriétés du RIN par un couplage entre l'intensité et la phase. Nous montrons que le processus en cascade modifie la dynamique du laser Brillouin par rapport à celle d'un laser Brillouin monomode avec une seule composante de Stokes de premier ordre. Nos résultats expérimentaux sont en excellent accord avec nos simulations, obtenues grâce à notre système non linéaire décrivant le fonctionnement d'un laser Brillouin multi-Stokes. Cette bonne concordance est principalement due à notre capacité :

- à obtenir des valeurs très précises des paramètres de la cavité et du coefficient de gain Brillouin en utilisant la technique CRDM ;
- à atteindre une stabilité à long terme (plusieurs dizaines d'heures) ;
- à contrôler finement le désaccord entre la résonance de Stokes du laser et la fréquence du maximum de gain Brillouin.

Nous démontrons expérimentalement pour la première fois que le bruit de fréquence est dégradé en présence d'une diffusion Brillouin anti-Stokes. Nous montrons également qu'un désaccord de gain de l'ordre de quelques centaines de kHz peut dégrader la réduction du bruit d'intensité ou également augmenter la largeur de raie par un couplage amplitude-phase. Toutes ces observations très fines nous permettent donc de fixer les limites fondamentales de tels systèmes laser comme : l'augmentation du bruit due aux ordres anti-Stokes ; le rôle du bruit de pompe et son interrelation possible avec la finesse de la cavité ; l'effet du désaccord inhérent aux ordres de Stokes plus élevés.

Toutes ces conclusions sont les clés de la conception et de l'ingénierie de ces lasers à fibre Brillouin, qui suscitent actuellement beaucoup d'intérêt comme en témoignent les travaux en cours dans la communauté scientifique. Cette thèse de doctorat contribue à une meilleure compréhension des lasers Brillouin multi-Stokes.

Mots clefs : Optique non linéaire, diffusion Brillouin stimulée, laser Brillouin, bruit de fréquence, bruit relatif d'intensité, largeur de raie laser, résonateur optique, spectroscopie cavity ring-down, stabilisation de fréquence.

Contents

List of Figures

List of Tables

Introduction

In 1922, Léon Brillouin theoretically predicted the scattering due to the interaction of the photons and acoustic waves (propagating density fluctuations) [6]. The experimental verification was difficult at that time due to the lack of coherent light source to efficiently generate an ultrasonic pressure wave. In 1930, Gross [7] experimentally proved the existence of photon and acoustics wave interaction. Gross was originally looking for the Raman scattering in organic liquids, but his measurements did not agree with Raman scattering. However it perfectly matched the theoretical predictions made by Brillouin. Note that Mandelstam predicted a similar scattering effect in 1926 [8]. Based on the work of Leon Brillouin, the inelastic scattering of the light from acoustic waves is referred as Brillouin scattering in literature.

The discovery of the laser (light amplification by stimulated emission of radiation) in the 1960s, revolutionized the study of fundamental physics by giving birth to new research like laser physics, nonlinear optics, etc. The lasers provide a coherent and powerful light source, that leads to changes in the material properties. Nowadays, lasers play vital role in telecommunication, medicine, defense, industry, environment, lightning ... In recent decades, different types of lasers have been developed in terms of optical power, coherency and wavelengths.

Soon after the first realization of a laser [9], Chaio and Townes observed, in 1964, stimulated Brillouin scattering (SBS) in quartz and sapphire [10]. After the invention of optical fibers, stimulated Brillouin scattering was first studied in 1972 by Ippen and Stolen [11]. Then SBS gained attention in telecommunication systems because it limits the performances by reflecting most of the power through the counter-propagating Stokes wave. It results in large depletion of pump power. On the contrary SBS can be used on purposes as optical amplifiers [12], lasers [13], filters [14, 15], and sensors [16, 17]. Informations from the SBS may give the mechanical properties of materials, which open

the field of Brillouin based bio-imaging [18, 19, 20]. In the past century, a tremendous amount of research was done concerning Brillouin scattering, especially in the last decades during which, SBS was observed in chip-scale structures [21, 22], and different materials like silica [11], chalcogenide [23], tellurium [24].

In 1976, Hill [13] realized a fiber laser based on Brillouin effects, which had the unique ability to reduce noise compared to that of the pump [25]. Later, different architectures of Brillouin lasers [26, 25, 27, 28, 29, 30, 31, 32] are studied. This low-noise laser is of interest to the scientific community for applications in microwave and optical signal processing, distributed sensors, spectroscopy, gyroscope, metrology. The noise properties of this laser are not well understood. In this thesis, we explain two Brillouin laser architectures: resonant and non-resonant Brillouin laser and their noise properties.

Objectives of the thesis

This thesis is devoted to the understanding of ring Brillouin fiber lasers, operating with multiple Stokes orders. Most of the work carried out during this thesis is part of the continuity of the works of Kenny Tow [33] and Schadrac Fresnel [34]. My work was accomplished in the framework of the SOLBO project (SOurces Laser Brillouin cOhérent à faible bruit) of the FUI call (Fonds Unique Interministériel AAP20) with the help of BPI France, the "Images et réseaux" cluster and in collaboration with IDIL Fibre Optiques (project leader), Lumibird, THALES, ISCR (Institut des Sciences Chimiques de Rennes), Photonics Bretagne.

The main objective was to design a low cost Brillouin fiber laser, with an integrated linewidth below kHz, by IDIL and also for the Foton Institute, to explore the physics of multi-Stokes Brillouin fiber lasers and to try to know the fundamental limitations of frequency noise reduction for these sources, whether for single or multiple Stokes order cavities. In this thesis, I propose

- a new Brillouin gain measurement technique, particularly adapted to short cavities and not requiring high optical pump powers (a few tens of milliWatts),
- a comparison of laser operation between resonant and non-resonant pumping,
- a modeling of our experimental results by an analytical approach, allowing us to explain the physical mechanisms of these lasers,

- a discussion of the fundamental limitations of these devices and their advantages.

Main results

Firstly, we will report a technique based upon the cavity ring-down method that enables the characterization of the Brillouin gain coefficient directly from probing the laser cavity. Material gain, optical cavity parameters, and lasing properties can be extracted from measurements within a single experiment. This method could be used to characterize an integrated microresonator Brillouin cavity. Secondly, we will study two different Brillouin designs, which are using resonant or non-resonant pumping. In non-resonant Brillouin laser, the pump is doing a single pass inside the cavity, and the generated Stokes wave are resonant inside the cavity. In order to increase the long-term stability of such scheme, we will propose a frequency stabilized non-resonant Brillouin fiber laser design, that enables us to compare our analytical and experimental results about frequency noise in a non-resonant Brillouin laser. The intrinsic linewidth of our non-resonant Brillouin laser is 1.3 Hz. Furthermore, we demonstrate experimentally that the intrinsic linewidth can be reduced down to 47 mHz by cascading two non-resonant Brillouin lasers, showing the ease and ability of such systems to produce low-noise light. Unfortunately, we did not succeeded to explore the fundamental limitations of noise reduction due to the noise floor of our bench.

A major work of this thesis is the investigation of noise properties of a resonant Brillouin laser. For resonant pumping, the pump and Stokes waves are resonant inside the cavity, which could produce multi-Stokes orders. We experimentally analyze, in this cascaded regime, steady-state optical powers and noise properties of the different signals, including frequency noise and relative intensity noise. Our experimental results reveal that the cascading process modifies the dynamics of Brillouin laser when compared to those of single-mode Brillouin laser with a single first order Stokes component.

We analytically and experimentally investigate the intensity noise of each Stokes wave and study the noise dynamics of the cascaded Brillouin scattering process. In particular we examine the impact of fiber ring quality factor on the laser RIN features such as amplitude-noise reduction and relaxation frequency. We also investigate the influence of the Brillouin gain detuning on the RIN reduction. This detailed study is important as many characteristics of frequency noise are related to RIN properties through a coupling

between intensity and phase.

The study of frequency noise dynamics of a multi-Stokes Brillouin fiber laser was done on a large mode-volume optical resonator with 2 m optical cavity, because this kind of cavity is less sensitive to acoustical and thermal fluctuations than micro-cavity. It will enable to reach lower flicker noise. With this cavity, we have reached an intrinsic linewidth of 12.8 Hz and less than 2 kHz integrated linewidth for 10 ms observation time.

Furthermore, we will experimentally demonstrate for the first time that the frequency noise is increased in the presence of anti-Stokes Brillouin scattering in the cascading process. We will also show that the gain detuning could enhance the linewidth by an amplitude-phase coupling. All these experimental results are in good agreement with our analytical calculations obtained through our nonlinear system for multi-Stokes Brillouin laser. This good match is mainly due to three facts:

1. we are able to get directly very precise values of cavity parameters and of the Brillouin gain coefficient using the CRDM technique;

2. we are able to reach long term stability (tens of hours);

3. we are able to finely control the detuning between the laser Stoke resonance and the frequency of Brillouin gain maximum.

All these very fine observations allow us to design and engineer Brillouin fiber lasers. We show some fundamental limitations of these systems in terms of noise reduction such as

- the role of pump noise, possibly in its interrelation with cavity finesse,

- anti-Stokes orders,

- the effect of detuning is inherent in higher Stokes orders.

Nevertheless, such systems are still very pervasive as evidenced by the interest they arouse in the scientific community. This Ph.D. thesis contributes to a better understanding of multi-Stokes Brillouin lasers.

Thesis organization

This thesis is organized into four chapters followed by a conclusion and some remarks. In chapter 1, we give a general introduction to the physics of laser noise necessary to understand the work of this manuscript. It also details the measurement technique for frequency noise and relative intensity noise (RIN) of laser. Moreover, we introduce fundamental ingredients of the laser stabilization methods, which have been used for the realization of Brillouin laser.

Chapter 2 begins by describing physical mechanisms behind the Brillouin scattering in optical fibers. We will briefly describe spontaneous and stimulated Brillouin scattering and will explain a new Brillouin gain characterization based on the cavity ring-down method (CRDM). We will also compare the results with conventional Brillouin gain characterization. This cavity ring-down method enables us to identify the different coupling regimes and estimate the Q-factor of the resonator. These measurements are fundamental to characterize Brillouin laser cavity and ease to design Brillouin cavity.

In chapter 3, we will describe a stabilized non-resonant Brillouin laser. The chapter begins with a historical overview of Brillouin lasers. This overview explores different laser designs and current state of the art of Brillouin lasers in fiber, integrated chip, and microresonator. Moreover, we address the issue of mode-hopping in non-resonant Brillouin laser and propose a frequency stabilization method based on Pound–Drever–Hall (PDH) locking. Also, we investigate the power and frequency noise characterization of non-resonant Brillouin laser. We show experimental frequency noise agreement to analytical results and corresponding laser linewidth are in the range of Hz level. We demonstrate that the cascading of two Brillouin lasers can reach the mHz linewidth.

In chapter 4, we will explore the physics of resonant Brillouin laser. We will discuss the power and noise dynamics of theses lasers with the help of our numerical and experimental results. RIN of resonant Brillouin lasers will be studied in terms of pumping power, photon lifetime, and gain detuning in the so-called single-mode and cascading regimes of the laser. We will show that our numerical simulations and experimental results are in good agreement. We will discuss some fundamental limitations of noise reduction linked to pump noise, Q-factor, anti-Stokes orders, gain detuning and amplitude phase-coupling.

Chapter 1

Noise in lasers

1.1 Introduction

Narrow linewidth lasers are of great importance for several areas, such as coherent optical telecommunications [35, 36], sensors [37], precision spectroscopy [38], optical atomic clocks [39, 40], frequency metrology [41, 42], LiDAR [43] and microwave photonics [44] to only name a few. My work is mainly focused on the development of low-noise Brillouin laser; the study of these lasers demonstrates that it is possible to produce a laser output with low-noises when compared to those of the pump laser. But before explaining this, it is necessary to introduce the theoretical and experimental basics of laser noises, which are available in many books [33, 34, 45, 46, 47, 48, 49, 50]. The object of this chapter is to introduce laser noises descriptions. The origin of the laser noise is defined and introduced, in section (1.2), by considering the amplitude and phase noises. In section (1.3), theory and experimental measurement methods are explained for laser relative intensity noise (RIN) while section (1.4) is dedicated to laser phase noise. Moreover, theoretical and experimental basics of the linewidth narrowing method, which is based upon laser frequency-stabilization on fiber ring cavity are introduced in section (1.5).

1.2 Origin of noise in lasers

In a laser, spontaneous emission plays an essential role in the generation of initial photons that leads to amplification by stimulated emission, and that will gives the laser emission. The spontaneous emission is a random process, which emits photons with

random direction, phase and polarization. These random fluctuations are called intrinsic or fundamental "noise" of the laser. These fluctuations may have a negative impact on numerous laser applications, more particularly in the field of metrology and optical sensors.

In presences of noise, the scalar electric field associated with the light wave, delivered by a single mode laser at the optical frequency of ν_0, is written:

$$E(t) = [E_0 + \delta E(t)]e^{i[2\pi\nu_0 t + \phi(t)]} \tag{1.1}$$

Where $\delta E(t)$ and $\phi(t)$ are temporal fluctuations of amplitude and phase. The representation is linked to the Fresnel vector in the complex plane (It is explained in appendix (A) [50]). The origin of these fluctuations can be classified into two categories: the first one is at the quantum level; this fundamental noise comes from the spontaneous emission process in lasers. The electromagnetic thermal radiation will also contribute to fluctuations. The second one is called technical noise; it may include several contributions as : acoustical and mechanical vibrations, temperature fluctuations or even the pump noise. Theses various random contributions lead to amplitude and phase noises that will be studied through their power spectral density (PSD).

PSD of a given random variable, $\delta b(t)$ (to be more general), will be the Fourier transform of its autocorrelation function $R_{\delta b}$. b can be either intensity or phase in the present study. The PSD can be written as $S_{\delta b}$:

$$S_{\delta b}(f) = \int_{-\infty}^{+\infty} R_{\delta b}(\tau)e^{-i2\pi f\tau}d\tau \tag{1.2}$$

with $R_{\delta b}$ being the autocorrelation function of $\delta b(t)$ defined by

$$R_{\delta b}(\tau) =< \delta b(t)\delta b(t-\tau) >= \int_{-\infty}^{+\infty} \delta b(t)\delta b(t-\tau)dt \tag{1.3}$$

Note that in Eq.(1.2) the frequencies of interest are mainly in the electrical domain [DC to a few GHz]. For that reason f may be used instead of ν to indicate low frequency components. It's why the measurements are carried out in the electrical field rather than in the optical field by an electrical spectrum analyzer (ESA). In the next sections, we will define amplitude and phase noises and explain the associated measurement methods to characterize them.

1.3 Relative intensity noise (RIN)

One of the objectives of this thesis is to study the intensity noise of a Brillouin laser experimentally and theoretically. In particular, we experimentally analyze the intensity noise of each Stokes wave generated through the Brillouin process. We examine the impact of the cavity parameters on the laser RIN features. In this section, we introduce the RIN principles and measurement method, some of the notations and explanations are taken from the following references [33, 34].

1.3.1 Definition of relative intensity noise

The emitted laser field (Eq.1.1) has temporal amplitude fluctuations; the related optical power as well:

$$P(t) = P_0 + \delta P(t) \tag{1.4}$$

where P_0 is the average power and $\delta P(t)$ is the temporal fluctuation of optical power. It describes the fluctuations of the optical power output of the laser around its average power of P_0. The intensity noise is obtained by dividing the optical power by the effective area, which is the illuminated surface. Then the laser relative intensity noise can be defined by taking a Fourier transform of $\delta P(t)$

$$RIN(f) = \frac{\langle \mid \delta P(f) \mid^2 \rangle}{P_0^2} \tag{1.5}$$

$\langle\rangle$ stands for statistical expectation. Thus the RIN is defined by the ratio of the power spectral density $S_{\delta P}$ [1] over the average optical power. $S_{\delta P}$ is the Fourier transform of the auto-correlation of $\delta P(t)$ and is related to the second moment of the noise forces. The definition can be taken in the electrical domain:

$$RIN(f) = \frac{S_{RIN}}{P_{ele}} \tag{1.6}$$

Where S_{RIN} is the electrical power spectral density. P_{ele} is average electrical power. The relation between optical power and electric power $P_{ele} = R{I_0}^2 = R\eta^2 P_0^2$; R is the load resistance of the photodetector. I_0 is the average photocurrent produced by the photodetector. η is the quantum efficiency of the photodetector. In the following, the RIN measurement method used in this manuscript is described.

[1] $S_{\delta P}$ can obtained from Eq (1.2) by considering the $R_{\delta P}(\tau) =< \delta P(t)\delta P(t-\tau) >$

1.3.2 RIN measurement method

At Institut FOTON, we study the intensity noise by a direct detection of PSD using an electrical spectrum analyzer [33, 34]. The experimental setup used to characterize the RIN of a laser during this thesis is shown in figure (1.1).

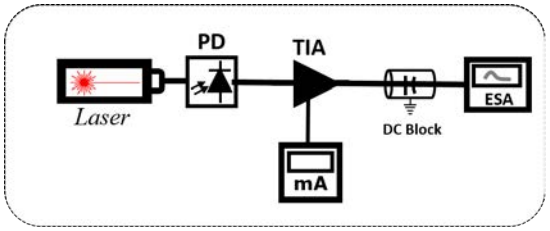

Figure 1.1: RIN measurement setup. The photocurrent from the photodetector is measured and amplified. Its DC component is blocked before its spectral analysis by the ESA. PD: photodetector, TIA: Transimpedance amplifier, ESA: Electrical spectrum analyzer.

The RIN detection system consists of a photodetector with a bandwidth from DC to 1 GHz, a trans-impedance amplifier (TIA) with a variable bandwidth depending on the gain, but not exceeding 200 MHz, and a "DC-Block" module with very low cut-off frequency (1 Hz), to remove the DC component of the electrical signal in order to avoid damaging the ESA. PSD is analyzed with the help of the ESA. The PSD collected on the ESA contains not only the PSD of the RIN but also that of thermal noise (S_T) and shot noise (S_{sh}). The PSD detected at the electric spectrum analyzer is then the sum of these three noise sources. As they are independent stochastic processes, the total PSD can be written as:

$$S_{Total} = S_T + S_{sh} + S_{RIN} \tag{1.7}$$

It is then necessary to measure the thermal and shot noise contributions in order to obtain the laser RIN. It will be explained in the next section.

1.3.3 Determination of thermal noise

Thermal noise S_T is independent of the optical signal received on the detector but depends on the devices in the measurement system (ESA, photodetector, amplifier). It is simply measured without an optical signal on photodetector. It consists of two main contributions: thermal noise (or Johnson noise or Johnson-Nyquist noise) and flicker, called also excess or $1/f$ noise. In the case of a photodetection system, even in the absence of

the incident signal, a current is generated by the movement of the charge carriers in the material due to thermal agitation. These current fluctuations induce thermal noise. The PSD of fluctuations due to thermal noise can be expressed as

$$S_T = 4k_B TB \tag{1.8}$$

where $k_B = 1.3807.10^{-23}\ J/K$ is the Boltzmann constant, T is the temperature given in Kelvin and B is the detection bandwidth. The PSD of the flicker noise is linked to electronic components (photodetector, amplifiers, ESA) that are used to measure. This noise is the consequence of several random processes [51]: fluctuations in the number of carriers [52], fluctuations in the mobility of carriers [53]. It is due to the presence of impurities and structural defects during the manufacture of electronic components. So this noise depends on the quality of the manufacturing and the technology employed. In the case of semiconductors, this noise can become annoying for frequencies below a few kHz. Thermal noise is the minimum signal level measurable by the detection bench and then have to be reduced by a judicious choice of devices.

1.3.4 Determination of shot noise

Shot noise (S_{sh}) is related to the randomness of the photons and electrons during the creation of photocurrent in the photodetector. The photocurrent is a function of the incident optical power. The PSD of shot noise is related to the photocurrent. If $H(f)$ is the transfer function of the detection chain, then the PSD of the shot noise is written as [54]:

$$S_{sh} = |H(f)|^2 2qRI_0 \tag{1.9}$$

where R is the load resistance of the spectrum analyzer. q is the electronic charge equal to 1.602×10^{-19} coulomb, and I_0 is the average photocurrent.

To evaluate the shot noise, it is necessary to use a reference source having a negligible intensity noise with respect to that of the shot noise [55]. White light sources are good candidates for this measurement [33, 34]. To ensure that the detection is at the level of the shot noise, we check the linearity of the measurements with the photocurrent. If the relative intensity noise is not negligible, we will have a non-linear behavior. Quantitatively, the shot noise PSD normalized by the photocurrent is given by the relation:

$$S_{sh_{norm}} = |H(f)|^2 2qR \tag{1.10}$$

Then the transfer function of the detection system can be written as:

$$|H(f)|^2 = \frac{S_{sh_{norm}}}{2qR} \tag{1.11}$$

From these thermal and shot noise PSD determination, we can calculate the RIN, as it will be explain in the next section.

1.3.5 Determination of relative intensity noise

The spectral density of the laser intensity noise is given by the following relation:

$$S_{RIN} = |H(f)|^2 RI^2 10^{RIN/10} \tag{1.12}$$

RIN is expressed in dBc/Hz and by abuse of use dB/Hz is used. The RIN of a laser can be obtained by insertion of Eqs. (1.12), (1.11), (1.10) in Eq (1.7):

$$\text{RIN} = 10\log_{10}\left(\frac{2q}{I}\left[\frac{S_{Total} - S_T}{S_{sh_{norm}} I} - 1\right]\right) \tag{1.13}$$

Figure (1.2) shows an example of RIN spectrum of a DFB fiber laser ($Koheras^{TM}$) emitting at a wavelength of 1.55 μm that will be used as a pump laser in the following chapters of this thesis. The peak around 154 kHz corresponds to the relaxation frequency of the laser. Beyond this frequency, the PSD decreases very quickly with a slope of 20 dB per decade. RIN is usually low in laser due to the clamping of the gain that reduces

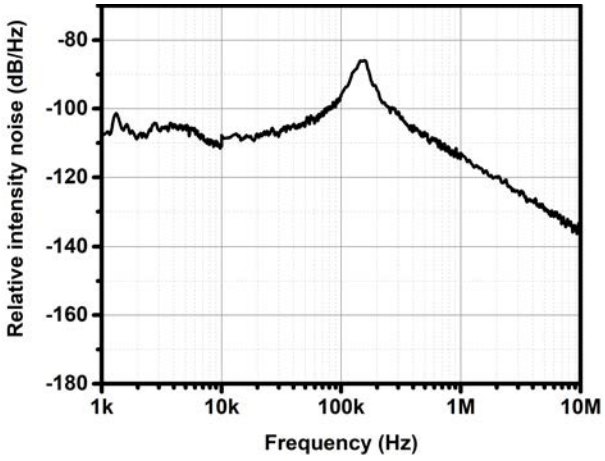

Figure 1.2: RIN of a DFB fiber laser (Koheras) emitting at a wavelength of 1550 nm

the input pump noise. This feedback mechanism is not present on the phase of the laser that continuously drifts and implies a larger noise contribution than in amplitude. The phase noise is explained in next sections.

1.4 Phase noise

In this section, we review the basic concepts of phase and frequency noises of a laser. We also describe the relations between the phase noise, frequency noise, and spectral laser linewidth. Moreover, we explain the measurement method of laser frequency noise based on the self heterodyne technique.

As we have seen in section (1.2), if we consider the laser emission as a perfect signal $E(t) = E_0 e^{i[2\pi\nu_0 t]}$, then the power is concentrated at a carrier frequency ν_0, the optical spectrum will be a Dirac function. But as a matter of fact, a sinusoidal signal has infinite energy and a more precise description will consider a broader emission with finite energy. Then, laser signal will fluctuate randomly in phase so the total power of the signal is symmetrically distributed on each side of the frequency ν_0. The full width at half maximum (FWHM) of the energy distribution is called the laser linewidth. According to the theory of Schawlow and Townes [56], the linewidth of a laser is due to phase noise caused by spontaneous emission of photons in a laser cavity. This fundamental limit of a laser linewidth can be described by a Lorentzian spectral lineshape:

$$\Delta\nu_L = \frac{\pi h\nu}{(2\delta_{1/2})^2 P_0} \tag{1.14}$$

Where $h\nu$ is the photon energy, $2\delta_{1/2}$ is the laser cavity resonance width and the P_0 is the laser output power. Generally, this value is very difficult to measure from the optical spectrum because other technical noise may increase the laser linewidth such as acoustical and mechanical vibrations, mode beatings between different longitudinal or transverse modes and noise transfer from the pump sources to the laser. In semiconductor laser this linewidth will be higher because of the coupling between intensity and phase, which is caused by the refractive index dependence on the carrier density. The study of the phase or frequency noises will give information about the Lorentzian linewidth of the laser and other contributions like Gaussian distribution due to environmental noises. Laser phase noise is characterized in the electrical domain with a single side-band power spectral density $S_\phi(f)$. In the following subsections, we will firstly introduce the relation between phase and frequency noise. Then we will explain the linewidth determination from the frequency noise underlying different noises like white and flicker noise in section (1.4.2). Section (1.4.3) details the experimental method to characterize the frequency

noise using the self-heterodyne method. The inherent noise floor of the experimental bench is analyzed.

1.4.1 Frequency noise in laser

The spectral purity of the laser can be expressed as a function of frequency. The instantaneous frequency of the laser is:

$$\nu(t) = \nu_0 + \delta\nu(t) \tag{1.15}$$

Where ν_0 is the central frequency. $\delta\nu(t)$ is related to the fluctuation of the frequency and phase by $\delta\nu(t) = \frac{1}{2\pi}\frac{d\phi(t)}{dt}$.

$$\nu(t) = \frac{1}{2\pi}\frac{d}{dt}[2\pi\nu_0 t + \phi(t)] = \nu_0 + \frac{1}{2\pi}\frac{d\phi(t)}{dt} \tag{1.16}$$

PSD of the frequency fluctuations $\delta\nu(t)$ can be obtained by Eq (1.17):

$$S_\nu(f) = \int_{-\infty}^{+\infty} R_{\nu(t)}(\tau)e^{-i2\pi f\tau}d\tau \tag{1.17}$$

with $R_\nu(\tau)$ being the autocorrelation function of $\delta\nu(t)$ defined by

$$R_\nu(\tau) =< \delta\nu(t)\delta\nu(t-\tau) >= \int_{-\infty}^{+\infty} \delta\nu(t)\delta\nu(t-\tau)dt \tag{1.18}$$

$S_\nu(f)$ is expressed in Hz^2/Hz. The relation between the phase and frequency noise is then linked through a derivative in the time domain, which implies, for the PSD, a proportional factor equal to the square of the frequency:

$$S_\nu(f) = f^2 S_\phi(f) \tag{1.19}$$

In general, PSD of laser frequency noise can be expressed in the form :

$$S_\nu(f) = \frac{h_{-1}}{f} + h_0 \tag{1.20}$$

Where h_0 is a white noise contribution (due to spontaneous emission). $\frac{h_{-1}}{f}$ is the laser flicker noise. These two contributions are the main ones in lasers. However the -1 term may be replaced by $\frac{h_{-2}}{f^2}$, which is linked to a random walk frequency noise (a term $\frac{h_{-\alpha}}{f^\alpha}$ with $1 < \alpha < 2$, may be also added or it may replace $\frac{h_{-1}}{f}$). It is interesting to know how to relate the frequency noise obtained from the noise PSD and the laser linewidth [57, 58, 59] (that might be obtained from the optical spectrum).

1.4.2 Relation between the power spectral density of frequency noise and optical spectrum

In this section we present a simple approach to estimate the laser linewidth from the frequency noise, a detailed explanation can be found in [57, 58, 59]. If we consider that the laser field is written as $E(t) = E_0 e^{i(2\pi\nu_0 t + \phi(t))}$, neglecting the intensity noise $\delta E(t) = 0$, then the PSD of its frequency noise is linked to the auto-correlation function as follows:

$$R_E(\tau) = E_0^2 e^{i2\pi\nu_0\tau} e^{-2\int_0^{+\infty} S_\nu(f)\frac{sin^2(\pi f\tau)}{f^2}df} \tag{1.21}$$

The laser spectrum is obtained by performing a Fourier transform:

$$S_E(\nu) = 2\int_{-\infty}^{+\infty} e^{-i2\pi\nu\tau} R_E(\tau)d\tau \tag{1.22}$$

As we have seen before a laser frequency noise PSD may be the sum of three types of noise: white, flicker, and random walk. In this thesis, we are focused only on white and flicker noises. In the following, we will detail the contributions of the white and flicker noises separately. Finally, we will explain the general case, which includes both noise contributions in the laser spectrum. The linewidth associated with the white noise is called intrinsic linewidth.

White noise

Let consider that the laser emission is only under the influence of spontaneous emission (white noise), then the PSD of the frequency noise (Eq 1.20) reduces to $S_\nu(f) = h_0$. The optical spectrum Eq (1.22) is then written as:

$$S_E(\nu) = E_0^2 \frac{h_0}{(\nu - \nu_0)^2 + (\pi h_0/2)^2} \tag{1.23}$$

The laser spectrum has a Lorentzian shape. Its FWHM is the laser intrinsic linewidth. $\Delta\nu_L = \pi h_0$. In figure (1.3) plotted the white frequency noise and its optical spectrum. The white frequency noise is plotted for a value $h_0 = 10^4\ Hz^2/Hz$ corresponding Lorentzian shape spectrum is give a intrinsic linewidth $\Delta\nu_L = 31.4\ kHz$. In this thesis manuscript, this relation is used to determine the intrinsic linewidth of a Brillouin laser.

Flicker noise

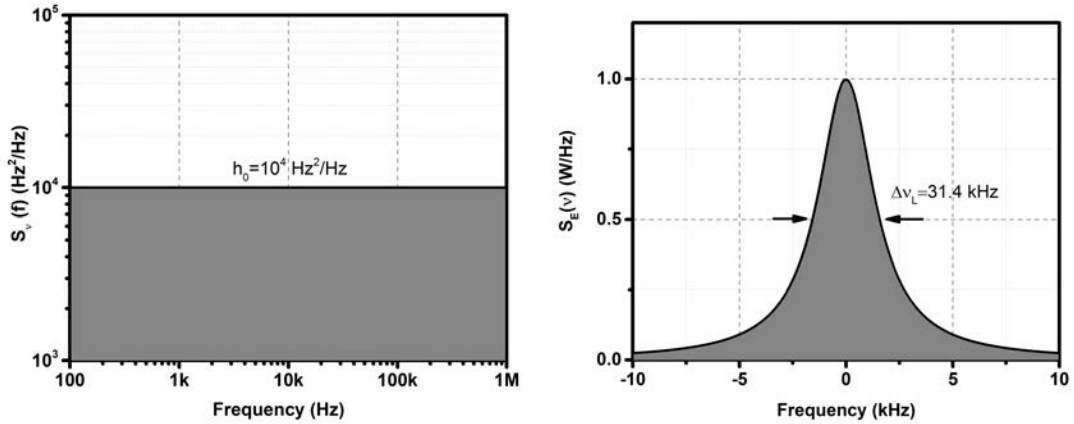

(a) (b)

Figure 1.3: Illustration of corresponding frequency noise and optical spectrum.(a) Frequency noise $S_\nu(f) = h_0 = 10^4\ Hz^2/Hz$. (b) Optical spectral of the laser corresponds to the white frequency noise and the intrinsic linewidth $\Delta\nu_L = 31.4\ kHz$

Frequency fliker noise is slighty more difficult to handle than in the case of white noise. Considering the flicker noise PSD is $S_\nu(f) = \frac{h_{-1}}{f}$. Then Eq.(1.21) is written as

$$R_E(\tau) = E_0^2 e^{i2\pi\nu_0\tau} e^{-2\int_0^{+\infty} h_{-1}(f)\frac{sin^2(\pi f\tau)}{f^3}df} \tag{1.24}$$

In this expression we can see that the integral ($J = \int_0^{+\infty} h_{-1}(f)\frac{sin^2(\pi f\tau)}{f^3}df$) is not defined at $f = 0$ but it can be shown [57] that it is a finite integral with an asymptotic value $\sigma^2 = 3.56h_{-1}$, in which σ^2 is linked to the width of the integrated linewidth.

In order to simplify this problem, we may introduce the notion of observation time (T_{obs}) and the associated minimum frequency (which is simply linked through an inverse relationship). For example, if we measure the frequency noise of a laser at 1 kHz from the carrier then the observation time will be 1 ms (1/1 kHz). The optical spectrum of the flicker noise is a Gaussian function [57].

$$S_E(\nu) = E_0^2 \frac{\sqrt{\pi}}{\sigma} e^{-(\nu_0-\nu)^2/\sigma^2} \tag{1.25}$$

This Gaussian function is centered on ν_0 and corresponds to the density probability function of the laser frequency. In other words, the laser frequency may have deviations from its central frequency ν_0. In the case of flicker noise, the mean deviation tends to an asymptotic value for infinite time of observation, which is linked to the fact that as shown above $\sigma^2 = 3.56h_{-1}$. The linewidth associated with the terms h_{-1}, which implies a frequency jitter, is called integrated linewidth.

Case of laser with flicker and white noise

In the general case, the laser frequency noise contains both white and flicker noise as explained in Eq.(1.20). Then the laser optical spectrum is a Voigt function, which is the convolution of a Lorentzian (white noise) and a Gaussian (flicker noise) functions [58]:

$$S_E(\nu) = E_0^2 \frac{\Gamma}{\sqrt{\pi}\sigma^2} \int_{+\infty}^{-\infty} \frac{e^{-t^2}}{(X^2 - t)^2 + Y^2} dt \tag{1.26}$$

$$X = \frac{\nu - \nu_0}{\sigma},\ Y = \frac{\Gamma}{\sigma},\ t = \frac{\sigma\tau}{2} + iX + Y,\ \Gamma = 2\pi^2 h_0 \tag{1.27}$$

It follows that the linewidth of the Voigt function will depend on the observation time as it has been underlined for the Gaussian function linewidth in the previous section. The Lorentzian function corresponds to the spontaneous emission, which is a white noise (h_0). The central frequency of the Lorentzian contribution will deviate in time with a probability given by a Gaussian function (linked to h_{-1} as mentioned above).

β-line approximation

The lasers that we use in this thesis, has white and technical frequency noise, which can be either a flicker or random walk noise. As we have seen previously the intrinsic linewidth of the laser is easily estimated from the white frequency noise. To estimate the value of the linewidth given by Eq.(1.21) from an experimental frequency noise spectrum, we opted for a recently proposed approach in the literature [57]. It assumes that in practice, any PSD of the frequency noise is separated into two regions by drawing a line, which is called "β-line"(see figure (1.4)). This β-line is described by:

$$S_{\beta-line}(f) = \frac{8ln(2)}{\pi^2} f \tag{1.28}$$

The intersection of the line $S_{\beta-line}$ and of the PSD is at a frequency $f_{\beta-line}$ that indicates the separation of the two regions. The method states that: frequency noise located below the line $f_{\beta-line}$ is usually a white frequency noise due to spontaneous emission. It implies a Lorentzian line-shape. White noise at higher frequencies contributes only to the wings of the optical spectrum, when considering the Voigt profile. The frequency noise located below the $f_{\beta-line}$ frequency will contribute to the Gaussian shape and it will depend on

the observation time. The linewidth of the optical spectrum can be estimated with a 10 % error by the following equation.

$$\Delta\nu_g = \sqrt{8ln(2)A} \tag{1.29}$$

Where A is the area under the curve:

$$A = \int_{1/T_{obs}}^{f_{\beta-line}} S_\nu(f)df \tag{1.30}$$

Figure (1.4) shows an example of the β-line approximation. Laser frequency noise given

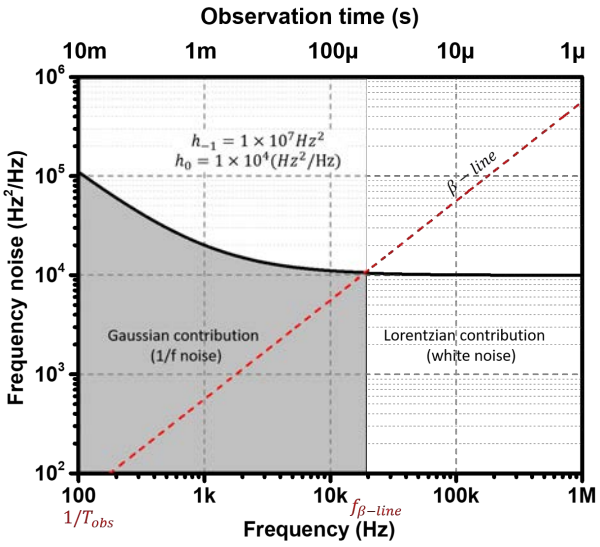

Figure 1.4: Frequency noise and linewidth estimation using $\beta - line$ method

by Eq (1.20) is plotted as a function of the frequency for values $h_{-1} = 1 \times 10^7 (Hz^2)$ and $h_0 = 1 \times 10^4 (Hz^2/Hz)$. The red dashed line represents the β-line and it intersects the frequency noise at $f_{\beta-line}$. The shaded region is the area under the curve, which gives the contribution to the Gaussian line shape (or the low-frequency contribution, implying a frequency jitter of the central frequency of the Lorentzian laser line). Integrated linewidth for an observation time of 10 ms ($1/T_{obs} = 100\ Hz$) gives 37.1 kHz. The intrinsic linewidth is $\pi h_0 = 31.4\ kHz$. This method enables to give an estimated linewidth, which could be useful in addition to a direct reading of the frequency noise. It gives a good estimation of the integrated linewidth for a given time of observation. In other words, it is an estimation of the impact of the low frequency noise (flicker ...). This method allows to evaluate the linewidth of a source which features a $1/f$ frequency noise component and a white noise component. This is the case of many lasers, externally stabilized on a cavity or not. The stabilization reduces the noise but there is always $1/f$ noise close

to the carrier. Sometimes the shape of the frequency noise spectrum is more complex than this two slopes description and the beta-line approximation cannot be used. The frequency noise is measured using a correlated delayed self-heterodyne method, which will be explained in the next section.

1.4.3 Experimental characterization of frequency noise

As we have seen in the previous subsection, the phase/frequency noise enables to analyze laser emission. In this section, we will explain the method, used in our laboratory, to measure frequency noise. As previously mentioned, phase and frequency noise are related. Generally, phase noise measurements are classified into three categories.

The first one is a direct heterodyne detection of two lasers [41, 60]. The signal of the laser under test is beating with the one of a reference laser, for which the phase noise is much lower than that of the laser under test. The resulting beat-note signal transfer the phase noise of the laser in the RF range. This can be then detected by usual devices as ESA. However, it is often difficult to track the beating signal in an electrical spectrum analyzer due to the frequency drift of the laser. To overcome this frequency drift we need more extra efforts to phase-lock two lasers one with each other. The drawback of this method is that low-frequency noise characteristics of the laser under tests are usually lost. When the laser phase noise is lower than the phase noise of the available reference laser, two identical lasers are built and their phases noise compared.

The second method uses a frequency discriminator. Laser frequency fluctuations are converted into intensity fluctuations by a discriminator like Fabry-Perot etalons [61, 62, 63], atomic transitions [64] or interferometers [65, 66]. With this method, the discriminator is operating at a specific frequency and could imply a narrow frequency bandwidth when it has a high resolution. Therefore an active locking of the laser frequency onto the frequency operating point of the discriminator is usually necessary [67].

The third one is based on the delayed self-heterodyne method, which was first proposed by Okoshi *et al.* [68] for measuring the linewidth of a laser. Later, this method was extended to measure the phase noise of a laser by using a short delay [65, 67]. Generally, these two methods are called uncorrelated and correlated delayed self-heterodyne respectively. For the uncorrelated delayed self-heterodyne, the delay time is much longer than the coherence time of the laser, which directly gives only the integrated linewidth of

the laser and it is difficult or even impossible to estimate the intrinsic linewidth. For correlated delayed self-heterodyne, the delay time is shorter than the laser coherence-time, so that the phase of the two fields are statistically dependent. In this case, beating fields contain information on laser frequency noise. This method is used to characterize the laser frequency noise in this manuscript.

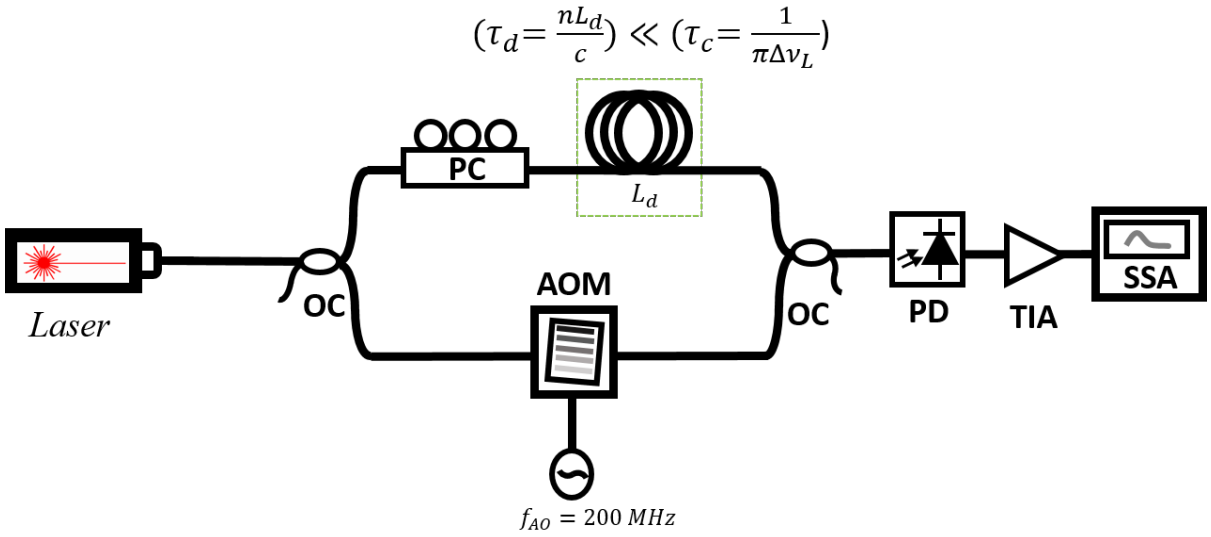

Figure 1.5: Self-heterodyne frequency noise measurement setup. OC: Optical coupler, PC: Polarization controller, AOM: Acousto-optical modulator, PD: photodetector, TIA: Transimpedance amplifier, SSA: Signal source analyzer.

Figure (1.5) is a schematic sketch of the frequency noise experimental setup based on the correlated delayed self-heterodyne technique. The optical signal is separated into two arms by a coupler. One arm is delayed by a fiber length (L_d) corresponding to a delay time (τ_d), which is taken shorter than the laser coherence-time (τ_c). In the other arm, the optical frequency is shifted by an acousto-optic modulator ($f_{AO} = 200\ MHz$). RF beating of the two fields, detected on a photodetector (PD) is also shifted by f_{AO}; it is then amplified using an electrical amplifier (TIA). A polarization controller is placed in one arm in order to maximize the beating signal. The signal source analyzer is used to measure the power spectral density of the phase noise RF beat signal at $f_{AO} = 200\ MHz$. In order to calculate the frequency noise, we need to find the transfer function of the setup, considering that the complex electrical field of the laser is:

$$E(t) = E_0 e^{i(2\pi\nu_0 t + \phi(t))} \tag{1.31}$$

Where E_0 is the signal amplitude and we consider that the laser has also a low-intensity noise. ν_0 is the laser frequency. $\phi(t)$ is the signal phase. Then the intensity detected by

the photodetector can be written in the following form:

$$I_d(t) = E_0^2\Big\{1 + cos\Big[2\pi(\nu_0 + f_{AO})\tau_d + 2\pi f_{AO}t + \Delta\phi(t,\tau_d)\Big]\Big\} \tag{1.32}$$

Where $\Delta\phi(t,\tau_d) = \phi(t) - \phi(t-\tau_d)$ is the phase difference between the two waves. In this approach, we do not take into account the phase noise introduced by the acousto-optic modulator because the laser phase noise is bigger than the electrical oscillator of the acousto optic modulator. The PSD of the laser frequency noise ($S_\nu(f)$) is related to the PSD of the laser phase noise ($S_\phi(f)$) at the output of the interferometer, following the expression that includes the transfer function of the delayed interferometer [65]:

$$S_\nu(f) = \left(\frac{1}{2\pi\tau_d sinc(\pi f\tau_d)}\right)^2 S_\phi(f) \tag{1.33}$$

The signal source analyzer gives the PSD of the phase noise. The frequency noise can be calculated by dividing the phase noise PSD by the transfer function of the interferometer. The interferometer acts as a low pass filter. The bandwidth is inversely proportional to the time delay of the interferometer. Figure (1.6a) gives an example of a transfer function of the interferometer with a delay of 200 meters. The cut-off frequency is 1 MHz, which gives a 300 kHz bandwidth. Figure(1.6b) plotted the gain conversion and measurement bandwidth in function of delay length. The gain conversion corresponds to the linear slope conversion of the transfer function. We can increase the measurement bandwidth by decreasing the delay length. When we reduce the length, the gain is reduced (see figure(1.6b)) (the transfer function is a cosine function; decreasing the delay length will increase the slope and thus the phase to intensity conversion ratio). Experimentally a compromise has to be found between these two parameters, that we usually want both as high as possible. The important point is to control that there is enough gain to have a signal above the noise floor of the bench. Noise floor measurement is explained in the next section.

1.4.4 Noise floor of the measurement bench

It is important to characterize the noise floor of the bench before any measurement of the laser frequency noise. The noise floor is caused by any noise other than that of the laser. The contribution of the noise floor can be due to mechanical and acoustical vibrations of the delay line fiber spool due to the environment. Also, it can be limited

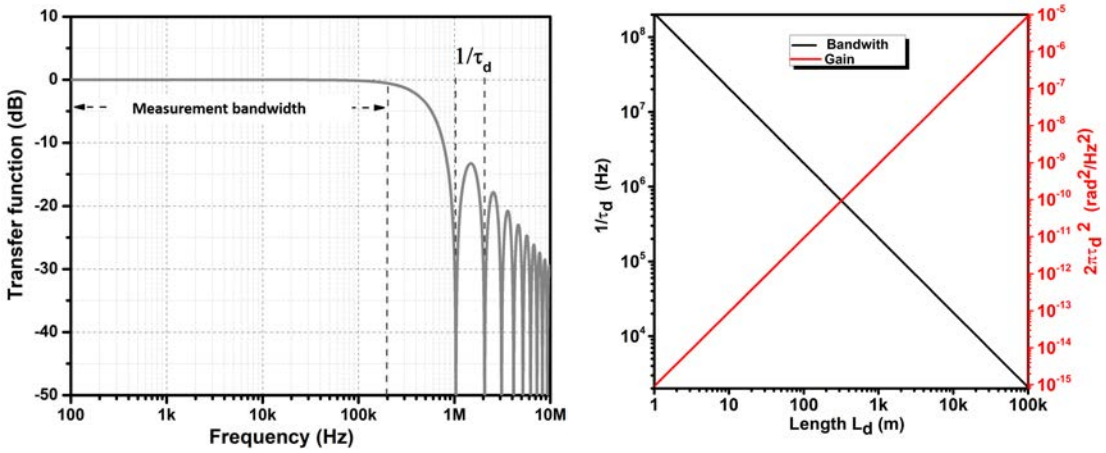

(a) (b)

Figure 1.6: (a) Transfer function of an unbalanced interferometer ($\tau_d = 200\ m$) (b) Cutoff frequency and gain conversion of the test bench, depending on the inserted delay length.

by the instrumental noise like the noise of the signal source analyzer, the noise from the RF modulator, the noise of the photodetector, and of the RF amplifier. Moreover, it can be limited by the intensity noise of the laser.

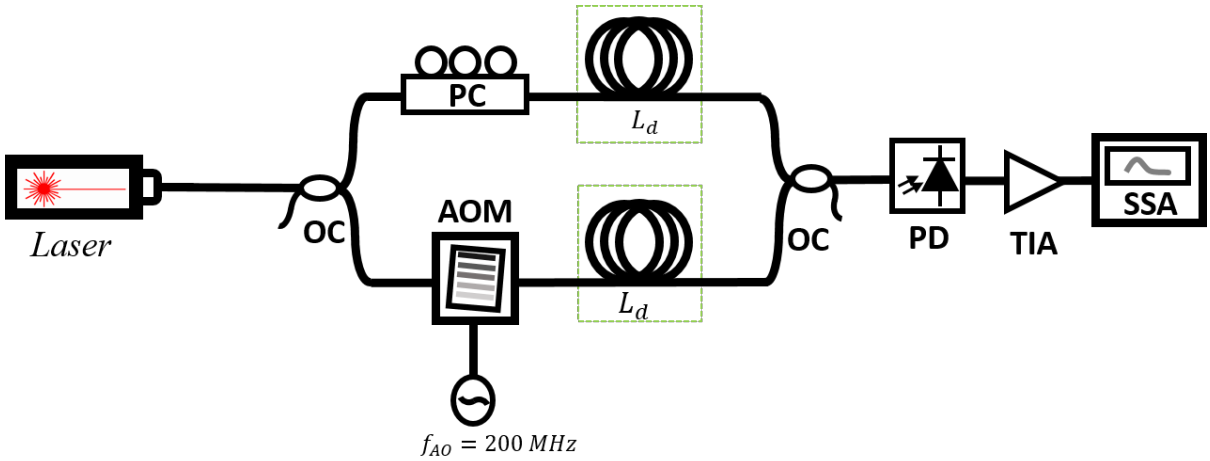

Figure 1.7: Experimental setup for noise floor measurement. OC: Optical coupler, PC: Polarization controller, AOM: Acousto-optical modulator, PD: photodetector, TIA: Transimpedance amplifier, SSA: Signal source analyzer.

In order to measure the noise floor, we used a method proposed by Llopis *et al.* [69], which is based on balancing the delay length of the interferometer. Two identical fiber spools are inserted in both arms (see figure (1.7)). Indeed, in this configuration, the contribution of phase noise is not coming from the laser itself but rather from the measurement system and its environment. In this case Eq (1.32) can be written as:

$$I_d(t) = E_0^2\Big\{1 + cos\Big[2\pi(\nu_0 + f_{AO})\tau_d + 2\pi f_{AO}t + \Delta\phi(t,\tau_d) + \phi_{sys}(t)\Big]\Big\} \tag{1.34}$$

Where $\phi_{sys}(t)$ is the noise from the measurement system and its environment. By balancing the interferometer, then its delay becomes equal to zero ($\tau_d = 0$). In that case, the phase delay of $\Delta\phi$ is null. As the delay is null, the beating between the lines from the two arms gives a coherent signal only at the same frequency under the laser line, bringing a noise component at DC and negligible contributions at other frequencies. It follows that with a null delay the measured noise is only due to the environment and may be attributed to the interferometer and not to the laser. We used this measurement method to characterize the noise floor before each phase noise measurement.

1.4.5 Example of noise measurement

We have explained the frequency noise and its measurement in the above subsections. In this subsection, we will characterize the frequency noise of a *Tunics* OM^{TM} laser and estimate its linewidth by using the $\beta - line$ approximation. As we discussed previously, for each measurement, we should analyze the system noise floor. Figure (1.8a) shows the laser phase noise (blue line) and its interferometer noise floor for different delays. These different delay lengths in MZI enable to improve the gain or the bandwidth. MZI noise floor is given for three delay lengths. First, the phase noise of the modulator signal is plotted in orange color: it is a measure by a direct plug to the SSA. Firstly, we remove the fiber spool from both arms of the MZI, which corresponds to the red curve (0 m) in figure (1.8a). The system sensitivity is measured from other contributions than that of the laser itself. In this case, noise from the fiber spool is not taken into account so it is an optimistic evaluation of the noise floor. The fiber spool may generate noise due to acoustic and mechanical vibrations, and also due to temperature sensitivity of the spool. The identical fiber spools are inserted in each arm to nullify the MZI delay in order to improve the measurement of the noise floor. The additional noise from the previous case is mainly due to the fiber spool. In figure (1.8a), noise floor measurements are shown for 10 and 200 meters of fiber spools in black and pink colors respectively. When the fiber length is increased from 10 meters to 200 meters the phase noise floor of the MZI is increased in the low offset frequency region. For higher frequencies (above 50 kHz), the system noise floor is equal for all cases. Recall that these measurements can be limited by the laser RIN and noise from the photodetector and amplifier. Tunics OM laser phase noise, measured with 10 meter fiber spool delay is plotted in blue color (see figure 1.8a).

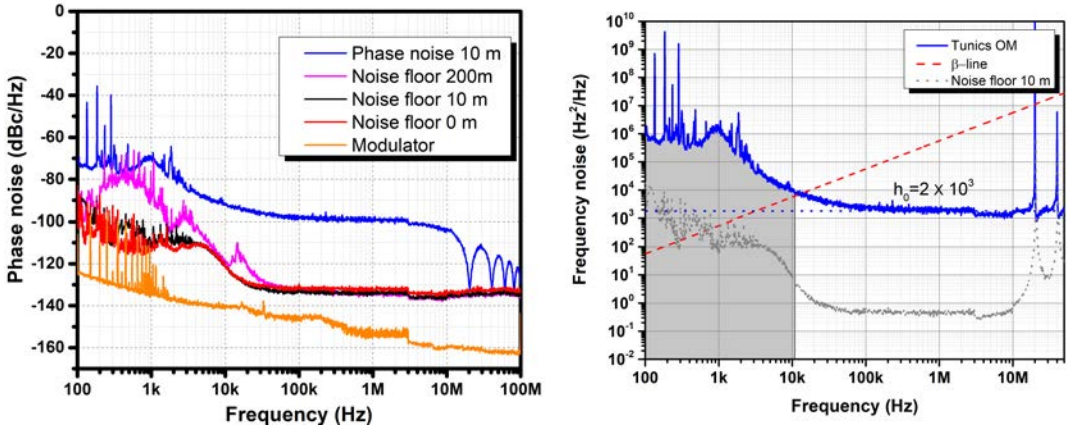

(a) (b)

Figure 1.8: (a) Phase noises of the laser and noise floors of the bench for different fiber lengths. (b) Frequency noise measurement of the Tunics OM laser and its linewidth estimation using $\beta - line$ approximation.

Measured laser phase noise is higher than its noise floor. Also, we can see that the first null at 20 MHz implies a a measurement sensitivity that locally drops down to the noise floor.

As we have seen in Eq (1.33), the PSD of the measured laser phase noise is related to the time delay of the MZI. Calculated frequency noises are plotted in figure (1.8b). The gray dotted line is the noise floor with the 10 m-fiber delay. The frequency noise of the Tunics OM laser is plotted (blue curve) and the white and flicker noise contributions are clearly identified. The grey area under the curve is the one used for the estimation of integrated linewidth. Below 1 kHz, laser experiences a plateau in noise, which may be due to the laser driver. Sharp peaks may arise from thermal and mechanical fluctuations. As discussed in section (1.4.2), intrinsic linewidth of the laser may be estimated from the white noise and integrated linewidth can be evaluated using the $\beta - line$ approximation. 6.28 kHz intrinsic linewidth and 203 ± 20 kHz integrated linewidth for an observation time of 10 ms are obtained. In the next section, we are going to explain how to reduce the technical noise and improve the laser-frequency stability.

1.5 Laser-frequency stabilization

Laser frequency stabilization consists in controlling the laser frequency by a servo-control. This section gives the basic principles of stabilization and the method that is used in this thesis. The detailed explanation can be found in several references [49, 70, 71]. The idea

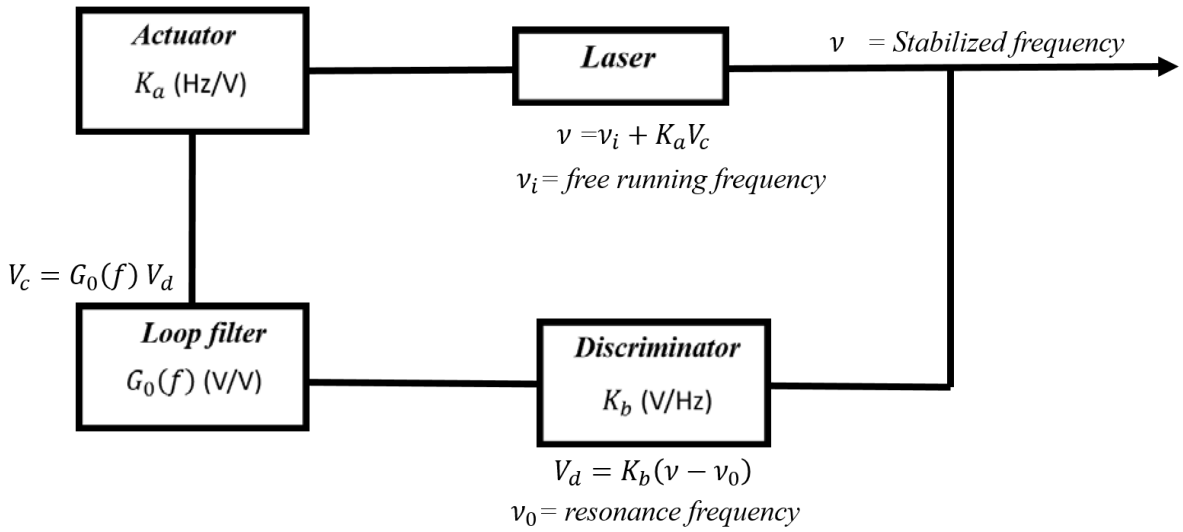

Figure 1.9: General scheme for frequency stabilization of a laser.

behind the stabilization is to measure the instantaneous laser frequency fluctuations using a frequency discriminator. The common method is to compare the laser frequency with a reference frequency. The frequency difference between the reference frequency and the laser frequency is called "error signal". The reference can be a laser or an optical resonator. The idea is to transfer the stability of the reference to the laser in a similar way that an optical cavity can be stabilized by a reference laser. There are several techniques available to do that, like atomic transitions, optical cavity resonance (Fabry-Perot resonator) or optical interferometers (Fiber Mach-Zehnder). Atomic transitions and interferometers give long-term stability when the environmental or operational conditions are minimized. From this measurement, a correction signal is generated through the actuator. This signal is a added to the laser pump in order to ideally compensate frequency fluctuations as a current change generates a frequency shift. The block diagram is given in figure (1.9), with its various elements, and their roles.

Laser-frequency fluctuations are monitored with a discriminator that converts linearly the frequency fluctuations into voltage fluctuations with a conversion slope K_b. This discriminator can be a cavity, gas cell or an interferometer. It generates an error signal, which is amplified and compensated by the loop filter. A PID (Proportional, Integrator, Derivative) device is generally used as the loop filter. It has a frequency-dependent gain coefficient $G_0(f)$. The amplified voltage fluctuations feeds the laser through an actuator, which converts voltage fluctuations into frequency fluctuations by a constant K_a. This actuator is the laser voltage driver.

Let consider that the initial frequency of the free running laser is ν_i. Assume that it is controlled by a servo loop, which corrects the laser frequency to ν that is close to the reference frequency ν_0:

$$\nu = \nu_i - K_a V_c \tag{1.35}$$

ν is considered to be the stabilized laser frequency. V_c is loop filter output voltage. The discriminator response is a function of the laser frequency and its output is a voltage. The discriminator voltage V_d is given by

$$V_d = K_b \delta\nu \tag{1.36}$$

where $\delta\nu = \nu - \nu_0$ is the residual frequency deviation from the references frequency ν_0 of the stabilized laser. The error signal will be a voltage proportional to $\nu - \nu_0$. The discriminator voltage V_d is amplified by a loop filter, described by a frequency dependent transfer function $G_0(f)$. Then the loop filter output voltage (V_c) is applied to the laser through an actuator:

$$V_c = G_0(f) V_d \tag{1.37}$$

The loop equation is

$$\nu = \nu_i - K_a K_b G_0(f) \delta\nu \tag{1.38}$$

which can be written:

$$\frac{\delta\nu}{\Delta\nu} = \frac{1}{1 + G(f)} \tag{1.39}$$

Where $\Delta\nu = \nu_i - \nu_0$ is the initial frequency offset of the free running laser. $G(f) = K_a K_b G_0(f)$ is the gain of the open servo loop. We can see that servo loop reduces the frequency deviation $\Delta\nu$ of the free running laser by the factor of open-loop gain. Thus, the open-loop gain must be large in order to improve frequency stabilization. In general the gain of the amplifier and the servo elements are frequency dependent. For an optimum performances of the servo loop, we need to know the frequency-dependent transfer function of all components [49].

As we have seen in the previous subsections, the laser has mainly two types of frequency noises: white and flicker noise. A frequency discriminator can detect this low-frequency noise fluctuations and suppress them using a feedback control system. Generally, the frequency noise discriminator linearly converts the optical frequency fluctuations into voltage fluctuations. On the other hand, an ultra high finesse optical cavity may be used to stabilize the laser frequency[72, 73, 74] to correct the fast fluctuations and even

reduce intrinsic laser linewidth. Generally, such a stable laser requires highly complicated pressure and temperature stabilization when high performances are expected. In this thesis, a Brillouin fiber cavity is used with a frequency stabilization technique, which enables us to reduce the laser linewidth under the Hz level. In this section, we discuss only the laser stabilization technique, which we used during this work. Brillouin lasing and its noise analysis will be discussed in chapter 3 and 4.

As we have seen before the performances of the locking is determined by the gain of the loop, which is dependent on the different transfer functions. One of the factors is related to the discriminator slope. We used an optical fiber ring cavity as a frequency discriminator. The instantaneous laser frequency is compared to that of the cavity-resonance frequency, which gives the error signal. The two common methods are available to measure the error signal: the side-of-fringe and modulation methods.

In the side-of-fringe method, the laser frequency is locked on to the half of the transmission power of the cavity resonances. At this point, resonance slope will be maximum and the transmission power may be considered proportional to the laser frequency deviations. Sensitivity to the frequency deviation measurements can be improved by increasing the slope of the discriminator with a low loss cavity. This method is easy to implement. However, this technique has some disadvantages. Firstly, laser amplitude fluctuations will be coupled to the frequency fluctuations that will increase the noise level. Secondly, narrow locking bandwidth, small frequency shifts across the cavity transmission lead to a change in amplitude, and then modify the locking point. Thirdly, side locking will reduce the amount of light coupled to the cavity. The modulation method can overcome these problems by locking the laser frequency onto the top of the resonance. The phase shift of the reflected light is measured through a modulation frequency. The slow frequency modulation method is named top-of-fringe locking and the fast modulation method is called the Pound-Drever-Hall technique. These two methods are discussed in the next section.

1.5.1 Top-of-fringe locking

As we have seen, in the side-of-fringe method, the laser is locked onto the side of a resonance. The intensity measurement gives the sign of frequency deviation. On the contrary, if we lock onto the top of a resonance, it is not possible to identify the sign

of a frequency change by a direct intensity measurement because in that case, measured voltage decreases in both variations (positive or negative). To overcome this difficulty, slow frequency modulation is applied to the laser output. When the laser frequency is lower than the cavity-resonances frequency, the frequency fluctuations will be converted to amplitude fluctuations with a certain phase. When the laser frequency is greater than the cavity-resonance frequency, it will create the same conversion with an opposite phase change. At the resonance frequency, the conversion is equal to zero. This correction gives the first derivative of the cavity transmission line-shape function. From the phase change, we can obtain the sign of the laser frequency fluctuations. This error signal acts as a discriminator; it allows us to lock the laser onto the maximum of the resonance independently of the intensity fluctuations.

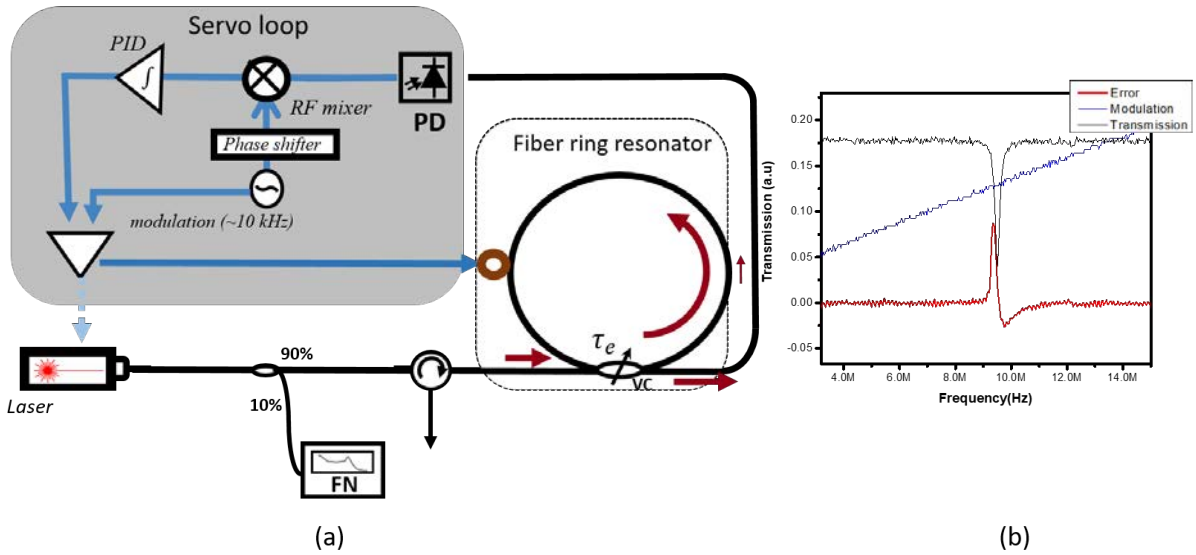

Figure 1.10: (a) General scheme of top-of-fringe frequency stabilization. (b) Oscilloscope traces for transmission laser signal, modulation and top of fringe error signals. PD: photodetector, PID: Proportional–integral–derivative controller, VC: Variable coupler, FN: Frequency noise measurement bench.

Figure (1.10) shows an experimental sketch of the top-of-fringe laser-stabilization. The fiber ring resonator is used as a discriminator and the Tunics OM laser is locked onto the ring cavity. The laser is modulated at lower frequency compared to the linewidth of the cavity resonance and the transmitter beating signal is detected on the photodetector and is demodulated with the modulation frequency thanks to a mixer. A phase shifter will ensure the input of the mixer to have the proper phase relationship between modulation and detected signal. This modulation and demodulation are done with the help of a locking amplifier. The error signal amplifier and the locking point are controlled by a

PID. The PID output is fed to the laser driver, which corrects the laser frequency. The error signal is shown in figure (1.10b), which has an asymmetry due to the mismatching phase shifter.

To summarize, the top-of-fringe method is independent of the laser intensity fluctuations. One major disadvantage is the correction bandwidth that is limited by the modulation frequency, which has to be smaller than the linewidth of the resonance. It's why this method is difficult to implement on very narrow resonance. Similarly, we can lock the cavity resonance onto the laser frequency, in this case, we modulate and correct the cavity length with a PZT. We used this method for the RIN studies of Brillouin fiber laser. The fast modulation method can overcome the disadvantage of the top-of-fringe method.

1.5.2 Pound–Drever–Hall technique

The fast frequency modulation method called Pound-Drever-Hall (PDH) technique was first described by Ronald Drever and John Hall, based on a frequency-modulation technique for microwave cavities developed by Robert Pound [62]. This part gives a brief introduction to the experimental setup of PDH. A detailed explanation of the PDH method can be found in several papers [75, 76].

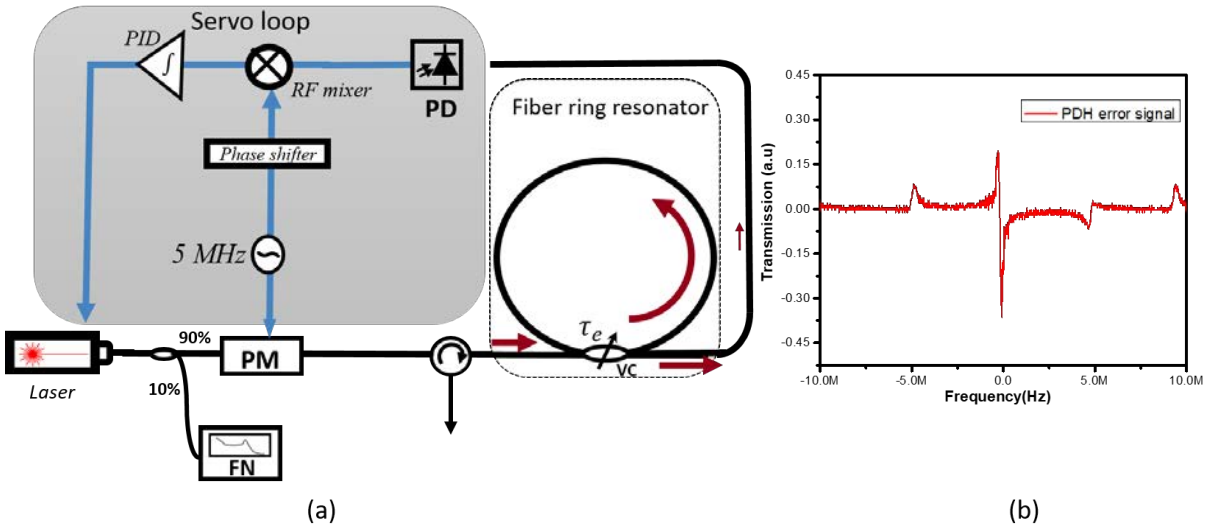

Figure 1.11: (a) General scheme of PDH frequency stabilization. (b) Experimental Oscilloscope traces for PDH error signal. PM: Phase modulator, PD: photodetector, PID: Proportional–integral–derivative controller, VC: Variable coupler, FN: Frequency noise measurement bench.

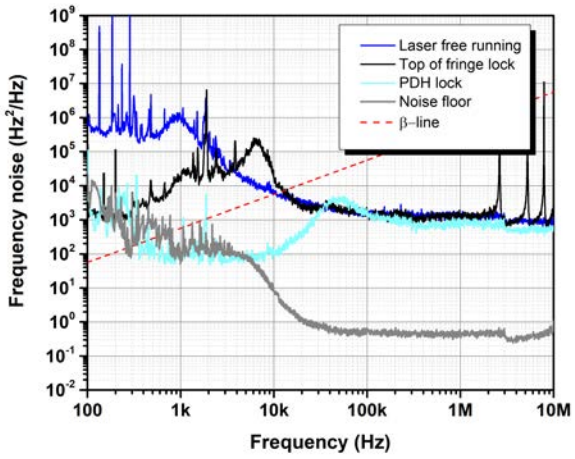

Figure 1.12: (a) Frequency noise measurement of the stabilized Tunics laser on fiber ring cavity with top of fringe and PDH lock.

Figure (1.11) shows the experimental setup of the PDH locking scheme. The fiber ring cavity is used as a frequency discriminator. The experimental setup is similar to the top-of-fringe lock. The phase modulator modulates the laser frequency at a modulation frequency that is higher than the cavity resonances linewidth. This phase modulator produces two frequency modulation sidebands equally spaced from the laser carrier. Since they are well outside the cavity resonances, sidebands are fully reflected from the cavity with no significant phase shift. When the laser carrier frequency matches the cavity resonance, then a reflected component from the cavity will be in phase with the incident light. The beating between the carrier frequency and its side-band is detected at a modulation frequency using a photodetector. At resonance, a sideband frequency beating will be 180^0 out of phase with respect to the other one. It follows that the sum of the two beatings at the modulation frequency (that we will call PDH beating in the following) will be canceled out and there will be no signal on the photodetecor at this modulation frequency. When the laser frequency is detuned slightly from the cavity resonance, the reflected light at the carrier frequency experiences a phase change; the sign of this phase change is given by the sign of the deviation of the PDH beating. The PDH beating will not be zero anymore because it is not exactly 180^0 out of phase. The PDH beating gives the error signal, which is used to correct the laser frequency (see figure(1.11)). Using a low-pass filter to isolate the DC term from the mixer, the PID output provides the error signal that is applied to the actuator for laser-frequency correction, after appropriate conditioning. During this work, the Toptica PDH controller (PDD 110/F) was used for laser stabilization.

Using this frequency stabilization method the laser frequency will be locked onto a cavity resonance. A cavity resonance will be generally more stable in the low-frequency range than a laser frequency. By doing the locking, the cavity stability is transferred to the laser frequency, which reduces the laser flicker noise. Figures (1.12a) shows the laser frequency noise measurement for two different locking methods. The blue line gives the free-running-laser frequency-noise. The black line shows the laser frequency noise using top-of-fringe locking. The locking improves the frequency noise in the low Fourier frequencies; the correction bandwidth is limited to 8 kHz. The top-of-fringe method enables to improve the laser linewidth from $203 \pm 20\ kHz$ (for the free-running laser) down to $72 \pm 7\ kHz$ with an observation time of 10 ms. The cyan line gives the laser frequency noise using a PDH locking; the correction bandwidth is then increased to 50 kHz; the integrated linewidth is reduced down to a value lower than 2 kHz with an observation time of 10 ms. As the noise floor is reached, the estimated linewidth is an approximated value, which is overestimated. Moreover, we measure the noise floor of the bench as shown in figure (1.12b). The PDH locking measurement is limited to the noise floor of the bench.

1.6 Conclusion

In this chapter, basic notions on laser intensity and frequency noise are introduced. Laser RIN is explained as well as the method of measurement using the direct detection method. A description of laser phase and frequency noise is detailed as well as the $\beta - line$ approximation method. Self-heterodyne method is introduced for measuring the laser frequency noise and its noise floor. Moreover, we show that the laser frequency can be stabilized on a fiber ring cavity resonance using the top-of-fringe and PDH methods. These servo-loop method will be used to realize Brillouin lasers in the coming chapters. Before explaining the Brillouin laser under study, we will introduce some generalities about the stimulated Brillouin scattering and its characterization method in the next chapter.

Chapter 2

Brillouin gain characterization using cavity ring-down spectroscopy

2.1 Introduction

This chapter is dedicated to a comprehensive overview of Brillouin scattering and detailed discussions about its characterization in optical fibers using different methods. A new method to characterize the Brillouin gain in high-Q cavities by using Cavity-Ring Down Method (CRDM) is proposed and analyzed.

2.2 Generalities on stimulated Brillouin scattering

Density fluctuations, impurities and thermal agitations of particles in a medium are among the various sources at the origin of different types of scattering. They are classified as linear, when the optical properties of the medium are not modified by incident light, on the contrary, nonlinear scattering occurs when the light intensity is sufficiently high to modify the optical response of the medium. Among nonlinear scattering effects, we can mention electrostriction in Stimulated Brillouin Scattering (SBS) and molecular vibrational and rotational states in Stimulated Raman scattering (SRS) [77]. Indeed, scattering could be divided into two categories, elastic or inelastic scattering. The energy of an incident photon is conserved in elastic scattering; it's why no frequency shift is observed in the scattered photon. Rayleigh scattering is in this category. On the contrary, for inelastic scatterings, energy exchange between scattered photons and incident

photons leads to a change in frequency as for Raman and Brillouin scatterings.

In this thesis, we focus on spontaneous Brillouin scattering and stimulated Brillouin scattering, which are the object of the next sections. The aim of this section is to introduce generalities on Brillouin scatterings such as standard coefficients and equations that will be largely used in the rest of the thesis. Spontaneous and stimulated Brillouin scatterings are described respectively in sections (2.2.1) and (2.2.2). Some of the explanations and equations are taken from the reference [78]. One objective of this thesis is to design a low-noise Brillouin laser. Gain and threshold of Brillouin scattering are key ingredients to implement those low-noise lasers. We then introduce those parameters in section (2.2.3) and (2.2.4) respectively.

2.2.1 Spontaneous Brillouin scattering

In a scattering medium, molecules make small displacements around their position of equilibrium under the effect of temperature. These movements are coupled together and create very small acoustic waves, which propagates in all directions. These acoustic waves modify the local matter-density and cause modifications of the optical index. It creates an index grating that moves at the speed of the acoustic wave. The incident light, for an acoustic wave moving in the same direction, is scattered on this grating with a down-shifted frequency due to the Doppler effect, generating a diffracted wave propagating in the opposite direction. The resulting wave is called a Stokes wave.

When the acoustic wave has an opposite direction to the incident wave, the scattered wave absorbs the energy of phonons and generates photons at a higher frequency called anti-Stokes. This process is called spontaneous Brillouin scattering and it is generated from a thermally excited acoustic vibrations [78]. At room temperature, these acoustic vibrations are present in fiber. Figure (2.1) illustrates spontaneous Brillouin scattering process in terms of wavevector and frequency. Applying the laws of momentum and energy conservations, we can write

$$\vec{k}_S = \vec{k}_P - \vec{q} \tag{2.1}$$

$$\omega_S = \omega_P - \Omega \tag{2.2}$$

Here $\vec{k}_i$, ω_i $(i = P, S)$ are the wavevector and angular frequency of pump and Stokes waves respectively. $\vec{q}$, Ω are wavevector and angular frequency of the acoustic wave,

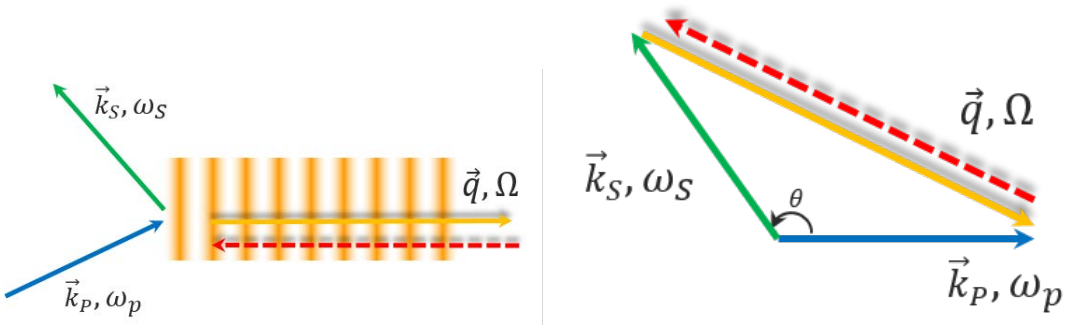

(a) (b)

Figure 2.1: Schematic representation of Brillouin scattering process and schematics diagram of (a) the propagation direction and (b) Momentum conservation of the incident, scattered (Stokes in orange) and acoustic wave. Red dashed lines represent anti-Stokes process.

respectively. Frequencies and wavevectors are related by

$$|\vec{k}_p| = \frac{2\pi n}{\lambda_P}, \qquad |\vec{k}_s| = \frac{2\pi n}{\lambda_S}, \qquad |\vec{q}| = \frac{\Omega}{V_A} \tag{2.3}$$

Here n is the optical refractive index of the medium, and V_A is the longitudinal acoustic velocity. As illustrated in figure (2.1) the conservation of momentum with an angle θ between pump and Stokes wavevector writes as follows:

$$|\vec{q}|^2 = |\vec{k}_p|^2 + |\vec{k}_s|^2 - 2|\vec{k}_p||\vec{k}_s| \cos\theta \tag{2.4}$$

Since $|\vec{k}_P|$ is nearly equal to $|\vec{k}_s|$ ($\Omega << \omega$)

$$|\vec{q}| = 2|\vec{k}_p| \sin\frac{\theta}{2} \tag{2.5}$$

Substitution of Eq (2.5) into acoustic angular frequency shift relation (2.3) gives:

$$\Omega = \frac{4\pi n V_A}{\lambda_p} \sin\frac{\theta}{2} \tag{2.6}$$

In single-mode optical fibers, the only permissible angles are $\theta = 0$ or $\theta = \pi$. Ω is equal to zero for forward scattering and is maximum for back-scattering. This gives the Brillouin frequency shift ν_B ($\Omega_B = 2\pi\nu_B$ at $\theta = \pi$):

$$\nu_B = \frac{2nV_A}{\lambda_p} \tag{2.7}$$

From this, we can understand that the Brillouin frequency shift depends on the pump wavelength and material properties through the acoustic velocity and the refractive index.

Similarly, the anti-Stokes component with up-shifted frequency can be obtained. When

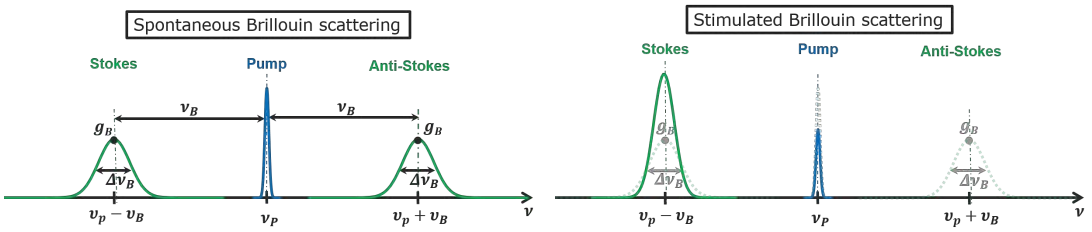

(a) (b)

Figure 2.2: Stokes process in (a) the spontaneous regime. Amplitudes of Stokes and anti-Stokes are of same order. (b) Stimulated Brillouin scattering regime. Stokes amplitude will increase and its gain spectrum narrows. ν_B: Brillouin shift, ν_P: pump frequency, $\Delta\nu_B$: Brillouin gain bandwidth and g_B: Brillouin gain coefficient

acoustics wave is counter-propagating to the pump wave (see figure 2.1a red line), we obtain:

$$\vec{k}_{AS} = \vec{k}_P + \vec{q} \tag{2.8}$$

$$\omega_{AS} = \omega_P + \Omega \tag{2.9}$$

Where $\vec{k}_i$, ω_i $(i = P, AS)$ are, as mentioned above for the Stokes, respectively the wavevector and angular frequency of the pump and of the anti-Stokes waves. In Stokes and anti-Stokes processes, the incident wave interacts with different phonon ensembles. For Stokes process, the pump wave interacts in the same direction as the acoustics wave. For anti-Stokes process, acoustics waves propagate in the opposite direction to that of the pump. In spontaneous Brillouin scattering, the Stokes and anti-Stokes wave have almost the same amplitude because the sources of acoustic phonons are only due to thermal agitation. Figure (2.2a) shows the spontaneous Brillouin scattering spectrum of Stokes and anti-Stokes. The spectral broadening of the two waves are due to the damping of acoustic wave; it is called spontaneous Brillouin gain bandwidth ($\Delta\nu_B$) and it is a unique feature of the Brillouin process. When the injected pump power is increased, the amplitude of the acoustic waves increases leading to efficient Stokes wave generation. This phenomenon is called stimulated Brillouin scattering and is described in the section below.

2.2.2 Stimulated Brillouin scattering

As we have seen previously, spontaneous Brillouin scattering is the result of the interaction between a pump wave and acoustic phonons induced by thermal agitation. The efficiency

of these spontaneous scattering are very low compared to stimulated process. Pump and Stokes waves beat together in the fiber giving rise to an interference pattern oscillating at the Stokes frequency shift ν_B (figure 2.3). For higher pump power, the amplitude of this beating increases and implies a modification of the matter density along the spatial pattern. This physical phenomenon, called electrostriction, is the capacity of a material to be compressed in the presence of an electric field. This electrostriction process induces a moving index grating at the speed of sound (V_A) in the medium, which selects a set of frequencies (ω_S, Ω_B) for a given pump frequency (ω_P). This means that electrostriction process creates a large number of acoustic phonons, which will tend to amplify the Stokes wave generation. The created Stokes wave and the pump wave interferes. This interference itself creates a material grating that increases the beating strength, which reinforces the Stokes wave generation (figure 2.3). Finally these two processes reinforce each other and causes the amplification of Stokes wave. This looping process is called stimulated Brillouin scattering.

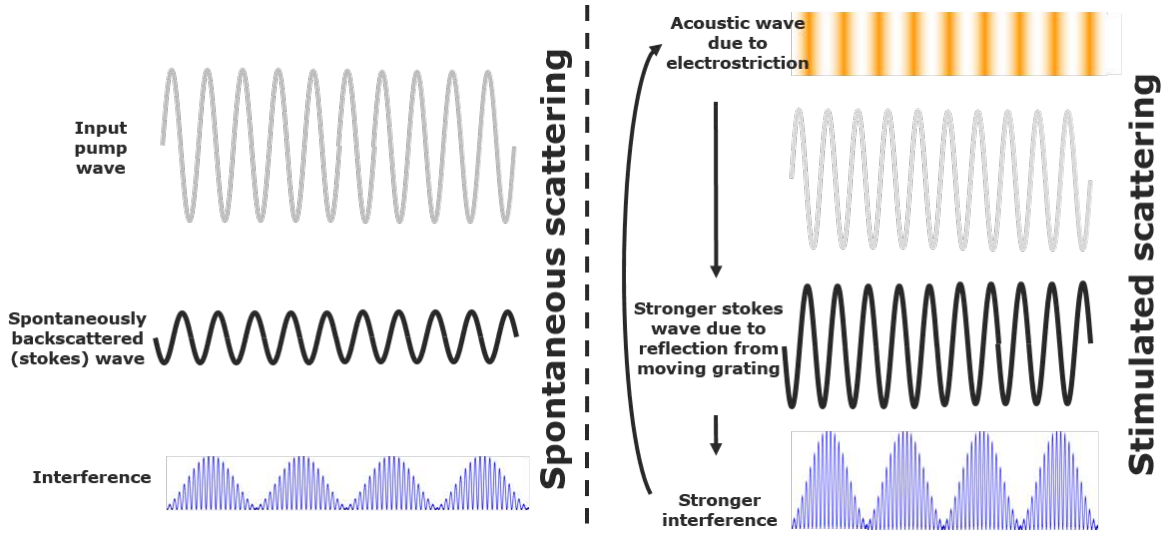

Figure 2.3: Schematic representation of the SBS. The beat between the pump wave and the Stokes wave creates by electrostriction and acoustic wave that diffuses the pump wave and therefore reinforces the Stokes wave.

It is interesting to note that due to the energy conservation condition, scattering Stokes process generates phonons. On the opposite, for anti-Stokes process, the phonons are absorbed by the pump wave in order to generate anti-Stokes photons at higher frequency. In spontaneous regime, Stokes and anti-Stokes have an equal probability to appears and then show the same amplitude (figure 2.2a). In the stimulated regime, high pump power

and electrostriction process rapidly increase the number of phonons, which propagate in the same direction as the one of the pump; it then amplifies the Stokes wave. In contrast, the anti-Stokes process is generated from the annihilation of pump photons and acoustic phonons, which propagate in opposite directions. These annihilations are a strong limitation to the amplification of anti-Stokes (figure 2.2b).

In conclusion, back-scattered Stokes wave is created by spontaneous Brillouin scattering from thermal noise. In stimulated Brillouin scattering, this Stokes wave is amplified through the electrostriction process. This amplification process may be used for the realization of low-noise Brillouin laser. The gain and threshold of Brillouin process are important to study for the design of laser. These two quantities are described in next sections.

2.2.3 Brillouin gain

As we have seen previously, Stokes wave amplitude will grow very rapidly in the stimulated Brillouin scattering regime. This growth will be characterized by the Brillouin gain $g_B(\nu)$. The spontaneous Brillouin gain spectrum is given by:

$$g_B(\nu) = g_B \frac{(\Delta\nu_B/2)^2}{[(\Delta\nu_B/2)^2 + (\nu - \nu_B)^2]} \tag{2.10}$$

The Brillouin gain is maximum at the frequency of $\nu = \nu_B$ and is equal to the Brillouin coefficient:

$$g_B = \frac{2\pi n^7 p_{12}^2}{c\rho_o \lambda_P^2 \Delta\nu_B V_A} \tag{2.11}$$

Where p_{12} is the elasto-optic constant and ρ_0 is the matter density. The Brillouin gain bandwidth is $\Delta\nu_B$ related to the acoustic phonon lifetime ($\tau_a = 1/2\pi\Delta\nu_B$) and to the acoustics absorption coefficient ($\alpha_s = \Delta\nu_B/V_A$). Generally, for standard telecommunication optical fiber, the Brillouin gain bandwidth $\Delta\nu_B$ is 30 MHz, which corresponds to a phonon lifetime of 5.3 ns. The acoustic waves propagate on short distances compared to the optical wave. Typically, Brillouin gain coefficient of standard silica fiber are ranging from 1.5×10^{11} to 3×10^{11} m/W [79, 80]. It is 1000 times higher than the Raman gain coefficient in silica fiber [78]. In fact, the Brillouin gain coefficient strongly depends on the composition of the medium; for example, chalcogenide fiber may have 100 times higher Brillouin gain coefficient than silica fiber [23].

Stimulated Brillouin scattering can be used as an amplification process in fiber. Two configurations may be considered. Firstly, the generator configuration, for which the

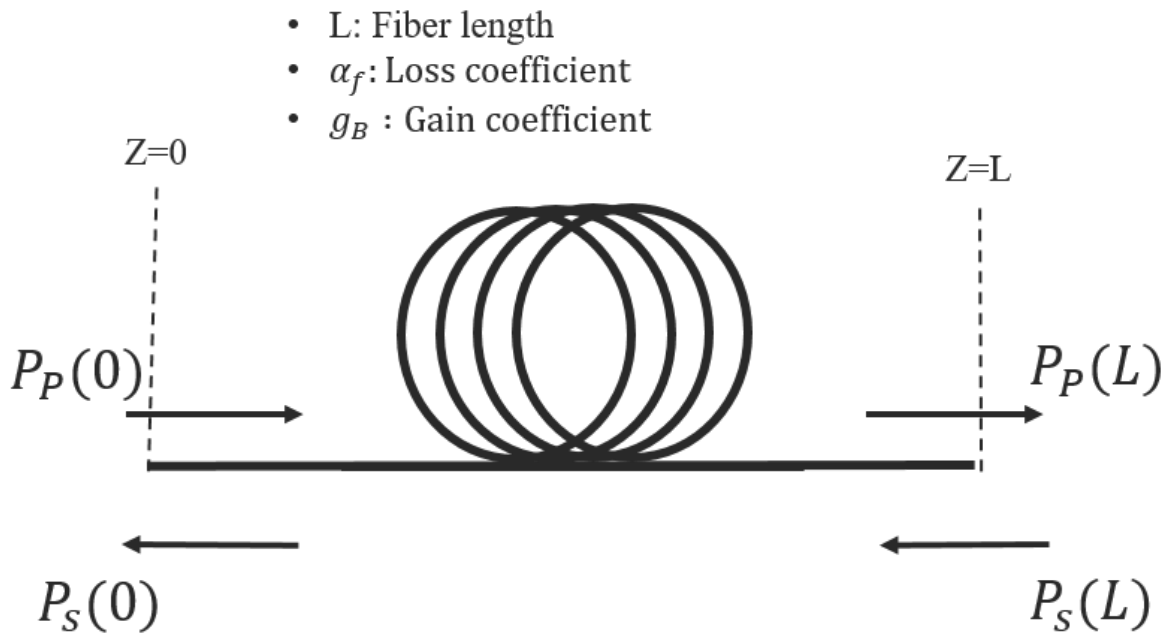

Figure 2.4: Schematics of the pump-probe method. P_p and P_s are the pump and Stokes powers respectively.

pump is injected into the fiber and the thermal noise initiates the Stokes wave. Secondly, the amplifier configuration, for which the pump is injected from one side and a weak signal (called probe) from the other side (see figure 2.4). If the probe frequency satisfies the Brillouin conditions (Eq. 2.2), then the probe signal will be amplified. Hence, the fiber acts as a gain medium. The amplification bandwidth is set by the acoustic phonon decay rate in the medium, which is related to the Brillouin gain bandwidth.

In the following, we will estimate the Brillouin single pass gain (G). To get a first estimation, we neglect the depletion of the pump intensity, by the nonlinear process. Then intensity evolves as $I_P(L) = I_p(0)e^{-\alpha_f L}$, where $I_p(0)$ is the intensity of the pump injected at $z = 0$. L, α_f are the fiber length and the losses coefficient respectively. It follows that the Stokes intensity along the fiber will vary as [78]:

$$\frac{dI_S}{dz} = -k_{polar} g_B I_p(0) e^{-\alpha_f z} I_S + \alpha_f I_S \tag{2.12}$$

Where k_{polar} is a polarization factor, that takes into account the variation of the polarization between pump and Stokes waves. k_{polar} varies between 0.5 and 1 depending on the birefringence and on the length of the fiber [81, 82]. A solution can be found to this equation:

$$I_S(0) = I_S(L) e^{k_{polar} g_B \frac{P_P(0)}{A_{\text{eff}}} L_{\text{eff}} - \alpha_f L} \tag{2.13}$$

Where, A_{eff} is the effective mode area, $L_{\text{eff}} = \frac{1}{\alpha_f}\left[1 - e^{-\alpha_f L}\right]$ is the effective length. The total gain of this optical system may be defined as the ratio of the input and output Stokes intensity I_S (considering that the Stokes wave is contra-propagative from z=L to z=0):

$$G = \frac{I_S(0)}{I_S(L)} = \frac{P_S(0)}{P_S(L)} = e^{k_{polar} g_B \frac{P_P(0)}{A_{\text{eff}}} L_{\text{eff}} - \alpha_f L} \tag{2.14}$$

where G is equal to the net gain of the system. This relation is used for gain characterization based on pump-probe experiments. In this thesis, we used this relation to analyse our experimental observations obtained from the CRDM technique (Section 2.4). As we have seen before the stimulated Brillouin scattering exponentially increases in higher pumping power regime. In the next section, we are going to determine the critical power corresponding to the stimulated Brillouin scattering threshold.

2.2.4 Brillouin threshold

In stimulated Brillouin scattering process, most of the pump power is transferred to the Stokes wave at a critical pump intensity, which is called Brillouin threshold P_{th}. Above this threshold, the Stokes intensity exponentially increases in the opposite direction of the pump. In this section, we determine the threshold power of stimulated Brillouin scattering. The Brillouin threshold is defined variously in the literature but all definitions share the same concept [83, 84, 85].

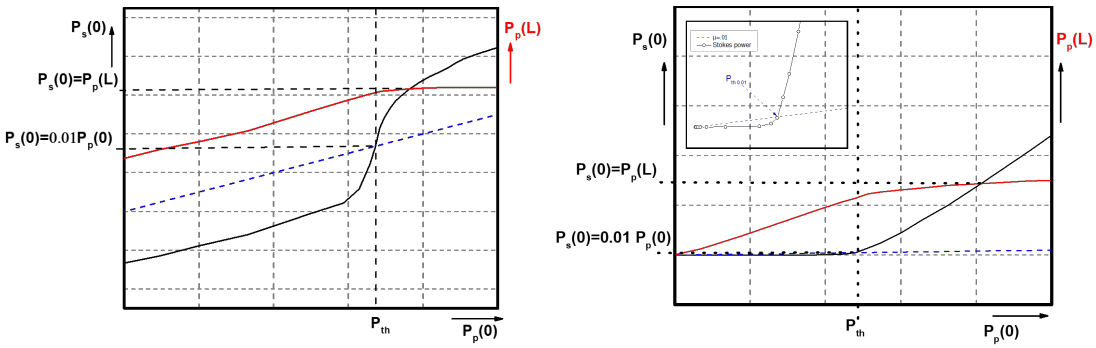

(a) (b)

Figure 2.5: Definition of Brillouin threshold power using transmitted (red) and back scattered Stokes (black) signals plotted as a function of the input power. 1 % of the input signal is plotted in blue color for references. $P_p(0)$: input pump power, $P_S(0)$: back-scattered Stokes, $P_p(L)$: transmitted power; (a) Logarithmic scale (b) Linear scale.

In figure (2.5), back-scattered Stokes ($P_S(0)$) (black curve) and transmitted power ($P_p(L)$) (red curve) are drawn as a function of the input power ($P_p(0)$). Figure (2.5 a) is plotted in logarithmic scale. It clearly highlights the Stokes transition from spontaneous to stimulated Brillouin scattering (black line). The transmitted power linearly increases in the spontaneous regime and then starts to saturate, indicating the onset of the stimulated regime, at a power, that can be defined as the threshold P_{th}. The Stokes and transmitted powers are intersecting at one specific point, that could be also taken as the threshold. 1 % of input power is plotted in blue, which is intersecting the Stokes power (black curve) at the center of the transition in logarithmic scale. Figure (2.5 b) shows the same figure plotted in linear scale. Taking 1 % of input power curve is of interests as it corresponds to an intermediate position in the transition between the end of the spontaneous regime (the first linear progression) and the starting of the stimulated one (the second linear dependence at higher pump powers). More generally, the threshold is defined as the input pump power, which is necessary to get a, back-scattered power equal to a fraction μ of the pump power: $P_s(0) = \mu P_P(0)$. μ may be taken equal to 0.01 [83, 84]. The idea behind this approach is that near threshold the Stokes power follows an exponential behavior and starts to approach an amplitude close to the one of the input power (2.5 b). An analytical equation for threshold can be found in [34, 86]:

$$P_{th} = \frac{g_{th} A_{\text{eff}}}{k_{polar} g_B L_{\text{eff}}} \tag{2.15}$$

Where g_{th} is a factor, which is dependent on μ and on material parameters (see appendix B). This dependency implies that the determination of the threshold from Eq (2.15) involves the knowledge of material parameters of the fiber under study, which are not always available.

In conclusion, Brillouin scattering is the interaction between three waves, which are Stokes, pump and acoustic waves. In spontaneous Brillouin scattering, Stokes wave are generated from interaction of pump wave and a thermally excited acoustic wave. In stimulated Brillouin scattering, the excited acoustic wave and Stokes wave are amplified by the electrostriction process in presence of higher pumping powers. In this thesis we are focused on the development of low-noise Brillouin laser. Indeed, it is important for us to measure the SBS gain bandwidth and gain coefficients to improve the laser design.

In this chapter, we propose an intracavity gain characterization method based on cavity ring-down method (CRDM). In order to compare and validate our experimental method, we characterized the Brillouin gain coefficient through conventional method that uses single pass Brillouin gain determination (section (2.3)). In section (2.4), we explain CRDM and its results. In section (2.4.7), we compare gain coefficients values extracted from CRDM, conventional method and results from the literature in order to validate our new method that allows Brillouin gain to be characterized directly in a laser configuration.

2.3 Experimental characterization of Brillouin gain

Stimulated Brillouin scattering in optical fiber can be experimentally characterized by analyzing the Brillouin scattering spectrum. As previously mentioned, the frequency of back-scattered light is shifted from its pump frequency. Shifted Brillouin spectrum experiences a broadening due to the acoustic waves usually following a Lorentzian shape [85]. At a given pump wavelength, the Brillouin spectra (Eq. 2.10) is defined by three parameters: the Brillouin shift (ν_B), the Brillouin gain bandwidth ($\Delta\nu_B$) and the Brillouin gain coefficient (g_B). These parameters (see table 2.4) are strongly dependent on fabrication process for conventional silica fibers (for example Corning SMF-28) [5, 33, 87, 88]. Also some experimental studies have been made in microstructured fiber, the coupling between optical and acoustical waves may be modified. It may have an impact on the three parameters that govern Brillouin backscattering and thus on the Brillouin threshold of the fiber as demonstrated in silica microstructured fibers [84, 89]. Similarly, Brillouin characterization of chalcogenide glass fibers [23, 90, 91] and planar wave guide [21] were reported. Chalcogenide glasses have higher Brillouin gain coefficients than SMF-28 due to material properties. Such values are reported in Kenny Hey Tow thesis [33], for microstructured chalcogenide fibers, in which the lower effective modal area enhances the nonlinear effect.

In 1972, lppen *et al.* [11] have proposed the first measurement method based on Fabry-Perot etalon, used to determine the Brillouin shift ν_B and gain bandwidth $\Delta\nu_B$, by analyzing back-scattered wave of Brillouin scattering from optical fibers [11]. However the spectral resolution was not good enough to measure precisely the Brillouin gain bandwith. Shibata *et al.* [92] proposed a pump-probe method to determine the on-off gain(G)[1] and

[1]on-off gain: Stokes-power difference with and without Brillouin gain Eq.(2.14)

Brillouin gain bandwidth. Two laser sources are required: a pump and a probe, for which signals are contra-directional. The probe frequency, which is shifted from the pump by the Brillouin shift, is tuned finely to scan the Brillouin gain line. Nikles *et al.* [80] used a single laser source. They generate pump and probe signals using electro-optic modulator. Another method to measure the Brillouin gain spectrum is the self-heterodyne technique, which was proposed by Tkach *et al.* [93]. In this method, the beating between the pump and the back-scattered wave is simply analyzed with an RF spectrum analyzer.

The above mentioned methods require input powers of the order of hundreds of milliwatts to watts or fiber length of the order of 10's of km, so that they cannot be used in case of short lengths (integrated resonators or micro-resonators) or low-power damage-threshold photonic structures. Moreover the techniques listed above do not allow to characterized the gain inside a resonator configuration.

To overcome these drawbacks, we propose in the following to adapt an existing technique, based on cavity ring-dow method (CRDM), to the Brillouin gain characterization inside a high-Q resonator. Before describing the CRDM technique, we determine the Brillouin gain coefficient using conventional methods. In this section, two Brillouin gain characterization methods are analyzed and compared using the same fiber. In section (2.3.1) we describe the self-heterodyne method, which is based on measuring the back-scattered Stokes frequency and the gain bandwidth. From Brillouin gain bandwidth, we can estimate the Brillouin gain coefficient using Eq. (2.11) by knowing the parameters. In section (2.3.2), we verify the Brillouin threshold using estimated Brillouin gain coefficient from the self-heterodyne technique.

2.3.1 Self-heterodyne technique

In the following, we describe the self-heterodyne (SH) technique proposed by Tkach *et al.* [93] and used for the Brillouin gain characterization in various media as silica optical fibers [93], As_2Se_3 chalcogenide fibers [23], tellurite fibers [94], Bismuth-oxide fibers [95], polymer optical fibers [96] and photonic crystal fibers [84, 89]. Among the various approaches listed above to measure the Brillouin gain, we described in more detailed the self-heterodyne technique since this is the one usually used in our lab.

We will then compare the gain evaluation obtained by both the SH technique and the CRDM on a given fiber. The objective is to calibrate the CRDM technique and to

confirm its ability to be used for Brillouin gain determination in high-Q resonators.

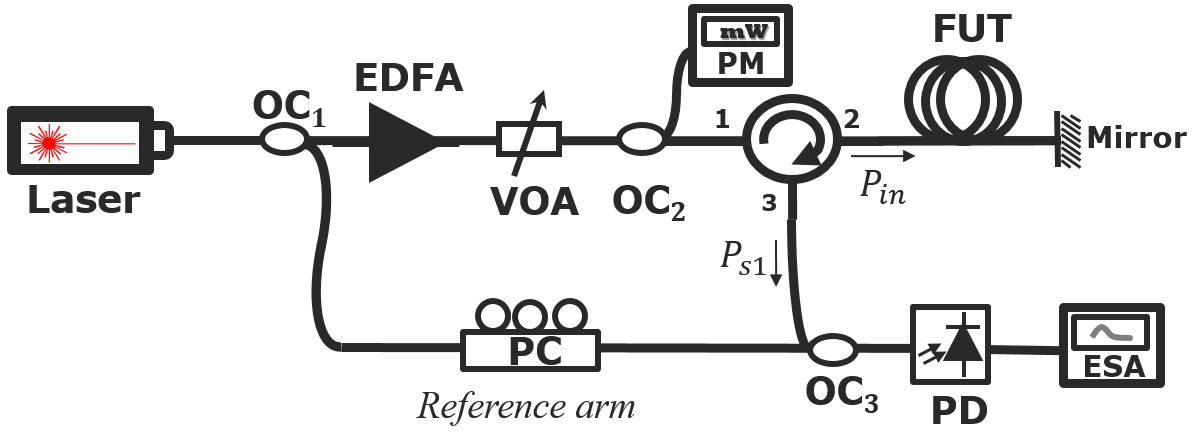

Figure 2.6: Experimental setup of self-heterodyne technique for measuring the Brillouin gain bandwidth. EDFA: Erbium doped fiber amplifer, VOA: Variable optical attenuator, PM: Powermeter, FUT: Fiber under test (L=26 km), PC: Polarization controller, PD: Photodetector, ESA: Electrical Spectrum Analyzer, OC: Optical coupler.

The self-heterodyne method is based on the measurement of Brillouin gain spectrum by beating pump and back-scattered Stokes waves. The beating signal is measured using a fast-photodetector and a RF spectrum analyzer. Therefore, the beating between the pump and Stokes waves, separated from the Brillouin shift, will directly give the gain spectrum; the laser pump is acting as a local oscillator when pump linewidth is much lower than that of the Brillouin gain spectrum.

Figure (2.6) gives a schematic of the experimental setup for the self-heterodyne technique. The pump laser is a narrow linewidth fiber laser (from Koheras), with less than 2 kHz linewidth, emitting at 1.55 μm wavelength. The power emitted by the pump laser is splitted into two arms, by a 50/50 coupler (OC_1). The first arm is called the "pump" arm and the second one the "reference" arm. The signal from the "pump" arm is amplified by an EDFA and then controlled by a variable optical attenuator (VOA). 1 % of the pump is extracted through a coupler (OC_2) for power monitoring before being injected into the fiber under study via an optical circulator. The Stokes wave is mixed with the signal of the "reference" arm by using a 50/50 coupler (OC_3). The resulting beat signal is transformed into an electrical signal by a fast-photodetector (20 GHz bandwidth), amplified and analyzed by an Electrical Spectrum Analyzer (ESA). Note that a polarization controller (PC) is inserted into one of the two arms of the coupler to maximize the amplitude of the beat signal.

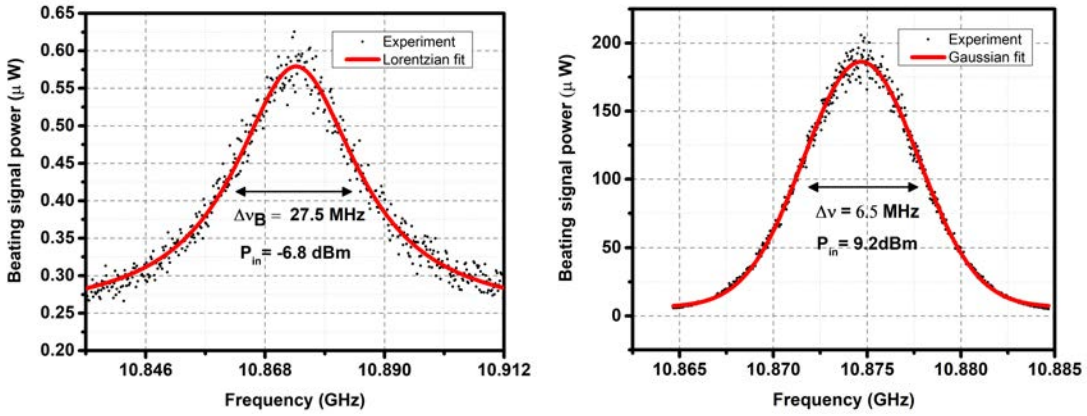

(a) (b)

Figure 2.7: (a) Spontaneous Brillouin spectrum at -6.8 dBm with Lorentzian fit. (b) Stimulated Brillouin spectrum at 9.2 dBm with Gaussian fit.

As we have seen before in section (2.2.4), Brillouin threshold is directly related to the fiber length so we used a 26 km long SMF-28 optical fiber for our Brillouin gain characterizations. Brillouin scattered spectra for different pump powers are shown in figure (2.7 a, b). The beating signal between Stokes wave and reference laser are centered at 10.87 GHz, which corresponds to the Brillouin shift of SMF-28 fiber. The FWHM of the scattering spectrum can be extracted from these experimental data by superimposing the experimental curves either with a Lorentzian or a Gaussian curve. Doing so, the profile of the scattering spectrum is obtained and FWHM is computed analytically. Figure (2.7a) shows the experimental gain curve and the associated Lorentzian fit at low power. As the pump power is increased, the back-scattered signal linewidth becomes narrower as reported in Gaeta *et al.* [85] and it can be approximated by a Gaussian fit.

In spontaneous regime, back-scattered Stokes linewidth depends only on the acoustic phonons decay rate, which is the spontaneous Brillouin gain spectrum. In stimulated regime, the back-scattered light will be amplified by the electrostriction process that will narrow the back-scattered Stokes linewidth. The evolution of the FWHM of the Brillouin spectrum as a function of the power injected into the silica fiber is plotted in figure (2.8). We can see that the FWHM for spontaneous regime is 27.5 ± 2 MHz. This value decreases exponentially when the injected power increases; finally it is saturating around 6.5 ± 2 MHz. The Brillouin gain bandwidth can be extracted from the spontaneous Brillouin spectrum which gives $\Delta\nu_B = 27.5MHz$.

As we have seen in section (2.2.3), we can estimate the Brillouin gain coefficient from the spontaneous Brillouin gain bandwidth and material parameters of the SMF-28 fiber.

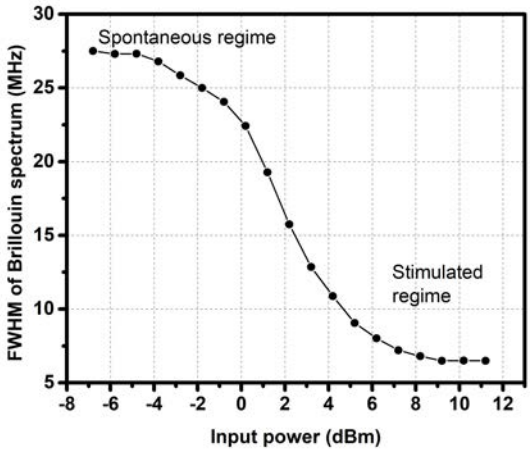

Figure 2.8: FWHM of Brillouin spectra as a function of the input pump power in SMF-28 fiber.

We recall the Brillouin gain coefficient Eq. (2.11)

$$g_B = \frac{2\pi n^7 p_{12}^2}{c\rho_o \lambda_P^2 \Delta\nu_B V_A} \tag{2.16}$$

Where, material parameters of the SMF-28 are given in table 2.3 and 2.4. The obtained Brillouin gain coefficient $g_B = 1.92 \pm .14 \times 10^{-11}\ m/W$ is laying within a range of reported values $1.9 - 2.5 \times 10^{-11}\ m/W$ in the literature [79, 80].

2.3.2 SBS threshold

In this section, we want to verify the experimental estimation of g_B performed in the section above using the SH technique. To do so, we will proceed using the following steps. First we will analytically estimate the Brillouin threshold from Eq. (2.11) using the previous experimental estimation of g_B. Then, we will compare the estimated P_{th} value to an experimental characterization of P_{th} using the definition given in section (2.2.4). We will conclude by a discussion on the matching between the estimated P_{th} and the experimentally determined value. As we have seen in section (2.2.4), the Brillouin threshold is proportional to g_{th} through material parameters (see Eq. 2.15). We substitute the Brillouin gain coefficient from self-heterodyne and other parameters (see table 2.3) in Eqs. (B.2-B.5) and estimate that g_{th} is equal to 11.24 for 26 km long fiber with losses of 0.2 dB/km. Similarly, SBS threshold was calculated from Eq.(2.15) taking into account the following parameters $A_{\text{eff}} = 84.90\ \mu m^2, k_{polar} = 2/3, L = 26\ km$ ($L_{\text{eff}} = 15\ km$) and $g_B = 1.92 \pm .14 \times 10^{-11}\ m/W$. We have an estimated SBS threshold of $P_{th} = 4.90 \pm .80\ mW$.

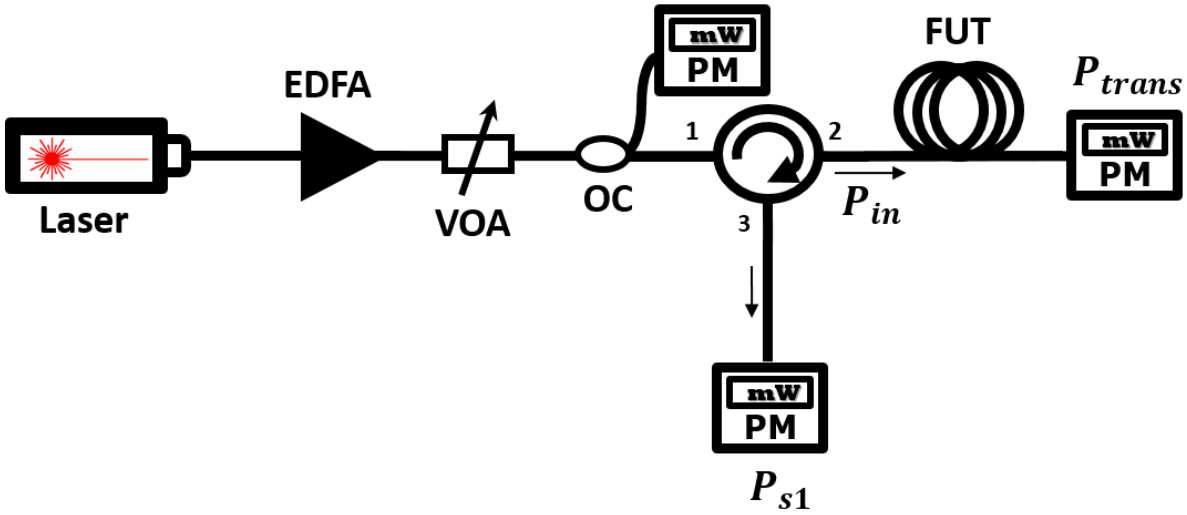

Figure 2.9: Experimental setup for SBS threshold measurement. EDFA: Erbium doped fiber amplifer, VOA: Variable optical attenuator, FUT: Fiber under test (L=26 km), PM: Powermeter, OC: Optical coupler.

This value will be compared in the next paragraph to the Brillouin threshold estimation through L-I curve measurement.

Brillouin threshold estimation through L-I curve measurement

The experimental estimation of the SBS threshold of the optical fiber requires the measurement of transmitted and back-scattered powers according to the input pump power into the fiber as shown in figure (2.9). The pump laser is a DFB-fiber laser from Koheras, emitting at 1.55 μm wavelength. The laser output is amplified using an Erbium-doped fiber optical amplifier (EDFA) before being injected into the optical fiber under test (FUT) via port 2 of an optical circulator. A variable attenuator (VOA) and a 99/1 coupler were placed before port 1 of the circulator to vary and measure the injected pump power (P_{in}) into the FUT. The back-scattered power (P_{S1}) is read using a power-meter placed on port 3 of the circulator. Transmitted power (P_{trans}) is measured at the end of the FUT. In figure (2.10) are shown the back-scattered and transmitted powers as a function of the injected pump power. The straight line corresponds to 1 % of the injected pump power. We can determined from figure (2.10), the Brillouin threshold identified as the transition from spontaneous to stimulated regimes. 1 % of the injected pump power is intersecting the Stokes signal at the center of the S shape curve. At the same pump power, the transmitted pump signal started to experience a saturation due to the non-

linear process that efficiently transfer pump power towards the Stokes. Then Brillouin threshold of 4.78 mW (6.8 dBm) was measured, which is in agreement with the estimated value $P_{th} = 4.90 \pm .80\ mW$ obtained from SH technique.

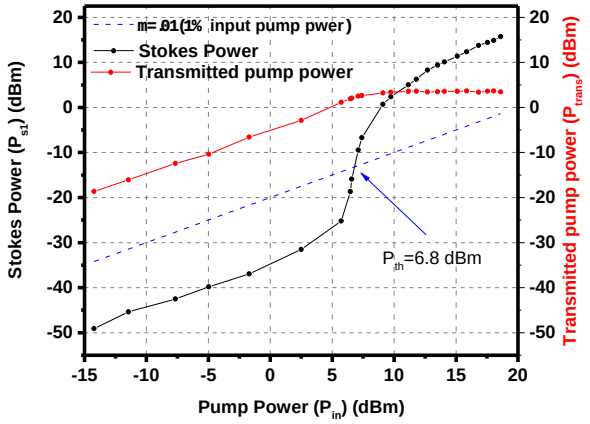

Figure 2.10: Brillouin threshold estimation using L-I curve measurement for a 26 km long SMF-28.

In the above sections, we have explained the determination of Brillouin gain coefficient using a self-heterodyne technique. We compare the Brillouin threshold estimations by analytical and experimental methods. This comparison validates our estimated Brillouin gain coefficient. These methods require a balance between the fiber length and the injected pump power. In case of short length, as in integrated waveguide and micro-ring cavities, the injected pump power becomes too important to adopt these methods especially because the interaction length is short (larger level of losses with respect to the fiber). It is why in the next section we introduce a new gain characterization method based on cavity ring-down method (CRDM), that requires less fiber length and injected pump-power because the re-circulation of light inside the resonator will increase the effective length of interaction.

2.4 Cavity ring-down method

The cavity ring-down method (CRDM) is a well-known technique in optical spectroscopic that measures the decay rate of light injected in an optical resonator. In 2008, Institute FOTON published that CRDM can be used to determine the coupling regime for passive resonators and the resonant gain for active resonators. The method was tested on Er^{3+} doped fiber resonators and also applied to determine the intrinsic and external Q-factors

of an MgF_2 whispering gallery mode resonator [97]. Later, it has been implemented on Erbium doped fluoride glass WGM microresonator [2], and studied the possibility of controlling the coupling regime of an ultrahigh Q-factor microresonator from undercoupling to spectral selective amplification by changing the pumping rate. Also, it was shown that transmission and dispersive properties of the microresonators can be characterized using the CRDM. In 2010, Trebaol *et al.*[98], have shown that the CRDM technique can accurately measure linear properties and frequency splittings of high-Q factor WGM microresonators. In 2015, CRDM was extended to the nonlinear regime study in [99], which enables the input power and the mode volume to be estimated for microspheres. Savchenkov *et al.* [100] reported an experimental observations of power-dependent and nonexponential decay of light stored in whispering gallery modes caused by stimulated Raman scattering in the resonator using cavity ring-down method. CRDM is a well established technique for gas sensing applications. Nowadays the CRDM is used in optical cavity characterization, and it is successfully implemented in various optical cavities like lithium niobate microdisk [101], strontium fluoride microresonantor [102], etc.

In this thesis, we propose to extend the use of the CRDM to retrieve the Brillouin gain coefficient. Performing Brillouin gain characterization inside the laser cavity takes advantage of the light re-circulation of the Stokes wave inside the resonator. As a matter of fact, it strongly increases the effective length of the Stokes wave in the waveguide; this leads to reduce the SBS threshold compared to common gain characterization techniques. This technique could also identify several nonlinear processes that can occur in such a high-Q resonator, for example, thermal drift and Kerr effect [99]. Moreover, the gain coefficient is obtained without the need for material parameter values. Also, this method can be used for characterization of the fiber resonator in order to measure the Q-factor, resonance width, coupling and losses coefficient.

This section is organized as follow: we describe the cavity parameters in section (2.4.1). Then we explain the two characterization approaches, namely the stationary and the dynamic in section (2.4.2) and section (2.4.3) respectively. In these sections, some of the explanations and graphs are taken from the thesis of Stéphane Trebaol [1]. In section (2.4.4), we describe the Brillouin gain coefficient characterization using CRDM and explain the relation between the Brillouin gain and cavity photon lifetime. In section (2.4.5), we make a detailed description of the experimental bench to retrieve the intracavity Brillouin gain coefficient from the CRDM technique. In section (2.4.6), we

discuss the results obtained using the CRDM method. These results have been published in "OSA Continuum" in December 2019 [103].

2.4.1 Cavity parameters description

We will describe the resonators in a very general way with the introduction of different notations and parameters such as the quality factor, coupling ratio, cavity losses or gain and resonance width. To introduce the general properties of optical resonators, we study the particular case of a ring resonator. We are going to get the transfer function of our system via the theory of coupled modes [104]. For this, there are two approaches: a frequency one and a temporal one that we relate to stationary and dynamical regimes.

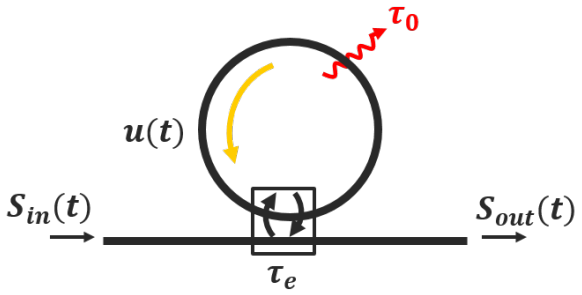

Figure 2.11: Schematic view of the resonator. $S_{in}(t)$: input field, $S_{out}(t)$: output field, u(t) : resonant field, τ_0 : intrinsic photon lifetime, τ_e : coupling lifetime.

The resonator mode under study is described by its lifetime τ and its field of amplitude $u(t)$ as shown in figure (2.11). The cavity is coupled to a bus waveguide with a coupler. Resonance frequencies are separated by the free spectral range $\Delta\nu_{FSR} = c/(nL) = 1/\tau_L$, where τ_L is the round trip duration, n is the effective group index of the resonator mode and L is the round trip length. We consider only one resonance frequency ω_0. The resonator mode amplitude u is excited by using an input field S_{in}. The total photon lifetime $\tau/2$ in the resonator is related to the coupling and intrinsic losses of the considered resonance:

$$\frac{1}{\tau} = \frac{1}{\tau_0} + \frac{1}{\tau_e} \tag{2.17}$$

where $\tau_0/2$ is the intrinsic photon lifetime and $\tau_e/2$ is the coupling lifetime. Similarly, the total quality factor of the resonator is defines as:

$$\frac{1}{Q} = \frac{1}{Q_0} + \frac{1}{Q_e} \tag{2.18}$$

where,

$$Q = \frac{\omega_0 \tau}{2} \tag{2.19a}$$

$$Q_0 = \frac{\omega_0 \tau_0}{2} \tag{2.19b}$$

$$Q_e = \frac{\omega_0 \tau_e}{2} \tag{2.19c}$$

Q_0 and Q_e are the intrinsic and extrinsic quality factors. ω_0 is the resonance frequency of the cavity. Later, we will show that τ_0 and τ_e are linked to the cavity losses and coupling ratio, which allowed us to estimate the Brillouin gain coefficient.

According to the damped harmonic oscillator model as described in [1], the excitation signal is $S_{in}(t)$ and the temporal evolution of the mode amplitude in the cavity is $u(t)$.

$$\frac{du}{dt} = \left(i\omega_0 - \frac{1}{\tau}\right)u(t) + \sqrt{\frac{2}{\tau_e}}S_{in}(t), \tag{2.20}$$

The output signal is expressed as:

$$S_{out}(t) = -S_{in}(t) + \sqrt{\frac{2}{\tau_e}}u(t) \tag{2.21}$$

If we scan slowly the emitting frequency of the probe signal across the resonator mode resonance (that means in a time longer than the lifetime of the resonator), we obtain the stationary response of the resonator. But if we scan faster (that means in a time shorter than the lifetime of the resonance), then we obtain the transient (dynamic) response of the resonator. Depending on the frequency scanning dynamics of the probe laser line, the shape of the transmitted signal through the bus waveguide will be impacted. We detailed, in the following, two specific configurations of the probe signal and the related information that can be explored from the resonator.

2.4.2 Stationary approach:

We assume a monochromatic input signal of the form:

$$S_{in}(t) = S_0 \exp(i\phi(t)) \tag{2.22}$$

Where $\phi(t)$ is a real function which is equal to ωt, where:

$$\omega = \omega_0 + 2\pi\delta \tag{2.23}$$

δ is the detuning from the resonances frequency. Then Eq. (2.20) is solved analytically and we obtained the expression of the transfer function $H(\delta)$:

$$H(\delta) = \frac{S_{out}}{S_{in}} = \frac{1/\tau_e - 1/\tau_0 - i(2\pi\delta)}{1/\tau_e + 1/\tau_0 + i(2\pi\delta} \tag{2.24}$$

and therefore the transmission $T(\delta) = |H(\delta)|^2$

$$T(\delta) = \frac{(1/\tau_e - 1/\tau_0)^2 + (2\pi\delta)^2}{(1/\tau_e + 1/\tau_0)^2 + (2\pi\delta)^2} \tag{2.25}$$

From this equation, we can plot the transmission spectrum with respect to the photon lifetime, which gives the different operation regimes of a resonator. Figure (2.12 a) shows the transfer function $T(\delta)$ for different values of the τ_0/τ_e ratio at resonance frequency ω_0. The curves have a Lorentzian shape with full width at half-maximum of $2\delta_{1/2}$ at the exception of the case $1/\tau_0 = 0$, which corresponds to the transparent regime. This regime is characterized by constant transmission over the spectrum ($T(\delta) = 1$). The different coupling regimes are discussed in the next section.

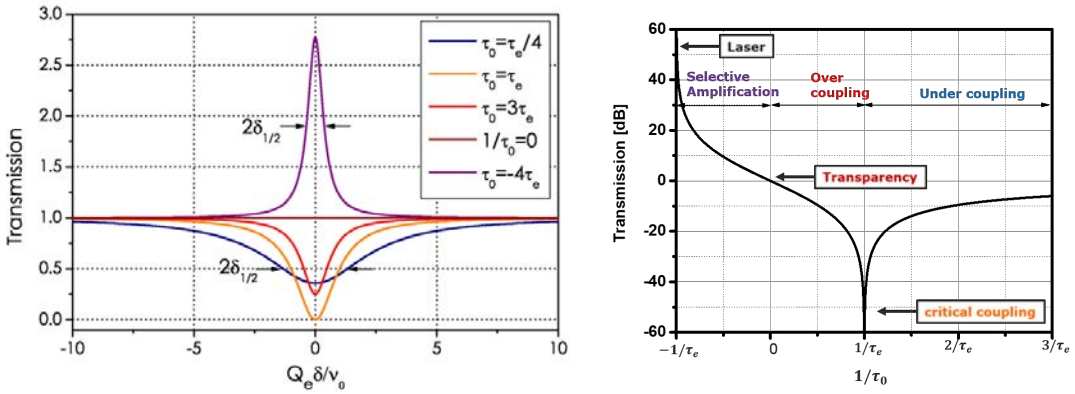

(a) (b)

Figure 2.12: (a) Transmission spectrum in steady state for different relative values of τ_0 and τ_e [1]. (b) Transmission at resonance T(δ=0) in decibels as a function of $1/\tau_0$ for the different coupling regimes.

2.4.2.1 Transmission and coupling regime

Considering the intensity of transmission at resonance $T(\delta = 0)$ in Eq. (2.25 b) we get:

$$T(\delta = 0) = \left(\frac{\tau_e - \tau_0}{\tau_e + \tau_0}\right)^2 \tag{2.26}$$

Figure (2.12 b) shows transmission at resonances $T(\delta = 0)$ for different intrinsic photon lifetimes. The relative values of τ_0 and τ_e determines the resonator coupling regimes.

The optical transmission spectrum of the figure (2.12a) shows the shape of the cavity resonance.

Under coupling: $\tau_0 < \tau_e$, the losses dominate (the resonator transmission is such that: $0 < T(0) < 1$).

Critical coupling: $\tau_0 = \tau_e$, the losses are equal to the coupling rate (the transmission drops to zero: $T(0) = 0$).

Over coupling: $\tau_0 > \tau_e$, the intrinsic losses are lower than the extrinsic losses. (the transmission resonance is such that $0 < T(0) < 1$).

Transparency: $1/\tau_0 \to 0$, the resonator is lossless and coupled system is fully transparent ($T(0) = 1$).

Selective amplification: $\tau_0 < -\tau_e < 0$, there is a gain inside the resonator and system acts like an amplifier, $\tau_0 < 0$ but it does not reach the lasing because the coupler leaks are not compensated $|\tau_0| < \tau_e$ (transmission is $T(0) > 1$).

Laser: $\tau_0 \to -\tau_e$, the internal gain is such that the losses of the coupler are compensated: $|\tau_0| = \tau_e$. According to Eq. (2.25), the transmission goes to infinity and reaches laser oscillations. Obviously, infinity is not a common physical quantity. A generalized transfer function must be introduced to describe the laser regime [1].

2.4.2.2 Q-factor and coupling coefficients

The cavity Q-factor is also expressed in terms of resonance frequency and resonances width:

$$Q = \frac{\nu_0}{2\delta_{1/2}} \tag{2.27}$$

where $\nu_0 = \omega_0/(2\pi)$ is the optical frequency. If we link this Q-factor from the damped harmonic approach to the one obtained by the matrix approach of Yariv [105] through a high finesse approximation, we obtain:

$$Q = \frac{\omega_0 \tau_L \sqrt{a\varrho}}{2(1-\sqrt{a\varrho})} = \frac{\omega_0 \tau}{2} \tag{2.28}$$

Where, a is the loss term of the cavity (internal cavity loss) and ϱ is the field transmission coefficient of the coupler. It is connected to the coupling coefficient (κ) in the case of a lossless coupler, by $\varrho^2 + \kappa^2 = 1$. We may then define an intrinsic quality factor Q_0 limited by the losses of the resonator ($\varrho = 1$):

$$Q_0 = \frac{\omega_0 \tau_L \sqrt{a}}{2(1-\sqrt{a})} = \frac{\omega_0 \tau_0}{2} \tag{2.29}$$

Extrinsic quality factor is limited by the coupling with the access line ($a = 1$):

$$Q_e = \frac{\omega_0 \tau_L \sqrt{\varrho}}{2(1-\sqrt{\varrho})} = \frac{\omega_0 \tau_e}{2} \tag{2.30}$$

Then τ_0 and τ_e are written:

$$\tau_e = \frac{\tau_L \sqrt{\varrho}}{2(1-\sqrt{\varrho})} \tag{2.31a}$$

$$\tau_0 = \frac{\tau_L \sqrt{a}}{2(1-\sqrt{a})} \tag{2.31b}$$

After simplification, we obtain the intensity of round trip attenuation coefficient $|a|^2$ and intensity coupling coefficient $|\kappa|^2$

$$|a|^2 = 1 - \frac{2\tau_L}{\tau_0} \tag{2.32a}$$

$$|\kappa|^2 = \frac{2\tau_L}{\tau_e} \tag{2.32b}$$

In Eq. (2.32a), $\tau_0 < 0$ corresponds to an optical attenuation, whereas $\tau_0 > 0$ corresponds to an optical gain. This correspondence will give us the information on Brillouin gain and different coupling regimes.

An important factor, in stationary approach, is the ability to discriminate the coupling regime. In particular, it might happen that equivalent spectral signatures are obtained for over and under coupling regime configurations. In stationary regime over and under coupling regimes cannot be discriminated by a spectral analysis because τ_0 and τ_e are playing the same role in transmission (see Eq. (2.25)). This discrimination is requested to get the intracavity Brillouin gain, the dynamical approach can overcome this difficulty.

2.4.3 Dynamical approach

In case of dynamic approach, we introduced in Eq. (2.22) an angular frequency ω, which is varying in time according to the equation:

$$\omega(t) = \omega_i + \frac{V_s}{2} \times t \tag{2.33}$$

where V_s, the angular frequency sweeping speed. For experimental convenience, we also define $\tilde{\mathrm{V}} = V_s/2\pi$, the frequency scanning speed. Considering this change and solving the Eq. (2.20), we can write the mode amplitude as:

$$u(t) = \sqrt{\frac{2}{\tau_e}} S_0 \exp\left(i\omega_0 t - \frac{t}{\tau}\right)\left[f(t) - f(0) + \frac{1}{i(\omega_i - \omega_0) + 1/\tau}\right] \tag{2.34}$$

$$f(t) - f(0) = \int_0^t \exp\left[i\phi(t') + (1/\tau - i\omega_0)t'\right]dt' \tag{2.35}$$

Which can be expressed using the complex error a function erf(z) with z ϵ C:

$$f(t) = -\sqrt{\frac{i\pi}{2V_s}}\exp\left[\frac{-i(2\pi\delta_i - i/\tau)^2}{2V_s}\right]\mathrm{erf}\left(\frac{i/\tau - 2\pi\delta_i - V_s t}{\sqrt{2iV_s}}\right) \tag{2.36}$$

Analytical expression of transmission can be expressed as a function of time:

$$T(t) = \left|\frac{2}{\tau_e}S_0\exp\left(i\omega_0 t - \frac{t}{\tau}\right)\left[f(t) - f(0) + \frac{1}{i(2\pi\delta_i) + 1/\tau}\right] - 1\right|^2 \tag{2.37}$$

where we define $2\pi\delta_i = \omega_i - \omega_0$ as the initial detuning. Here, we can see that τ_0 and τ_e are not interchangeable in the analytical expression of the transmission in Eq. (2.37). For a given coupling regime, τ_0 and τ_e are fixed, and transmission depends only on the speed of scanning (V_s).

Figure (2.13) shows calculated transmission for different scanning speeds in case of a critical coupling configuration. Scanning speed $\tilde{V}_S$ is proportional to the normalized sweeping speed $\tilde{V}_0 = 2/(\pi\tau^2)$, considering a resonance width $(1/(\pi\tau))$ swept in a duration equal to the photon lifetime $\tau/2$. Figure (2.13a) is obtained by slowly scanning the laser frequency of the probe signal ($\tilde{V}_S$=0.0075 $\tilde{V}_0$). The plotted transmission (Eq. 2.37)) is very similar to the stationary regime. When scanning speed increases, we can observe the appearance of oscillations on the transmission (Figure 2.13b). This ringing is a signature of the transient response of the resonator. Increasing the sweeping speed (Figure 2.13 c and d), enlarge the number of oscillations that can be observed. These oscillations result from the interference between the light coupled inside the resonator at frequency ν_0 and the sweeped probe signal frequency $\nu(t)$. These oscillations refer to the phenomenon of ring down [106, 107, 108]. This ringing effects enable the phase of the field inside the resonator to be obtained and then the coupling regime to be determined.

Figure (2.14a) shows the transmission of a resonator in the over and under coupling regimes in the stationary or very slow frequency sweeping regime (see Eq.(2.25)). Since τ_0 and τ_e play the same role in the transmission function T, the two responses are precisely the same. By increasing the sweeping frequency rate, the responses of each coupling regime are sharply different, which allows us to determine the coupling regime as shown in figure (2.14b).

In the following section, the experimental results will be compared to the transient response of the resonator by using the analytical model (Eq.(2.37)) presented above. The

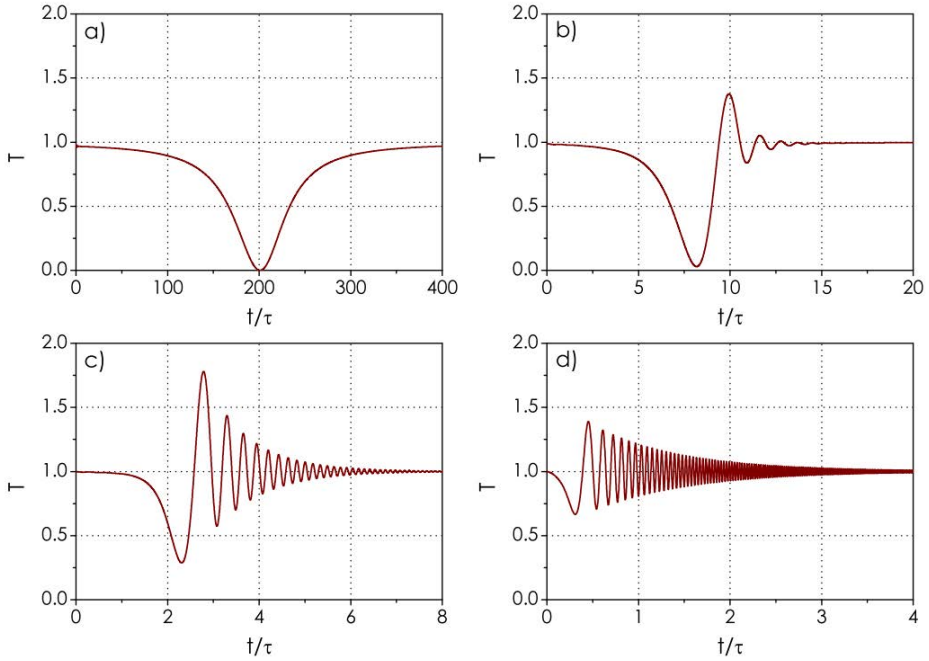

Figure 2.13: Transmission of a resonator for different scanning speeds.(a) $\tilde{V}_S$=0.0075 $\tilde{V}_0$,(b) $\tilde{V}_S$=0.3 $\tilde{V}_0$, (c) $\tilde{V}_S$=3 $\tilde{V}_0$, (d) $\tilde{V}_S$=30 $\tilde{V}_0$ with a $\tilde{V}_0 = 2/(\pi\tau^2)$ [1].

fitting procedure will allow us to deduce the experimental parameters :V_s, τ_0, and τ_e. The information of intrinsic losses or gain of the cavity is obtained from τ_0. This helps us to find the Brillouin gain inside the cavity.

2.4.4 Estimation of Brillouin gain coefficient

The gain G of the ring cavity can be experimentally evaluated with CRDM. It follows that the coefficient g_B can be calculated from Eq. (2.14). Note that the fiber is polarization maintaining ($k_{polar} = 1$). G is the total gain along one round trip inside the cavity and may be written:

$$G = a^2 = \beta e^{-\alpha_f L} e^{g_B P_{cav} L_{\text{eff}}/A_{\text{eff}}} = a_{\text{op}}^2 e^{g_B P_{cav} L_{\text{eff}}/A_{\text{eff}}} \tag{2.38}$$

where β gives the inner local losses, α_f the fiber losses coefficient, A_{eff} the effective fiber mode area and L_{eff} the usual effective interaction length. a_{op}^2 is the intensity round trip attenuation of the cold cavity mode without stimulated Brillouin scattering. P_{cav} is the pump intensity inside the cavity.

As can be seen in Eq. (2.38), when the pump intensity P_{cav} is increased, it allows to progressively compensate linear cavity losses. Thereby, intensity round-trip attenuation

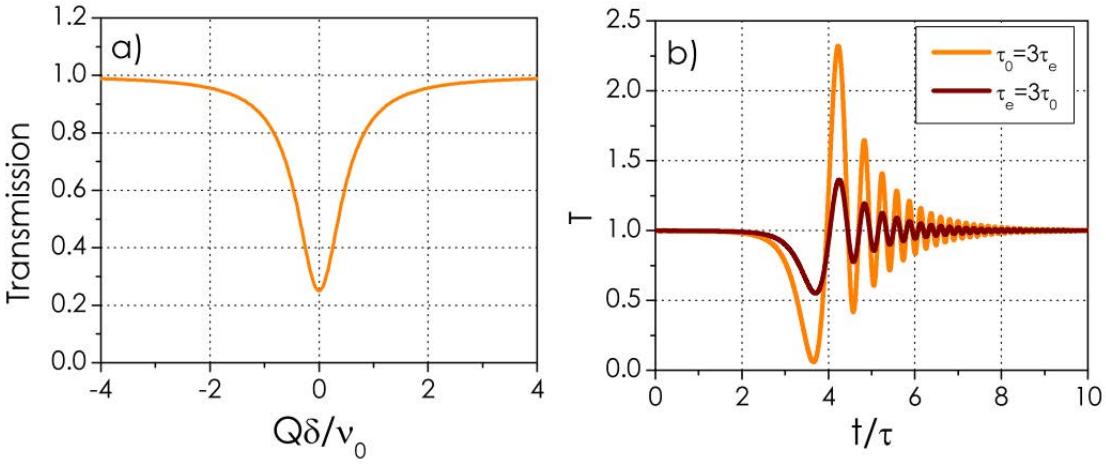

Figure 2.14: (a) Transmission in the stationary regime as a function of the normalized detuning in the case of $\tau_0 = 3\tau_e$ and $\tau_e = 3\tau_0$. The two curves are exactly superimposed. (b) Transmission as a function of time in the same two cases with $V_s = 2.25V_0$. Note that the two responses are easily distinguishable [1].

a^2 and intrinsic photon lifetime τ_0 can be tuned through the pump intensity keeping the coupler lifetime constant.

We can evaluate experimentally using CRDM, τ_0 and then $a^2 = 1 - 2\tau_L/\tau_0$. The experimental estimation of the Brillouin gain coefficient can be obtained from Eq. (2.38):

$$g_B = \frac{A_{\text{eff}}}{P_{cav} L_{\text{eff}}} \ln \frac{a^2}{a_{\text{op}}^2} \tag{2.39}$$

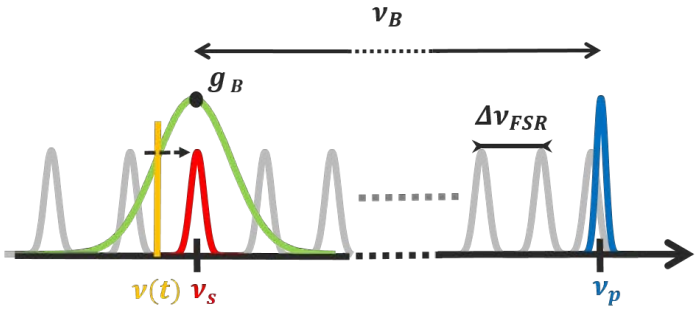

Figure 2.15: Spectral overview of the CRDM method: Pump laser line (blue), Brillouin gain curve (green), probed cavity mode (red) and probing laser line (yellow). ν_B corresponds to the Brillouin shift, where $\Delta\nu_{FSR}$ stands for the spectral spacing (Free Spectral Range) between cavity modes.

We consider the Brillouin scattering in the ring cavity based on a non-resonant pumping system. Figure (2.15) shows the schematic of Brillouin gain in the ring cavity. The

blue line corresponds to the pump signal at frequency ν_p that produces a Stokes gain (green curve) through the SBS process. In the background of the figure, one can see the periodic distribution of the ring cavity modes (gray lines).

Nevertheless, the perimeter of the resonator, that fixed the free spectral range of the cavity ($\Delta\nu_{\text{FSR}}$), and the spectral distribution of the gain curve ensure to favor the amplification of one cavity mode (red color line), that we call the Stokes mode. We consider that the Stokes mode at the frequency ν_s is at the frequency of the maximum of the gain. Using the CRDM technique, a probe signal $\nu(t)$ (yellow color line on figure 2.15) sweeps across the resonance. The probe is swept with a speed of V_S, which gives a transient response. As we have seen before, when the pump input power is increased, the gain will also increase as well as the cavity lifetime. Using the Eq.(2.37), we fit this transient response of the cavity that will give the τ_e and τ_0 value. By knowing this value we can calculate the Brillouin gain coefficient using Eq.(2.39). This method allows us to characterize the cavity and Brillouin gain coefficients inside the cavity. In the next section, we will discuss the experimental setup for gain characterization and its results.

2.4.5 Experimental setup for Brillouin gain measurement using CRDM

In this section we detail the experimental setup and measurement method. It is organized in three paragraphs, which described the fiber cavity, the Brillouin laser setup and the CRDM method. The CRDM experimental setup is presented in figure. (2.16).

The fiber cavity is composed of a $L = 20\ m$ polarization maintaining silica fiber distributed as $L_1 = 19$ m from coupler to circulator port 2 and $L_2 = 1$ m between circulator port 3 and coupler. The effective interaction length has to be precisely determined to optimized the evaluation of g_B. For our cavity configuration, $L_{\text{eff}} = L_1 + |\varrho^2| \times L_2 = 19.9 \pm 0.6\ m$ where the coupler transmission coefficient $|\varrho^2| = (1 - |k^2|)$ is introduced to incorporate the pump intensity attenuation through the coupler. The effective area of the fiber is $A_{\text{eff}} = 84.9\ \pm 0.2\ \mu\text{m}^2$. The cavity is coupled to the input/output fiber by a 95/5 coupler.

The pump is a single mode laser (pump) centered at 1550 nm. The pump intensity is amplified through an Erbium Doped Fiber Amplifier (EDFA). The input power is controlled by a variable optical attenuator. 1 % of the pump is extracted through

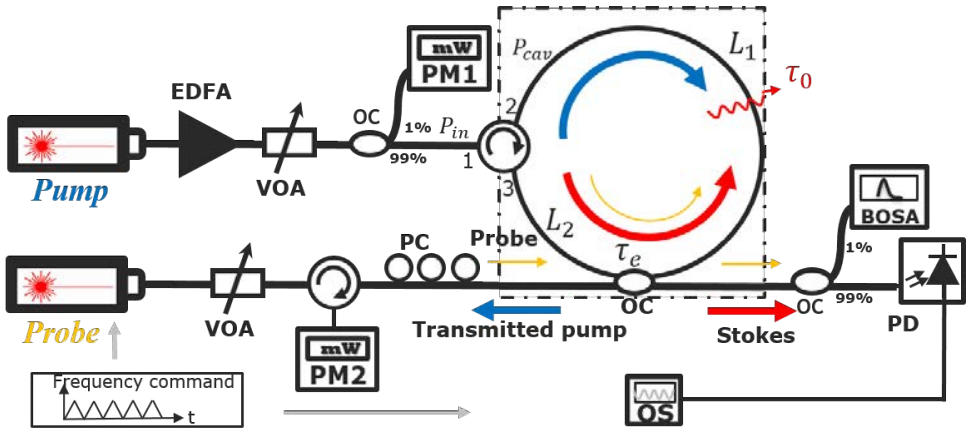

Figure 2.16: a) Experimental setup for Brillouin gain cavity ringdown determination. EDFA: Erbium-doped fiber amplifier, VOA: Variable optical attenuator, OC : Optical coupler, PC: Polarization controller, BOSA: Brillouin optical spectrum analyzer, PM : Powermeter, PD : Photodectector, OS : Oscilloscope.

a coupler for intensity power monitoring (PM1). The remaining part P_{cav} of the laser pump intensity P_{in} is coupled to the cavity by a circulator. Both quantities can be related through, $P_{cav} = \alpha_{12} P_{in}$, where $\alpha_{12} = 0.758$ is the combined losses of the circulator and connectors. The circulator ensures a single pass to the pump signal in the fiber loop preventing re-injection. For sufficient pump intensity, the stimulated Brillouin Stokes signal is generated in the opposite direction of the pump signal. Extracted Stokes signal is analyzed spectrally thanks to a high-resolution Brillouin Optical Spectrum Analyser (BOSA), while a photodetector records the intensity. This setup is a non resonant Brillouin laser with a threshold of $P_{th} = 61.8$ mW. Lasing properties of this non-resonant Brillouin laser is detailed in the next chapter.

Now we describe the CRDM setup. All the measurements are performed for a pump power P_{in} lower than the pump power lasing threshold P_{th} to be within the validity domain of the technique [97]. The probe signal is provided by a tunable laser (Tunics OM). Before entering the cavity, the signal intensity is controlled by a variable optical attenuator (VOA), and its polarization is adjusted through a polarization controller (PC). The probe laser frequency is positioned close to the Stokes mode, thanks to a 10 MHz - resolution spectrum analyzer (BOSA). The frequency of the probe signal is continuously swept across the resonant Stokes signal by a frequency command allowing to adjust the sweeping speed and the scanning frequency range. A photodetector then collects the transmission of the cavity mode that is observed on an oscilloscope triggered by the

frequency command.

2.4.6 Results and discussions

CRDM signals are collected for input pump powers varying from 0 to P_{th}. Figure (2.17) presents various CRDM signals collected for pump power ranging from 13.84 to 59.46 mW (red color curves). The normalized transmission is plotted as a function of time. On increasing pump power, the amplitude and number of frequency oscillations increase. To get more insight on those specific temporal signatures, data are fitted using the procedure described above and allows to determine τ_0 and τ_e as a function of P_{in}. As expected the τ_e value is constant for all the measurements (see table (2.1)).

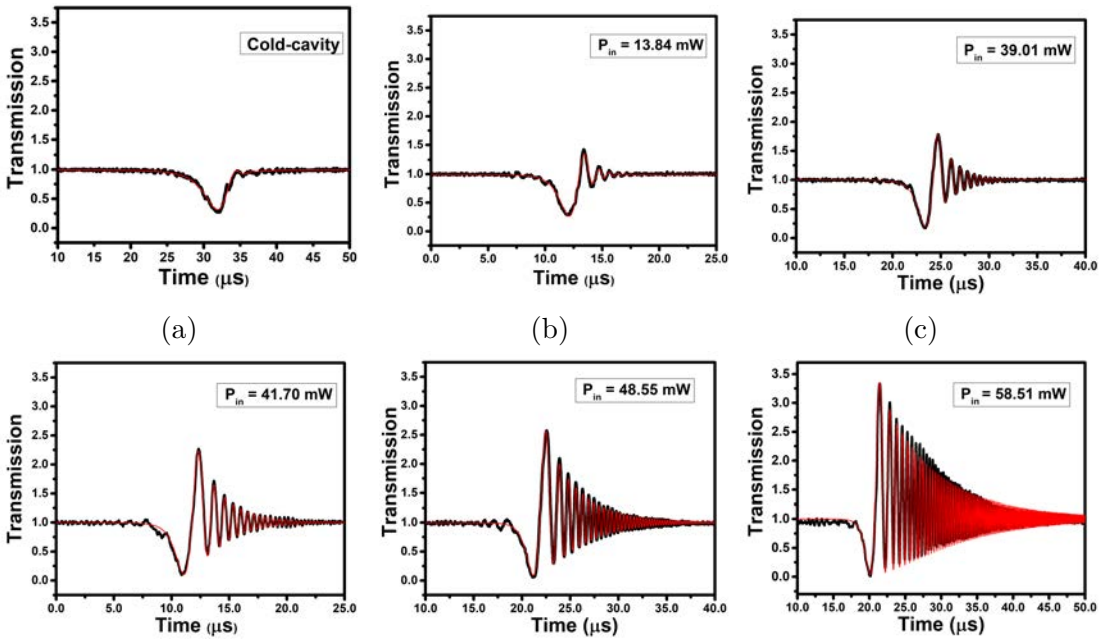

Figure 2.17: Fast scanning profiles recorded from the Brillouin cavity at different pumping power (P_{in}) with a scanning speed of 2.8 $MHz/\mu s$: The intrinsic photon lifetime (τ_0), transmission and Brillouin gain coefficients are deduced from the analytical fits (red) of experimental curve (black). (a) cold cavity, (b) under coupling, (c) near to critical coupling, (d) over coupling, (f) near to transparency, (g) amplification.

For $P_{in} = 0$ mW, the cold cavity parameters are extracted: $\tau_e = 3.80$ μs and $\tau_0 = 1.20$ μs. Using the definition $Q = 2\pi\nu_S\tau/2$, we get an estimation for the loaded quality factor of 5.6×10^8. When, P_{in} is varied from 13.84 to $50.14mW$, τ_0 increases, modifying the coupling regime from under coupling (cold cavity) towards the transparency regime through the critical coupling and over-coupling. For $50.14 < P_{in} < P_{th}$, τ_0 takes a negative value

corresponding to the amplification regime. The variation of τ_0 as a function of the pump power refers to a progressive compensation of the linear losses until the amplification regime.

Table 2.1: Parameters obtained from the fitting of ringing profiles at different pump powers

P_{in} [mW]	τ_e [μs]	τ_0 [μs]	Coupling regime	g_B [m/W]
only probe	3.80	1.20	–	–
13.84	3.20	1.56	undercoupling	1.71×10^{-11}
17.22	3.34	1.67	undercoupling	1.67×10^{-11}
27.30	3.43	2.52	undercoupling	1.98×10^{-11}
39.01	3.94	3.82	critical coupling	1.78×10^{-11}
41.70	3.46	8.99	overcoupling	2.06×10^{-11}
43.87	3.87	0.33	overcoupling	2.17×10^{-11}
48.55	3.84	735400	transparency	2.03×10^{-11}
50.14	3.78	−7483500	transparency	1.96×10^{-11}
52.02	3.61	−0.22	amplification	1.98×10^{-11}
55.87	3.81	−0.12	amplification	1.91×10^{-11}
58.51	3.86	−6.70	amplification	1.96×10^{-11}
59.46	3.58	−5.26	amplification	2.00×10^{-11}

Figure (2.18) shows the transmission at the resonance of Brillouin cavity in decibels as a function of $1/\tau_0$ for different regimes, red squares are the estimated values from the gain characterization. The pump power changes the cavity gain; this leads to a change in coupling regime from undercoupling to amplification. From those fitted data, we can retrieve a^2 from Eq. (2.38) and then the value of the Brillouin gain g_B by use of Eq. (2.39). Table (2.1) shows calculated gain for different coupling regimes.

Figure (2.19) summarizes the extracted gain values as a function of the pump power. The mean value (red dashed line) is equal to 1.94×10^{-11} m/W with a standard deviation (shaded green region) of $\pm 1.5 \times 10^{-12}$ m/W. The uncertainty contribution to g_B related to A_{eff}, L_{eff} and P_{cav} gives 0.6×10^{-12} m/W and do not enlarge the experimentally determined standard deviation of g_B. We can then conclude that the Brillouin gain standard deviation is related to the experimental extraction of τ_0. In the next section, we will compare the extracted Brillouin gain coefficient from CRDM with self-heterodyne and pump-probe methods.

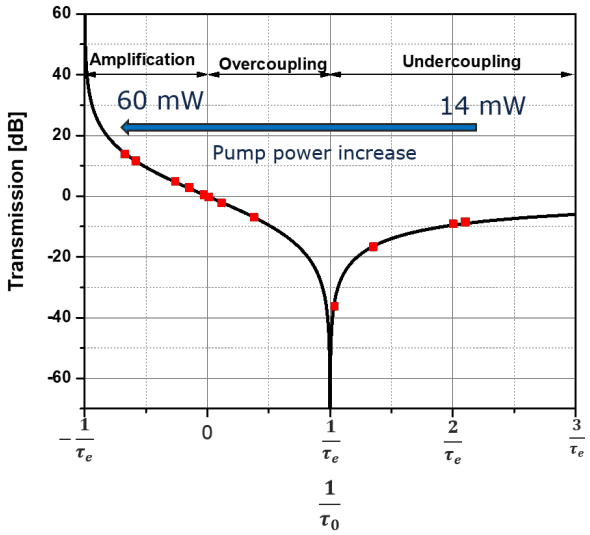

Figure 2.18: Resonant transmission obtained from the fitting of ringing profiles in the Brillouin cavity. This figure is inspired from article [2].

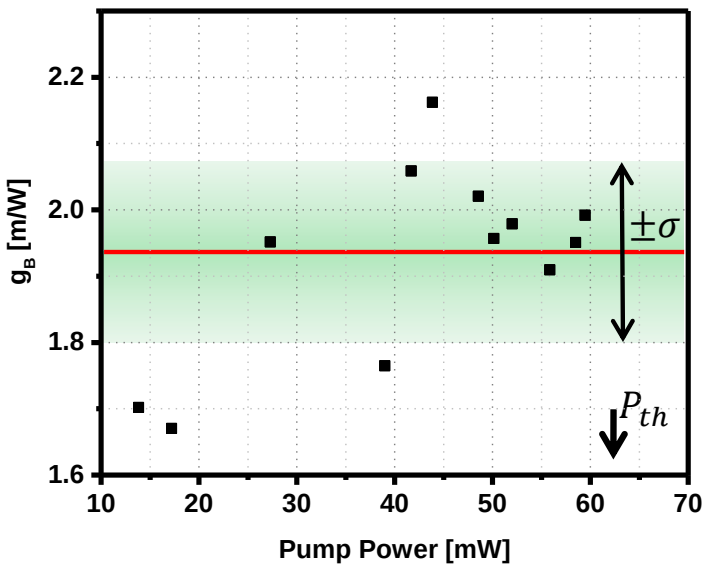

Figure 2.19: Brillouin gain coefficient extracted from the CRDM signal for various input pump powers. The mean value is equal to $g_B = 1.94 \times 10^{-11} \pm 1.5 \times 10^{-12}\ m/W$.

2.4.7 Comparison with other methods

To evaluate the relevance of the method, we compare our Brillouin gain estimation through the CRDM technique to other references, for which Brillouin gain bandwidth is experimentally estimated by self-heterodyne [93] and pump-probe [80, 79, 109] techniques. These methods are applied to similar single-mode telecom fibers with around 3 % GeO_2. The Brillouin gain bandwidth is experimentally estimated to be $\Delta\nu_B = 27.5 \pm 2$ MHz. Then, using Eq. (2.11) the gain coefficient can be determined. As mentioned before, this determination depends on the material parameters of the used fiber. Fabrication process conditions (doping, temperature, etc.) affect those parameters. For example, a commercial single-mode fiber in the C band region usually has a GeO_2-doping concentration of a few percent, but this value is usually unknown.

Table 2.2: Comparison of g_B values obtained for single mode silica fibers [5] in various works. SH stands for self-heterodyne.

Methods	g_B value [$\times 10^{-11}$m/W]	standard deviation [$\pm 10^{-12}$m/W]
CRDM [our work]	1.94	1.5
SH [silica value]	2.45	1.8
SH [3% GeO_2 value]	1.92	1.4
Pump-Probe [silica value][79]	2.29	-
Pump-Probe [3% GeO_2 value][92]	1.98	-
Pump-Probe [3% GeO_2 value][80]	2.07	-

Table 2.3: Material values for pure and 3% GeO_2 doped silica fibers.

Parameters	SiO_2 [79]	$SiO_2 + 3\%GeO_2$ [110]
Refractive index [n]	1.45	1.46
Elasto-optic coefficient [p_{12}]	0.271	0.236
Density [$\rho(kg.m^-2)$]	2200	2244

We report in table (2.3) material values for pure silica and 3%-doped GeO_2 silica fiber from different journals. Using those parameters, Brillouin gain coefficient estimation gives 2.45 and 1.92 $\times$ 10^{-11} m/W (see Table 2.2) for silica and 3% GeO_2 doped silica fibers respectively. The standard deviation, related to $\Delta\nu_B$ determination, is bounded between $\pm 1.4 \times 10^{-12}$ m/W $< \sigma < 1.8 \times 10^{-12}$ m/W. The g_B estimation obtained from the CRDM technique is very close to the one obtained by self-heterodyne using the parameters of a commercial monomode fiber 3%-doped with GeO_2. Upon this example, we see that

Table 2.4: Parameters of a 3% GeO_2 doped silica fibers

Parameters	Values	References [92]	References [80]
Effective area [A_{eff}]	84.90 μm^2		
Length [L]	26 km		
Loss coefficient [α_f]	0.20 dB/km		
Polarization coefficient [K]	1.50		
Brillouin shift [ν_B] GHz	10.87	21.20	12.84
Acoustic velocity [V_A] $\frac{m}{s}$ (Calculated from 2.7)	5770	6011	5804
Wavelength [λ_p] nm	1550	828	1320
Bandwidth [$\Delta\ \nu_B$] MHz	27.50 ± 2	90	35
Brillouin threshold [P_{th}] mW	4.70 $\pm .8$		

the material parameters impact the estimation of the Brillouin gain. Comparison to other works on similar silica fibers (see Tab. 2.2) give comparable g_B values extracted using the CRDM. Pump-Probe gain coefficient values are calculated using Eq (2.11) with parameters shown in tables (2.3) and (2.4).

In conclusion, CRDM method is explained and demonstrated on a Brillouin cavity. We show that CRDM can be used to identify the coupling regime of the cavity by analyzing the intrinsic and extrinsic photon lifetimes. It will help to optimized the laser threshold and laser noise. Also, we show that the CRDM technique can be used in Brillouin gain coefficient characterization in a cavity configuration. Moreover, we measure the Brillouin gain coefficient of SMF-28 fiber with different measurement methods and compared to CRDM; the measured values give a good agreement.

2.5 Conclusion

In this chapter, we have reviewed the spontaneous and stimulated Brillouin scattering in optical fiber. We have explained the generality about Brillouin gain and threshold in optical fiber. We have also discussed several approaches for measuring the Brillouin gain coefficient. We have measured the Brillouin gain coefficient using the self-heterodyne method and have validated it using Brillouin threshold determination in SMF-28 fiber. We have demonstrated that CRDM can be used to characterize Brillouin gain coefficient in high-Q resonators. On contrary to usual technique this method through a simple and single-pass measurement gives access to the Brillouin gain coefficient of the material constituting the cavity. We have reviewed the CRDM principle and extracted cavity parameters like Q-factor, intrinsic and extrinsic photon lifetimes, which will help us to

optimize the Brillouin laser threshold and noise performances as it will be explained in the next chapters. The proof of concept has been experimentally demonstrated with a fiber ring resonator. CRDM allowed us to determine unambiguously the coupling regime and to estimate the Brillouin gain coefficient of the material composing the resonator without knowledge of material constants. The self-heterodyne and pump-probe techniques are in good agreement with the CRDM. This cavity ring-down method can be applied to any resonator. The determination of Brillouin gain coefficient in microresonators, exotic material fiber rings and whispering gallery mode resonators for which usual methods do not apply could be done with CRDM.

Chapter 3

Stabilized non-resonant Brillouin fiber laser

3.1 Introduction

First Brillouin laser has been studied by Hill *et al.* [111] in 1976. Hill's cavity was rather a hybrid cavity. In addition to the fiber used as a gain medium, it consisted of massive optical components such as lenses, mirrors, and signal separators [112]. It was a Fabry-Perot configuration with a mirror at the end of the fiber. In this first SBS laser demonstration, a cascaded process of up to 14 laser lines have been observed. Later with good stabilization, laser threshold power reached hundreds of mW for Brillouin fiber ring laser [113]. In this free space configuration, nearly 70 % of the signal was lost after one round trip. In 1982, Stokes demonstrated an all-fibered Brillouin laser; fibered tunable directional coupler was used to close the cavity; this allowed him to reduce the cavity losses and the Brillouin laser threshold [114].

The first analytical study of a Brillouin laser was reported in [115]. They give a first model description allowing to express the behavior of the Brillouin laser threshold and Stokes output power. A discussion on the impact of the cavity detuning to the laser performances was also done. A pioneering work has been published in 1991 reporting a 2 kHz linewidth Brillouin laser based on a 20 meter fiber ring cavity [25].

Multi-Stokes Brillouin fiber laser (MBL) have been studied in terms of threshold conditions, efficiency, output and circulating pump power in 1993 [116]. The same group investigated the effects of temperature [117], frequency pulling [118] and frequency sta-

bility [119] of the single-mode Brillouin lasers, after which the dynamics of the Brillouin laser became a subject for several studies [120, 121, 122]. In 2000, Debut *et al.* proposed a theoretical model and predicted that the Brillouin laser linewidth can be narrowed respect to the pump linewidth by the combined influence of acoustic damping rates and cavity losses [123]; they also experimentally demonstrated 12 meters BFL with a laser linewidth, reduced by a factor of 10 [124].

Later, the intensity noise of a BFL was reported theoretically; it was shown that the pumping rate and cavity reinjection are the major parameters of the transfer function of the pump intensity noise for BFL with low finesse cavities [125]. They also predicted that the RIN of the BFL could be lower than that of pump laser RIN for some frequency regions. However, this prediction was not confirmed by their experiments due to mechanical instabilities of the BFL. In 2006, Geng *et al.* proposed an actively stabilized BFL using a PDH frequency locking technique and reported a 20 dB frequency noise reduction [126], later they reported RIN reduction of BFL by experimentally showing that the pump to Stokes noise transfer function acts as an efficient low-pass filter [127, 128].

The development of low-loss optical couplers, circulators, and gratings leads to the development of new Brillouin fiber laser configurations like non-resonant pumping [26], unbalanced Mach-Zehnder interferometer [28], Bragg grating [27], self-injection locking [29] based BFLs. Similarly, hybrid Brillouin/erbium fiber laser has been reported [30]; erbium-doped fiber is inserted inside the cavity, which enables to amplify the Stokes signal thanks to a pump; this configuration reduces the threshold and laser noises, which are reported in different articles [129, 130, 131, 132]. In past decades, Brillouin fiber lasers have been demonstrated in different geometries and materials fibers, like silica photonic crystal fiber [133], tellurite fiber [24, 134, 135, 136], chalcogenide fibers including step-index [137], suspended core [138] and microstructured [139]. Even though some of the first experimental observations of Brillouin scattering were done in liquids [140] and gases [141], after a few decade, first liquid Brillouin laser was demonstrated in integrated liquid-core fiber filled with CS_2 [142]. Similarly, CO_2 filled Hollow-core fiber-based gas Brillouin laser was reported [143] with 33.2 mW of threshold. These two works have opened a new class of Brillouin lasers.

In 2009, Tomes and Carmon observed SBS in spherical silica resonator where the optical and acoustical modes are whispering-gallery modes (WGM) [144]. Luckily, the higher-order optical WGM-modes have a frequency separation of 11 GHz that corresponds to

the SBS shift at the 1550 nm pump wavelength. Brillouin lasing threshold of 26 μW with 90 % of slope efficiency was observed. In the same year, Grudinin *et al.* demonstrated the Brillouin laser in 5 mm diameter of CaF_2 WGM resonator, which gives a longitudinal frequency spacing closed to the SBS shift of 17.7 GHz at 1064 nm pump wavelength. The laser threshold is obtained at 3 μW, with significant cascading effects observed at higher pump powers [145]. These WGM Brillouin lasers are obtained by the phase-matching of random spacing between the different optical mode families. In 2012, the group of Vahala introduces Brillouin lasers using a chemically etched ultrahigh-Q wedge resonator on a silicon chip [146]. This resonator is made through a lithographic process, which enables to create microresonator with sub-MHz precision in resonator spacing and high Q-factor (875 millions). Using this resonator, the Brillouin lasing is observed at 50 μW. Also, they obtained a significant linewidth narrowing and cascading effect in this Brillouin laser at 1550 nm pump wavelength [147]. Moreover, these cascaded Brillouin laser signals are used to demonstrate the microwave generation, in which noise performances are comparable to commercial signal generators [148]. More recently low-noise cascaded Brillouin laser was used for the realization of optical gyroscope [149, 150]. In 2014, the group of Vahala demonstrated a Brillouin laser at 1064 nm pump wavelength from an ultra-high-Q silica wedge disk resonator on silicon with a 0.1 Hz^2/Hz fundamental frequency noise [151]. Later, variety of microresonator based Brillouin lasers were demonstrated and studied, such as silica-based microsphere [152, 153], micro-rods [154, 155], micro-bottle [156], microbubbles [157] and toroid microcavity [31]. Moreover, microresonator Brillouin lasers were demonstrated with different materials, other than silica as microdisks of barium fluoride [158], strontium fluoride [159], tellurite microspheres [160] and silicon-oil droplet microsphere [161]. However, these microresonators can achieve SBS lasing at low optical power but they are not fully compatible with large-scale optical integration. One alternative is to use an integrated planar ring resonator coupled to a waveguides.

In 2013, Kabakova *et al.* demonstrated efficient Brillouin lasing using a 20 meters As_2S_3 chalcogenide chip [162]. Due to high insertion loss (5.5 dB) of the chalcogenide chip, a high laser threshold of 330 mW was obtained with a 30 % slope efficiency. Even with very high roundtrip losses, they observed 10 dB linewidth reduction compared to that of the pump laser. In 2018, Gundavarapu *et al.* reported sub-hertz fundamental linewidth integrated Brillouin laser in Nature Photonics [163]. The laser ring resonator composed of silicon nitride (Si_3N_4) on silica (SiO_2). Although the SBS gain is low in

Si_3N_4 [22], the low optical propagation losses of the materials (0.4 dB/m) and 7.43 cm long cavity help to obtain a Q-factor of 28 millions, which leads to a lasing at a relatively low pump threshold of 14.6 mW. This Brillouin laser highlights a 0.7 Hz fundamental linewidth. Even though these microresonators and integrated Brillouin lasers shows a Hz level fundamental linewidth, their integrated linewidth is of the order of pump laser linewidth because these cavities are more sensitive to thermo-refractive fluctuations [164].

This problem can be reduced by a larger mode volume cavity with a short fiber ring resonator. In 2019, Loh *et al.* addressed this issue and demonstrated an integrated linewidth of 20 Hz by using a high-Q resonator consisting of 2 meter polarization-maintaining (PM) fiber [165]. The group of Loh showed that high-Q fiber resonator SBS laser can be used as reference sources for portable optical atomic clocks [166].

All the above mentioned Brillouin laser can be classified into two categories: **non-resonant and resonant pumping**. In the first case, the pump is not resonant or it makes a single pass within the cavity, which will be explained in details in this chapter. For the second case, the pump is seeded in a resonant mode in order to circulate inside the cavity, which will reduce the laser threshold when compared to the non-resonant case. The resonant pumping will be studied in the chapter 4.

In the Institut FOTON, resonant and non-resonant Brillouin lasers are studied. In the thesis of Kenny Hey Tow [33], non-resonant Brillouin lasing was realized with suspended core [167] and microstructured chalcogenide fibers [138, 139]. In the first case, non-resonant Brillouin laser was constructed using 3 meters of suspended core $As_{38}Se_{62}$ chalcogenide fiber with silica components. A Koheras laser was used as a pump at 1550 nm wavelength. A lasing threshold of 22 mW with a 26 % slope efficiency was observed. 5 and 6 dB reduction in relative intensity and frequency noise were observed when compared to the pump laser noise respectively [138]. In the second case, 3 meter microstructured GeAsSe fiber was used as a gain medium. At a higher pumping power, two Stokes orders were observed due to Fresnel reflections at chalcogenide fiber facets. The first Stokes in this experiment acts as a pump for the Stokes 2. The linewidth of the pump, Stokes 1 and Stokes 2 were measured to be 4 MHz, 270 kHz, and 20 kHz respectively and approximately 23 dB linewidth narrowing was observed in the cascading process [139].

In the thesis of Schadrac Fresnel [34], were studied both configurations of the Brillouin laser with silica fiber. In the first case, the non-resonant Brillouin laser was constructed

using a 20 meters silica fiber and lasing was observed at 60 mW of pump power. The RIN of the BFL was studied as a function of pump power. Nearly a 40 dB frequency noise reduction was observed in this cavity. In the second cases, resonant Brillouin laser was demonstrated by 20 meter fiber ring cavity; the pump and Stokes were resonant. Multiple Stokes order were observed and studied and their power dynamics gave similar results as in [116, 168]. The RIN behavior of the first three Stokes orders were studied and it was observed a 20 dB RIN reduction in the clamping regime [34]. Unfortunately the measurement of the frequency noise of the resonant Brillouin laser was limited by the noise floor of the measurement bench eventhough the Brillouin laser was studied in different configurations.

In this thesis, objectives were to identify key parameters in Brillouin fiber lasers and especially their influence on noise properties by taking benefits of the initial work that was done in the lab.

In this chapter, we will focus on the non-resonant Brillouin laser. Firstly, we introduce non-resonant Brillouin laser architecture in section (3.3). After that, the characterization of non-resonant Brillouin laser is explained. In section (3.4) we will describe the experimental setup and will address the issue of mode-hopping in non-resonant Brillouin laser. We propose a new mode-hopping suppression method based on PDH locking. Finally in section (3.6), we will study the frequency noise reduction of non-resonant BFL experimentally and analytically. Moreover, we have realized a mHz linewidth Brillouin laser using cascading of two non-resonant BFL.

3.2 Condition for Brillouin lasing effect

Generally, a laser is obtained by inserting an amplifying medium inside an optical cavity. The optical amplification is performed by a population inversion, which favors the stimulated emission. In the case of a Brillouin laser, the resonant optical mode amplification is carried out by stimulated Brillouin scattering. Then the generated Stokes wave is circulating in the opposite direction to that of the pump wave. The laser can oscillate only on cavity modes covered by the Brillouin gain band. Recall that the free spectral range (FSR), which fixes the difference between two neighboring modes, is given by $\Delta\nu_{FSR} = \frac{c}{nL}$; L is the cavity length and n is the refractive index of the medium. To have a resonant mode at the Brillouin-gain maximum, it is necessary that the Brillouin shift

is a multiple of the FSR ($\nu_B = N \times \Delta\nu_{FSR}$, N is the number of cavity modes separating the pump wavelength and the gain-maximum wavelength).

If the number of modes under the gain curve is larger than 1, then the regime is called multi-mode (figure (3.1a)). Generally, it is observed in "long" fiber ring cavities because the FSR is small when compared to the SBS gain bandwidth, multi-mode regime could leads to an unstable laser operation [118, 169]. In a single-mode regime, only one mode will exist under the SBS gain curve (figure (3.1b)), which can be obtained for "short" cavities. The number of resonant modes under the gain bandwidth could be estimated for a side-mode suppression ratio of 20 dB (1 %) to N_{mode} =2.58 $\times(\Delta\nu_B/\Delta\nu_{FSR})$, (see the Appendix C). It turns out that, as the gain is not homogeneous, considering only $\Delta\nu_B/\Delta\nu_{FSR} < 1$ may be enough to have a single-mode operation. It is why we will take this ratio as a reference.

For a stable emission, it is necessary to ensure that there is only one cavity mode under the Brillouin gain curve. In practice, even if this former condition is fulfilled, a resonant mode will shift due to temperature and mechanical fluctuations [117, 119], which could lead to mode-hopping. We can avoid this drawback by applying an active locking to fix the Stokes frequency under the gain curve.

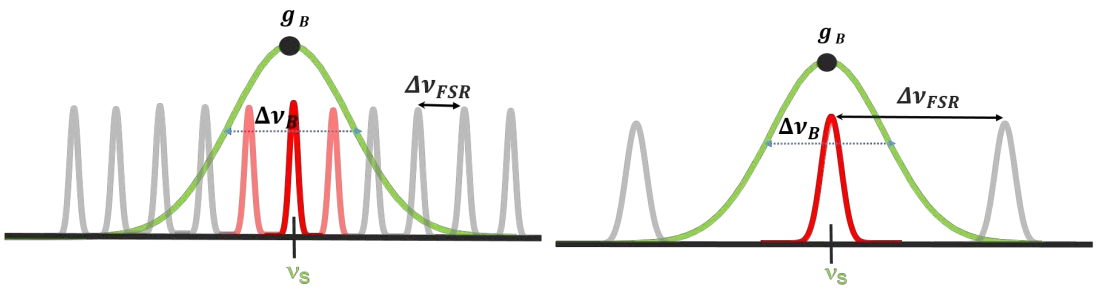

(a) multi-mode operation (b) single mode operation

Figure 3.1: Distribution of cavity modes under the Brillouin gain curve.

In conclusion, in order to get a single-mode Brillouin laser with an optimized gain, we need to fulfill two necessary conditions. The first one is that ν_B should be equal to $N \times \Delta\nu_{FSR}$. The second is that the $\Delta\nu_B/\Delta\nu_{FSR}$ should be lower than 1. It is worth mentioning that the Brillouin frequency is defined by the phase matching condition, which depends on the optical wavelength as well as the material properties.

As a matter of fact, temperature fluctuations will affect the generated Stokes frequency by two main mechanisms. The first one is linked to cavity-length fluctuations (due to temperature), which modifies the position of the resonant frequencies of the cavity comb. The second one is related to the acoustic velocity V_A in the medium, which affects the amplitude of the Brillouin shift. Pump frequency fluctuations could also shift the position of the gain maximum. This maximum is separated from the pump wavelength by the Brillouin shift. Then any pump frequency fluctuations will generate the same amplitude of frequency fluctuations of the gain maximum with respect to a resonant mode. Due to these instabilities, a resonant mode, which is located at the gain maximum, may stop lasing at the benefits of an adjacent mode. This phenomenon is called mode-hopping.

Mode-hopping is a phenomenon that a laser experiences with sudden jumps in optical frequency, which are related to the resonator stability or to mode competition in homogeneous medium. The Brillouin laser is operating in a single-frequency regime inside the resonator for some time, but then it suddenly switches to another mode due to some external perturbations. This means that different modes are sharing the pump power for a short period. Mode-hops may be due to temperature variations that will change the central Brillouin frequency of the gain or the cavity resonance frequencies. A "short" fiber cavity will increases the laser threshold; it may even experience this effect if the resonant mode is not well fixed at the maximum Brillouin gain. Moreover, Brillouin scattering and fiber cavity are firmly dependent on temperature. Resonance frequency shifts are related to the refractive index (n) and cavity length that are both temperature-dependent. Resonance frequency shifts can be written in terms of thermo-expansion ($\alpha_T = \frac{1}{L}\frac{dL}{dT}$) and thermally induced change in refractive index ($\frac{dn}{dT}$):

$$\frac{d\nu}{\nu} \approx -\frac{1}{n}\frac{dn}{n}\Delta T - \alpha_T \Delta T \tag{3.1}$$

With $\alpha_T = 0.51 \times 10^{-6}\ K^{-1}$ and $\frac{dn}{dT} = 11.6 \times 10^{-6}\ K^{-1}$ [165]. Thus at a frequency of 193.6×10^{12} Hz, the shift is 1.65 GHz for $\Delta T = 1$°C. Brillouin-shift coefficient due to a temperature variation is 1 MHz/K while it is 500 $MHz/\%$ for strain coefficient [80].

The Brillouin frequency changes also along with the pump laser wavelength (7 MHz/nm). It is a small change in comparison to the other effects, but this will depend on the pump -laser stability. For a semiconductor DFB laser, the temperature stabilization is around 1/100°C. This implies frequency fluctuations of the order of a few 10's MHz (as typical fluctuations are a few $GHz/$°C). It is equivalent to a wavelength fluctuations less than the

picometer[1]. It implies a fluctuation for the Brillouin shift of the order of a few kHz. The same conclusion can be drawn for the driving current as the stability is better than 10 μA, which means fluctuations of the order a few ten's of MHz (the wavelength dependence to a change in bias current is a few GHz/mA).

All these effects have influences on mode-hopping in the Brillouin cavity, and it limits the long term single-mode operation. Generally, mode-hopping will be suppressed in resonant Brillouin laser by a servo-loop as it will be explained in the next chapter. Usually, mode-hopping is observed in the non-resonant Brillouin laser because frequency locking scheme were rarely implemented. In this chapter, we proposed a locking method to suppress the mode-hopping in non-resonant Brillouin laser. Before going to the stabilization method, we introduce simple non-resonant Brillouin laser architecture and cavity parameters.

3.3 Description of the laser architecture

A schematics of a non-resonant Brillouin laser is shown in figure (3.2). It has been already introduced in the chapter 2 for the purpose of Brillouin gain characterization through CRDM technique. Here, we study the Brillouin lasing of this cavity. The pump laser power is injected through a circulator from port 1 to port 2. The single-mode silica fiber is used as an active medium. It is connected to a coupler to get a part of the laser signal and transmitted pump. One of the coupler ports is connected to the circulator port 3 to close the ring-cavity. It will restrict the pump transmission from port 3 to 2 of the circulator. Then, the pump wave (in blue color) is only performing one round trip inside the cavity. This single-pass pump will induce the stimulated Brillouin scattering process inside the ring cavity. The Stokes wave is generated in the opposite direction. Stokes wave (in red color) is traveling anti-clockwise direction and it will go through the circulator port 2 to 3. It can circulate for several round trips before leaving the cavity.

We consider that the relative position between the cavity modes and the Brillouin gain bandwidth is perfectly overlapping at gain maximum ($g_B(\nu) = g_B$) and also that the cavity is polarization maintained (which implies $k_{polar} = 1$). The losses coefficients of the different components are given in the table (3.1). We consider that the pump and

[1]A variation of 1 nm is equal to 125 GHz at a wavelength of 1.55 μm

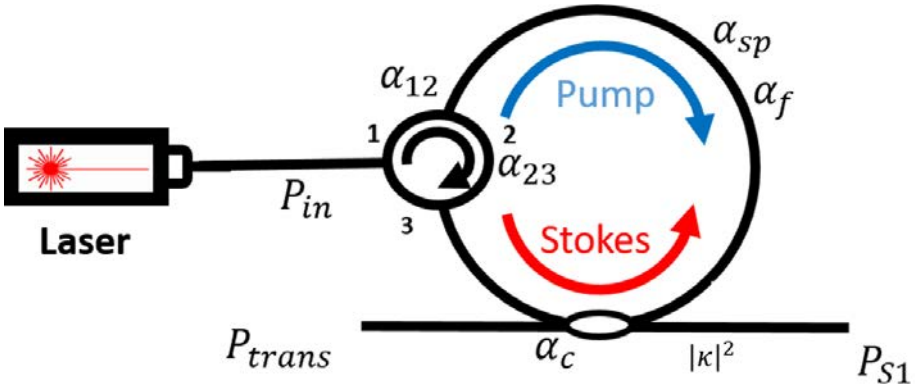

Figure 3.2: Schematic representation of a BFL cavity with non-resonant pumping showing the different losses coefficients detailed in table (3.1).

Table 3.1: Losses coefficients of each components in the cavity

Parameters	Symbol
Losses from port 1 to port 2	α_{12}
Losses from port 2 to port 3	α_{23}
Splicing losses	α_{sp}
Fiber losses	α_f
Percentage of the signal extracted from the cavity	$\|\kappa\|^2$
Coupler losses	α_c

Stokes waves will experience total losses, α_1 and α_2 respectively expressed by:

$$\alpha_1 = \alpha_{12}\alpha_{sp}\alpha_f\alpha_c \tag{3.2a}$$

$$\alpha_2 = \alpha_{23}\alpha_{sp}\alpha_f\alpha_c \tag{3.2b}$$

In the following section, we will characterize round trip losses α_2 by CRDM and describe the Brillouin laser experimental setup.

3.4 Experimental set-up

A non-resonant Brillouin laser with 20 m polarization-maintaining (PM) fiber and (95/5) % coupler with 3-port circulator to close the cavity is schematically described in figure (3.3). The cavity is passively stabilized by setting the fiber glowed on a metallic plate. The pump is a tunable C-band source (Tunics OM) associated with an erbium-doped optical fiber amplifier. A variable optical attenuator (VOA) controls the injected power so that the pump has constant noise properties in intensity and frequency as the tunable

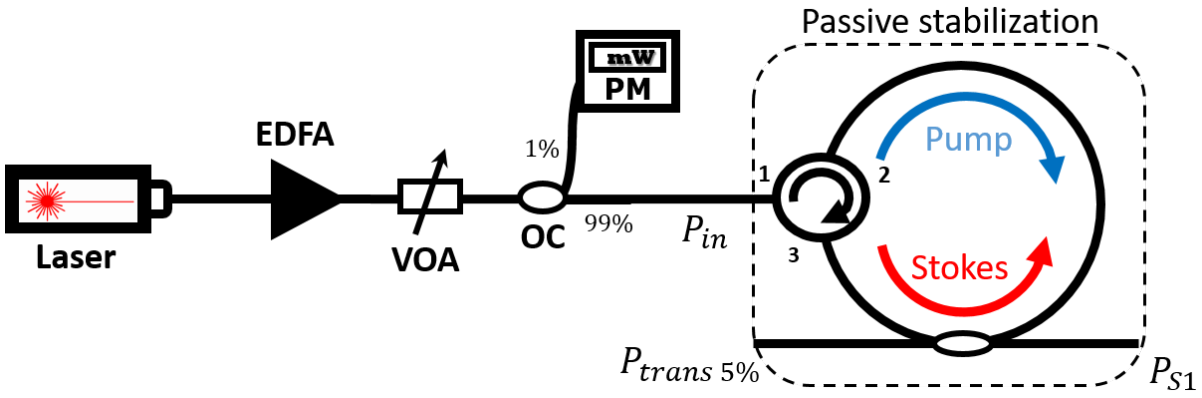

Figure 3.3: Experimental setup for non-resonant fiber ring cavity Brillouin laser characterization

Table 3.2: Parameters of the non-resonant BFL cavity

Parameters	BFL_{20PM}
L	20 m
τ_0	1.2 μs
τ_e	3.8 μs
α_2	0.83
$1 - \|\kappa\|^2$	95 %
$Q - factor$	5.6×10^8

source and the optical amplifier have a constant operating point. A 99/1 % coupler is used to monitor the input pump power. As discussed above, the pump will generate a Brillouin gain and a Stokes wave circulating in the opposite direction to that of the pump. Circulating Stokes power (P_{S1}) and transmitted pump (P_{trans}) signals are collected on the power-meter placed at the output of the coupler. BFL cavity is characterized by a cavity ring-down method as discussed in chapter 2. Using this method, we extract the intrinsic and extrinsic photon lifetimes of the cavity; this gives the total round trip losses (α_2) and Q-factors. The extracted parameters are shown in table (3.2).

3.4.1 Characterization of Brillouin laser

In this section, we discuss about the power dynamics of non-resonant Brillouin laser and characterize the Brillouin threshold. The estimation of the Brillouin laser threshold requires the measurement of Stokes power according to the input pump power. Experimental results are shown in figure (3.4*b*): Stokes output is shown in red and transmitted pump power in black. From this figure, the Brillouin laser threshold is given at 61.8

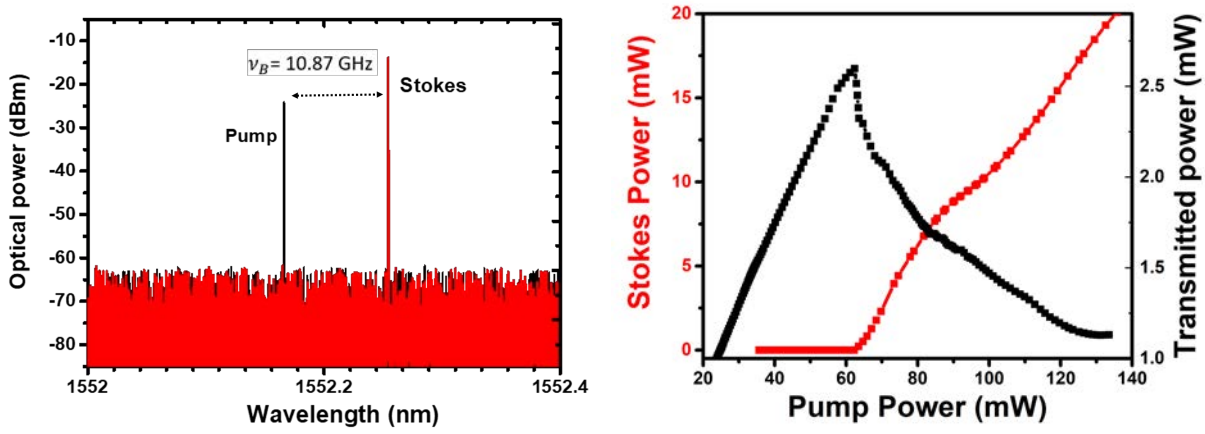

(a) (b)

Figure 3.4: (a) Optical spectrum and (b) Power characterization of the 20 m non-resonant BFL cavity

mW. Once the pump reaches the threshold of the Stokes 1, an exponential decrease in transmitted power is observed due to the excess losses from the energy transfer of the pump to the Stokes wave. The Stokes power linearly increases along with the input pump power with 25 % of slope efficiency. It is worth noting that, for the determination of the Brillouin gain coefficient using the CRDM method, the laser is operating below 61.8 mW.

An optical spectrum of the non-resonant Brillouin laser, which is obtained with a high resolution Brillouin optical spectrum analyzer (BOSA), is shown in figure (3.4a). The Stokes component is, offseted by 10.87 GHz from the pump wavelength, which corresponds to the Brillouin frequency shift.

To observe the mode-hopping, we used a high-resolution Fabry-Perot spectrum analyzer because the resolution of the BOSA is limited to 10 MHz, which is in the order of the FSR.

3.4.2 Experimental observation of mode-hopping

Mode-hopping is observed using a high-resolution Fabry-Perot spectrum analyzer with a 2 MHz resolution and 300 MHz FSR. This optical analyzer consists in varying the length separating the two mirrors, over a half-wavelength (half a wavelength corresponds to an FSR), by moving one mirror thanks to a PZT. This change in length of the cavity is so small that it does not affect the FSR of the Fabry-Perot. However, it makes all comb resonant-frequencies shifting along with length variation of the fiber ring cavity. The detected signal on the photodetector and the triangular PZT scanning amplitude

are displayed on an oscilloscope showing the Airy function. By using the known length separating the two mirrors, the free spectral range is determined and is used to calibrate the horizontal axis of the oscilloscope. Stokes signal is measured and reported in figure

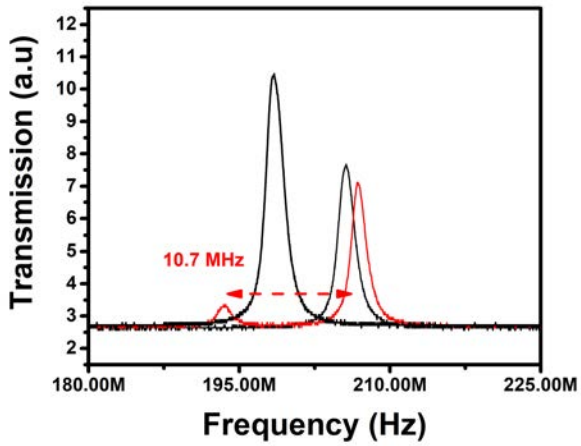

Figure 3.5: Mode-hopping of non-resonant Brillouin laser cavity, observed through a Fabry-Perot analyzer in different time intervals (black signal). Red signal shows that we can observe two resonant modes at the same time under the gain bandwidth.

(3.5) using the scanned Fabry-Perot analyser. The figure shows different acquisitions; each time, the resonant mode is suffering a frequency shift. Sometimes two-mode are co-existing under the gain cure simultaneously as shown in red color. In this case, the mode are separated by 10.7 $\pm$ 2.0 MHz, which is near to the calculated FSR of the 20 m Brillouin cavity (10 MHz). These observations demonstrate the necessity for an active locking of the resonance frequency by controlling the cavity length or the pump wavelength. The next section describes mode-hopping suppression technique based on cavity-length and pump frequency control.

3.5 Stabilized non-resonant Brillouin fiber laser

In this section, we propose a new frequency stabilized mode-hopping suppression method, which improves the frequency noise of the non-resonant Brillouin laser. As seen in section (3.2), the mode-hopping generally observed is due to the shift of the resonant mode, which resonates at the maximum of the gain bandwidth. To suppress this effect we need to stabilize the wavelength of the resonant mode with respect to the gain maximum or the inverse. In 2016, a mode-hopping suppression method on the non-resonant Brillouin cavity was reported [170]. Their approach is based on the phase-locked-loop (PLL), which

freezes the frequency difference between the pump and the Stokes waves. When the length of the Brillouin fiber resonator changes due to thermal and acoustic fluctuations, its resonance frequency drifts relatively to the maximum of the SBS gain. Therefore, the active laser mode, which provides maximum gain, transfers successively from one mode to another.

Measurement of the beating between the Stokes and the pump frequencies includes the detuning between the maximum SBS gain and the resonant frequency associated with the oscillating Stokes wave. Moreover, by freezing the frequency difference between the Stokes and pump, one could automatically stabilize the Stokes oscillating wave with respect to the maximum SBS gain. Effectively, the SBS maximum gain frequency follows the pump frequency. So pump frequency is drifting according to the cavity length drift. It suppresses the mode hopping effect. The locking stability depends on the local oscillator which is used as a reference.

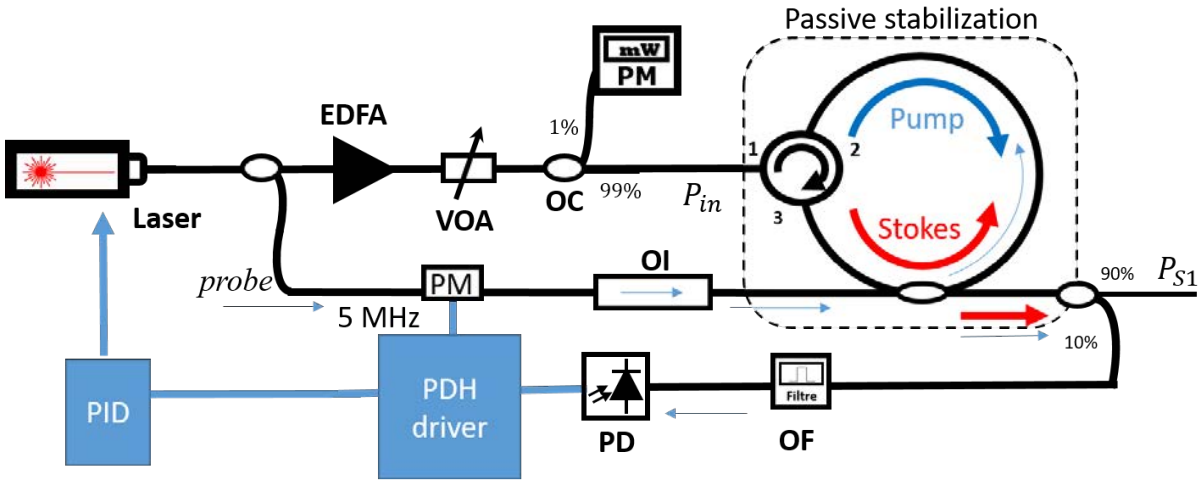

Figure 3.6: Experimental setup of BFL cavity with active PDH locking on cavity a resonances. EDFA: Erbium-doped fiber amplifier, VOA: Variable optical attenuator, OC: Optical coupler, PD: Photodetector, PM: Phase modulator, OI: Optical isolator, OF: Optical filter.

We propose a frequency stabilizing method using PDH locking. It is commonly used in resonant Brillouin laser. From our knowledge, it has not been used for non-resonant pumping scheme. The PDH locking method is described in section (1.5.2). In a non-resonant pump scheme, the pump cannot have a resonant mode. We then use a weak reference pump signal called probe, propagating in the same direction than the Stokes. Probe signal is used to lock the pump frequency to a cavity resonance-frequency as shown

in figure (3.6) using the PDH method.

The non-resonant BFL cavity consists of an optical circulator and an optical coupler. The circulator permits a resonant propagation in the backward direction. The laser power is splitted into two arms, using a coupler. In one arm, the signal is launched into a fiber ring resonator via an optical circulator through an EDFA, and a VOA, in order to generate the Stokes wave. In the signal arm, probe is launched in the same ring cavity but in the backward direction. This probe signal is phase-modulated at 5 MHz to realize a PDH frequency locking mechanism, which maintained the probe in a resonant mode. The benefit of this PDH locking technique is to transfer the stability of the ring cavity to the pump laser. This reduces the drifting (flicker noise) of the pump frequency. Since we can reasonably consider that the Brillouin shift is constant, the generated backward-propagating Stokes in the first arm will be stabilized on a frequency ν_{s1}.

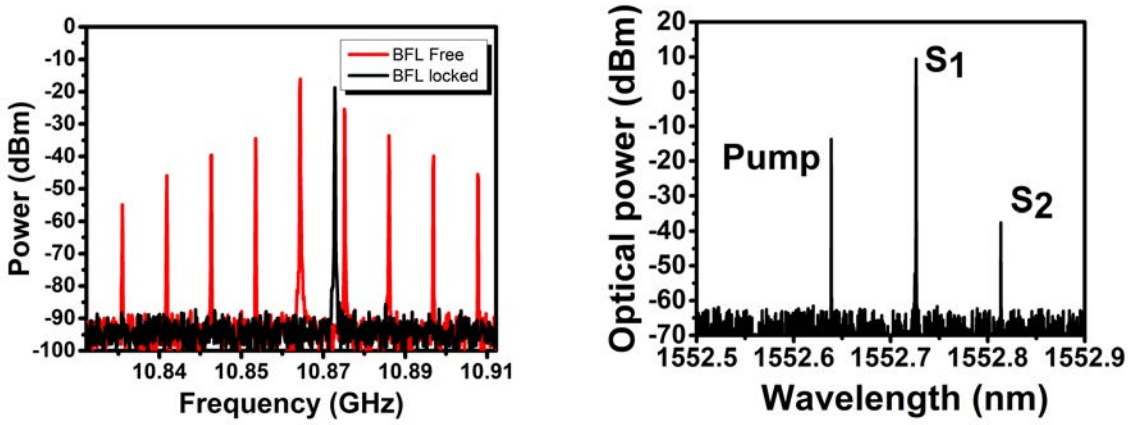

(a) (b)

Figure 3.7: (a) Beating between pump and Stokes wave with and without mode-hopping stabilization scheme. (b) Optical spectrum of stabilized non-resonant BFL cavity.

For the PDH locking the signal is modulated at a frequency of 5 MHz using a phase modulator. The modulated optical signal is injected into the ring cavity through the coupler. The optical power in the second arm is kept small ($< 1mW$) to have negligible unwanted nonlinear interactions. The output port contains the Stokes signal and the probe signal. A small portion of the output signal is extracted using a 90/10 coupler and is filtered out, using an optical filter to extract the probe signal. The Stokes signal is filtered out from the other port. The PDH probe is demodulated using the PDH driver (from TOPTICA photonics). It generates the error signal that is fed to the control loop that modifies the pump frequency [75, 76]. We can check the disappearance of mode-

hopping using the oscilloscope, as well as the long-term stabilization (more than 1hr). Figure (3.7a), shows the beating signal between pump and Stokes waves in free running (red) with multiple beating due to the mode-hopping phenomena. The black line shows a single frequency beating signal after locking. Moreover, the optical spectrum is measured using the BOSA and is shown in figure (3.7b). For high pump power (202 mW), we observe a Stokes 1 (S1) and Stokes 2 (S2) signals. Signal to noise ratio between Stokes 1 and 2 is 50 dB because the Stokes 2 is not resonant in the cavity. We obtained 0.63 mW output power of Stokes 2 at 300 mW input pump power. The observation of stable Stokes 2 emission is an indirect means to evaluate the stability of the frequency locking scheme.

3.6 Frequency noise of non-resonant Brillouin laser

In a conventional laser, light amplification is obtained by population inversion of atoms or molecules. The spontaneous emission associated with the gain medium acts as a quantum noise source responsible for the presence of a minimum spectral width given by the limit of Schawlow-Townes [56]. In semiconductor laser, this limit is a few kHz and can even reach the values of Hertz for gas lasers. This limit is difficult to measure because of the technical noise due to temperature and mechanical vibrations caused by environmental disturbances. The spontaneous emission is not the only source of noise in a conventional laser. The noise of the laser emission also depends on the fluctuations of the pumping system. The intensity noise of a conventional laser is strongly, linked to the intensity noise of the pump laser noise. In the case of optically pumped conventional lasers, the frequency noise of the pump does not contribute to the laser frequency noise.

However, in the case of a Brillouin laser, it is not always true because there is a strong coupling between the phase of the emitted Stokes wave and that of the pump wave. Indeed, in a Brillouin process, there is an interaction between three waves via electrostriction. The pump wave interacts with an acoustic wave in order to generate a Stokes wave, (see chapter 2 for details). Then intensity and phase noises of these waves are coupled together.

In the following, we will describe the frequency noise of non-resonant Brillouin laser. We will introduce an analytical model for the frequency noise. Then we compared the analytical and experimental result in different non-resonant Brillouin fiber laser configu-

rations.

3.6.1 Analytical frequency noise of non-resonant BFL

Linewidth narrowing of Brillouin laser was experimentally observed by Smith [25] and theoretically studied by Debut [123] within the framework of a three-wave model. It was shown that the phase noise of the Stokes wave is strongly reduced and smoothed under the combined actions of acoustic damping and cavity feedback [124]. The phase noise transfer of the Brillouin laser can be found in [123]:

$$S_0(f) = \frac{-lnR}{\beta_A - lnR + i2\pi f} \frac{e^{i\pi f} sin\pi f}{\pi f} \phi_0(f), \tag{3.3}$$

$$H_1(f) = \frac{-ln(R)}{\beta_A - ln(R) + i2\pi f} \tag{3.4a}$$

$$H_2(f) = \frac{e^{i\pi f} sin\pi f}{\pi f}, \tag{3.4b}$$

$S_0(f)$ and $\phi_0(f)$ are respectively, Stokes and pump phase noises. Eq (3.3) can be factorized into two contributions: H_1 and H_2. R is the feedback rate of the cavity, which is defines as $R = \alpha_2 \times (1 - |\kappa|^2)$. β_A is the acoustic damping rate: $\beta_A = 2\pi\Delta\nu_B/\Delta\nu_{FSR}$. The transfer function of the Stokes phase noise is shown in figure (3.8). The graph is plotted

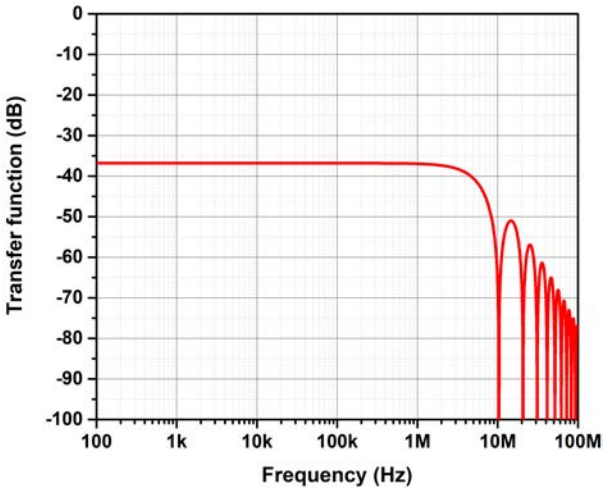

Figure 3.8: Analytical phase noise transfer function for the 20 m fiber length cavity with R = 0.78 and $\beta_A = 17.27$.

by taking the value of the fiber length, the Brillouin gain bandwidth and the feedback rate of 20 meters, 27.5 MHz, and 78 % respectively. This transfer function is thus associated with two factors: H_1 acts like a low pass filter, which filters out the fluctuations

at high frequencies; it also reduces the amplitude fluctuations at low frequencies as its modulus is less than 0 dB. H_1 is related to cavity parameters, to the acoustic damping rate, and to the coupling ratio. H_2 corresponds to the delay line filtering effect of the inteferometer (fiber spool ring cavity). The phase noise reduction between the pump and Stokes is called the K factor and is expressed as :

$$K = \left(1 - \frac{\beta_A}{ln(R)}\right)^2 \tag{3.5}$$

As cavity losses and gain bandwidth are taken into account (table (3.2)), frequency noise reduction of 37 ± 1 dB with such a Brillouin laser is expected. A similar frequency noise reduction effect was reported in [33] and [34]. The reduction factor may vary with the feedback rate R.

In Brillouin laser, there are three main sources of noise. The first is the noise from the pump laser; this noise will be filtered out before being transferred to the Stokes wave as mentioned in the former subsection. To get a low-noise Brillouin laser, the ideal configuration would be to use a low-noise pump laser. The second source is related to the cavity; it is mainly a variation of cavity length and reinjection rate due to thermal and mechanical fluctuations. If the laser cavity is sufficiently stable, then the fluctuations of fiber length are small, which induces only "slow" drift of the laser frequency, typically in the frequency band (DC-1 kHz). On the other hand, they do not contribute to the intrinsic linewidth of the Stokes wave. The third source is related to the spontaneous Brillouin scattering. By analogy with conventional lasers, for which spontaneous emission limits the Schawlow-Townes linewidth, similarly spontaneous Brillouin scattering limits the Stokes-wave coherence. The noise level is generally very low when compared to the other noise contributions.

In the following, we study the frequency noise of the non-resonant Brillouin laser in three different configurations. The first one consider a free running laser to pump the non-resonant BFL cavity. In the second case, a stabilized pump laser is used and then, in the third configuration we study a laser architecture based on the cascading of two non-resonant BFL. We conclude by a comparison of the frequency noise reduction performances. We measure the frequency noise via a self-heterodyne technique thanks to a Mach-Zehnder interferometer with a 200 meter delay, which was introduced in section (1.4.3).

3.6.2 Non-resonant BLF frequency noise using a free running pump laser

Tunics OM laser is used as a pump laser for this experiment. Measured frequency noise of Stokes and pump laser are plotted on figure (3.9a) (in black for the pump and blue for S_1). As we have seen before the BFL frequency noise is reduced by a factor of K due to the combined influences of the cavity feedback and acoustic damping rate. In order to compare the experimental results, we analytically calculated the frequency noise by the product of the pump frequency noise and the analytical transfer function of the BFL (dotted blue line). A good match is found between measured and the calculated frequency noise. A reduction of 37 dB relatively to the pump frequency noise over a frequency range comprise between 1 kHz and 300 kHz is observed. Below 1 kHz, we remark a discrepancy between the measurement and the simulation. Indeed, the amplitude of the measured frequency noise is slightly larger because measurements are limited by noise floor. In figure (3.9), dotted gray line shows the noise floor of MZI with 200 m fiber (see section (1.4.4b). Below 8 kHz, noise measurements are limited by the noise floor of our experimental bench. This is due to the stability of our MZI. Note that a better stabilization of the interferometer could improve the noise floor [171]. Above 100 kHz, the noise floor is nearly 24 dB down from the frequency noise of Stokes.

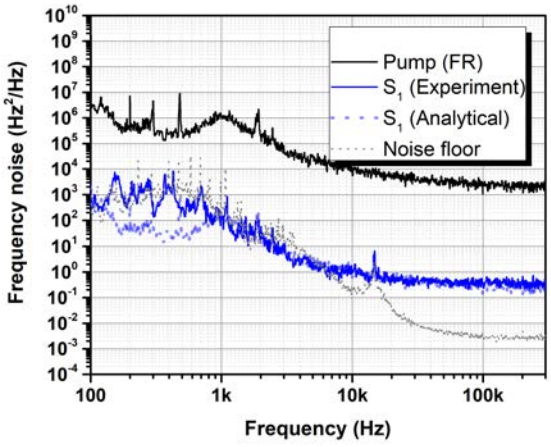

Figure 3.9: Experimental and analytical frequency noise measurement of 20 m non-resonant BFL. Corresponding noise floor with 200 m delay is plotted in dotted line.

We estimate the integrated linewidth of the pump laser and of the Stokes line using the "$\beta - line$" approximation. In the free-running (FR) operation, the pump laser exhibits an integrated linewidth of $187 \pm 18\ kHz$ for 10 ms observation time. The frequency noise

level is $3 \times 10^6\ Hz^2/Hz$ at 100 Hz offset frequency. From the estimated frequency noise reduction previously calculated, we may expect to observe an integrated linewidth of 360 Hz (see blue dotted line in figure (3.9)). Taking into account the noise floor, that gives frequency noise level of $5 \times 10^2\ Hz^2/Hz$ at 100 Hz offset frequency, enables us to say that the integrated linewidth is below 2 kHz and that we cannot know its exact value. Thus it has decreased the integrated linewidth from $187 \pm 18\ kHz$ to a value below 2 kHz. If we assume that it is correct to draw a comparison between the analytical results and the noise floor, the noise floor has to be improved by 20 dB in order to measure the low frequency component (and the following case shown in figure (3.10a) by 40 dB).

3.6.3 Non-resonant BFL frequency noise using stabilized pump laser

To suppress mode-hopping, we stabilize the pump frequency onto a cavity-resonance frequency. Figure (3.10) shows the frequency noise measured for the free running pump laser, frequency-locked (FL) pump, and the SBS laser. By locking the pump laser onto a cavity resonance, the integrated linewidth of the pump laser is improved, when comparing the black curve and red curve of figure (3.10). Once again the improvement below 8 kHz cannot be characterized because the PSD reaches the noise floor. We can only say that the integrated linewidth is lower than $66.17 \pm 6\ kHz$ kHz. The improvement of the pump noise level is at least the one of the noise floor, which is decreased at least by three order of magnitude compared to frequency noise of free-running pump.

As we have seen previously, SBS laser will improve the reduction of the laser linewidth due to the improvement of pump flicker noise. Expected frequency noise are plotted in lightgreen colour. Unfortunately, S_1 (FL) is limited by noise floor of our bench. So we do not see any improvement in the S_1 frequency noise between FR and FL. Still, the intrinsic linewidth is reduced from 6.8 kHz to 1.3 Hz, which corresponds to 37 dB reduction. It matches our estimated value of 37 ± 1 dB.

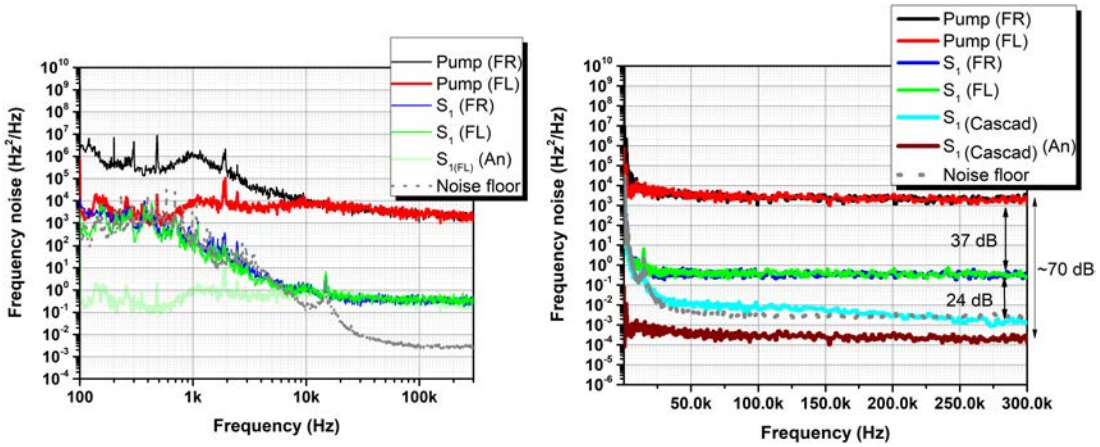

(a) (b)

Figure 3.10: Frequency noise of the non-resonant BFL laser. (a) pump and Stokes signal with and without stabilization in logarithmic scale (b) frequency noise of cascaded non-resonant BFL laser in linear scale.

3.6.4 Frequency noise performances of two cascaded non-resonant BFL

To find the intrinsic linewidth limitations, we cascaded two non-resonant BFL, frequency noise is plotted in figure (3.10b). A first Stokes wave is generated with a 20 meters fiber cavity, which gives 37 dB noise reduction. Then the output of this BFL is amplified using an EDFA and injected into a second BFL. The second Brillouin laser is made by a 14 meter fiber cavity and 75 % of rejection rate, which corresponds to a noise reduction factor of 33 dB. Then a reduction factor close to 70 dB might be expected when compared to the pump laser frequency noise.

We plot on figure (3.10b) the expected noise reduction (dotted brown curve) and the measured Stokes frequency noise at the output of the two cascaded Brillouin laser (cyan curve). We obtained 61 dB reduction in frequency noise. This performance is limited by the noise floor of our MZI (dotted gray curve) that do not allows to completely characterized this configuration. The cascaded BFL reaches the intrinsic linewidth of 47 mHz at 100 kHz.

We have shown that cascaded Brillouin laser architecture laser can reach the sub-Hz intrinsic linewidth. However we did not succeed to explore the limitation of this Brillouin laser configuration.

3.7 Conclusion

Non-resonant Brillouin laser is demonstrated using a silica fiber cavity. We explained the threshold power and mode-hopping characterization of a Brillouin ring-cavity. 20 meters Brillouin cavity is made using a silica fiber and it is experimentally shown that even a short cavity could suffer from mode-hopping due to the thermal shift of the cavity resonances. We then proposed a frequency stabilized non-resonant Brillouin laser design, which suppressed the mode-hopping effect. Also, it improved the pump laser noise by transferring the stability of the cavity to the pump using the PDH method. Finally, the frequency noise properties of a non-resonant Brillouin fiber laser have been investigated experimentally with the realization of Hz level Brillouin laser. Moreover, we demonstrated that a mHz linewidth laser based on cascading of two BFL cavities can be easily reached.

Chapter 4

Multi-Stokes Brillouin fiber laser

4.1 Introduction

We have seen that stimulated Brillouin scattering can be used as a laser gain medium and that non-resonant Brillouin laser can exhibit a sub-Hz linewidth. The high laser threshold of the non-resonant Brillouin laser can be a limiting factor in some applications. Another class of high performances lasers are resonant Brillouin lasers, in which pump and Stokes waves are resonant inside the cavity. Resonant Brillouin laser acquire a lot of interest in laser physic communities for its ability to exhibit low threshold and low noise dynamics [25, 123]. Resonant Brillouin laser is capable to produce different lasing Stokes orders. Power dynamics, linewidth narrowing and intensity noise reduction have been demonstrated in various systems as fiber rings [34, 126], whispering gallery mode microresonators [158] or planar waveguide structures [172] to only name a few. Those systems are made of nonlinear materials as silica [34], chalcogenide [33], silicon nitride [163], crystal fluoride [145] or silicon [173].

One remaining question concerning the resonant Brillouin laser architecture is the potential to improve the intensity and frequency noise reduction by cascading the SBS process. Theoretical papers related to this problematic predicts intensity and frequency noise dynamics in the cascaded SBS process [3]. In this chapter, we demonstrate experimentally, that under a specific operating regime, Stokes line intensity noise can be reduced up to 20 dB with respect to the input pump RIN. Moreover we report the complex RIN dynamics of a multi-Stokes Brillouin laser (MBL) in various configurations. Those results have been published in "Optics Express" in December 2018 [174]. Similarly, we investigate

the frequency noise dynamics of the multi-Stokes Brillouin laser. We observe a close to 27 dB of frequency noise reduction for single mode Brillouin laser compare to it's pump noise. In particular, we investigate the roles of the photon lifetime and detuning of the gain bandwidth on the RIN and frequency noise reduction of the MBL.

The chapter is organized as follows. In section (4.2), we describe the physics of the MBL. In section (4.3), the experimental setup and the fiber ring resonator used for the present study are explained. We introduce the MBL model based on coupled mode equations and derive the stationary response of MBL, which are explained in sections (4.4) and (4.5) respectively. In section (4.6), we study the RIN behavior of Stokes lines in function of the input pump power in presence of higher order Stokes lines. Moreover, we discuss the impact on RIN performances of several parameters as cavity lifetimes, detuning of gain bandwidth and pump noise level.

In order to study the influence of detuning and length, we setup a short cavity with high-Q factor, which enables the detuning to be controlled by pump wavelength. In section (4.7), we introduce the frequency noise study of the MBL. First, we describe the frequency noise behavior of the Stokes lines as a function of the input pump power. Secondly, we explain the over all frequency noise behavior of individual Stokes lines and the impact of the cascaded and gain detuning effects. Finally, we study the impact of photon lifetime of the cavity on frequency noise of the Stokes 1 ($S1$) laser emission.

4.2 Resonant Brillouin laser

In resonant Brillouin laser configuration, pump and Stokes waves are resonant inside the cavity. The critical physics behind the Brillouin laser is the coupling between optical and acoustic waves. As we have seen in chapter 2, through Brillouin scattering process, a high-frequency photon (Pump) characterized by its frequency ω_0 and wavevector k_0, decays to a lower frequency photon (Stokes) and phonon with frequencies ω_1 and Ω_0 and wavevectors k_1, q_0, respectively. Brillouin coupling efficiency transfers the energy from the pump to the Stokes waves. Stokes photons can stimulate as well the decay of pump photons to Stokes photons generation, similarly to a classical gain media through stimulated optical amplification. This amplification occurs in a small bandwidth $\Delta\nu_B$, which is related to the phonon decay rate in the medium. When the medium is placed inside a cavity, the process will be more efficient if the pump is coupled to an optical resonant mode. The

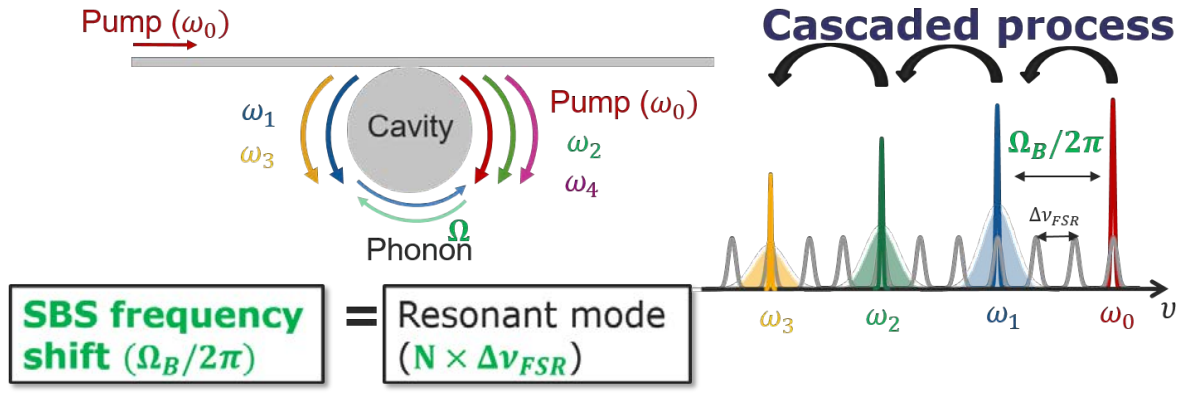

Figure 4.1: Illustration of cascade Brillouin laser. A pump laser of frequency ω_0 is injected into an optical resonator. When its wavelength matches the Brillouin condition ($(\Omega_B/2\pi) = N \times \Delta\nu_{FSR}$), pump resonant mode at ω_0 is scattered at ω_1 by emitting a phonon at Ω_B. When the pump power is sufficiently high, the Stokes wave at ω_1 acts as a pump for higher order Stokes lines.

Stokes signal is generated at a frequency related to one of the resonant modes. If the Stokes frequency is at the maximum gain frequency, then the Brillouin frequency shift is a multiple of the free spectral range ($(\Omega_B/2\pi) = N \times \Delta\nu_{FSR}$) as shown in figure (4.1). Then the Stokes wave generation is more efficient. At higher pumping power, counter-propagating Stokes 1 ($S1$) acts as a pump for a counter-propagating second Stokes 2 ($S2$). This process is generated by a distinct phonons reservoir with frequency Ω_1 and is propagating in the opposite direction to phonons at frequency Ω_0. Frequency differences between the consecutive Stokes are not equal and are slightly shifted because each Stokes wave is created with different phonons frequencies [34]. The shift is moreover dependent of the pump wavelength and temperature as we have seen in section (3.2).

The optical pump is thus injected into a high-Q cavity. As underlined before, the Brillouin gain, created by the pump wave circulating several times in the cavity, allows a Stokes wave flowing in the opposite direction to reach the laser threshold. We consider that the pump frequency and cavity resonance frequency are stable. Resonant Stokes 1 (S1), located at the maximum of the Brillouin gain, can then be amplified. It propagates in the opposite direction to that of the pump. Similarly, when the power in S1 reaches the output power needed for Stokes 2 (S2), to compensate its linear losses, coherent emission of S2 wave also takes place; the cascaded process is on.

4.3 Brillouin laser architecture

We have seen that different types of Brillouin laser architectures have been studied in the last few years. In this thesis, we study two kind of Brillouin laser, resonant and non-resonant configuration. In the previous chapter, we have discussed and studied the dynamics of the non-resonant Brillouin laser. In this section, we examine the resonant Brillouin laser dynamics, which is interesting due to the low threshold and higher order Stokes emissions. We are focusing on the fiber ring cavity based Brillouin laser. This section is organized in three parts. Firstly, we will explain the fiber ring cavity and its parameters, which are essential part of the Brillouin laser. Secondly, we will describe the experimental setup of the laser. Finally, we will detail the laser locking method used to maintain the pump laser in resonance with the fiber ring cavity.

4.3.1 Fiber Ring Cavity

The central element of the MBL is composed of a fiber ring resonator. As we have seen in previous chapters, the gain or losses inside the resonator is quantified by the intrinsic cavity lifetime ($\tau_0/2$) and the coupling strength by the coupling lifetime ($\tau_e/2$). Moreover, the resulting total photon lifetime of the resonator can be linked to the Q-factor (see section (2.4.1)).

The resonator is made of a 20 meters polarization-maintaining fiber corresponding to a free-spectral range (FSR) of 10 MHz. The light is coupled in and out through a variable coupler allowing to vary the coupling coefficient and then the Q-factor of the resonator [97]. In the present study, we consider two resonator configurations for study the impact of photon lifetime in Brillouin lasers, which we call: the high-Q resonator ($Q_{\mathrm{h}} = 6 \times 10^8$) and the low-Q resonator ($Q_{\mathrm{l}} = 2 \times 10^8$). Table (4.1) shows the extracted cavity parameters using the cavity ring down method, which was introduced in section (2.4). The low-Q factor (MBL_{LQ}) and high-Q factor (MBL_{HQ}) cavities are in the overcoupling regime ($\tau_0 > \tau_{\mathrm{el}}$) and the undercoupling regime ($\tau_0 < \tau_{\mathrm{eh}}$) respectively.

In terms of Brillouin laser performances, the overcoupling regime implies a higher output power at the price of higher lasing threshold with respect to the undercoupling operation. As it will be shown later, the Q-factor of the resonator impacts the RIN features of the MBL (Section 4.6).

Table 4.1: Parameters of resonant BFL 20m cavity

Parameters	MBL_{HQ}	MBL_{LQ}
τ_0	1.39 μs	1.39 μs
τ_e	3.7 μs	0.47 μs
$Q-factor$	6×10^8	2×10^8

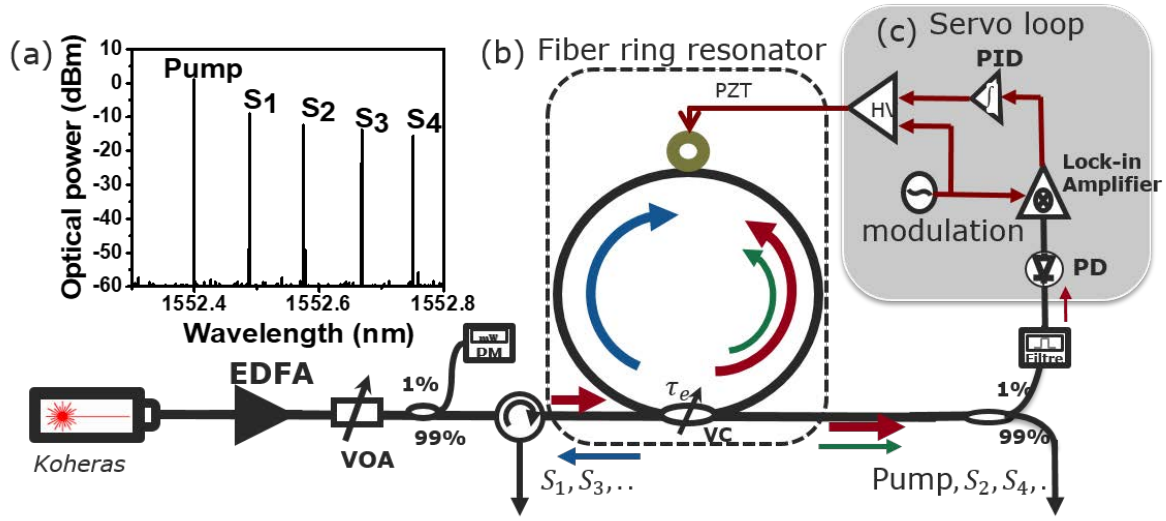

Figure 4.2: Experimental setup to study the lasing properties of multi-Stokes Brillouin Laser. Pump: Koheras continous wave laser, EDFA: Erbium-doped fiber amplifer, VOA-variable optical attenuator , VC: Variable coupler, PZT: Piezoelectric transducer, Filter: Yenista optical filter, PD: Photodetector, PID: Proportional-integral differential amplifier, HV: High-voltage amplifer, TA: Transimpedance Amplifier, ESA : Electrical spetrum analyzer. 20 m polarization maintaining fiber spooled in PZT. Red line: Pump wave, Blue: Stokes 1 wave , Green: Stokes 2 wave.

4.3.2 Experimental setup

The experimental setup is illustrated in figure (4.2). The fiber ring cavity is optically pumped using a continuous wave (CW), that has an integrated linewidth of 2 kHz with observation time 10 ms at 1552.4 nm. The laser output power is amplified before the cavity injection. A motorized variable optical attenuator helps to control the input power in the MBL. 1 % of the input pump power is collected for power monitoring.

The laser pump signal is injected in the cavity via a circulator and a coupler, and then propagates clockwise around the cavity (red arrow). The circulating pump wave initiates Brillouin amplification in S1 wave, traveling in the opposite direction (blue arrow). For

sufficiently high pump power ($P_{\text{in}} = P_{\text{th}}$), Brillouin lasing threshold is reached giving rise to efficient S1 emission outside the resonator. S1 wave can, itself, play the role of pump laser for S2 wave (green arrow).

4.3.3 Cavity servoing

The laser threshold for the various Stokes waves can be drastically reduced when the pump signal is resonantly coupled to the cavity. This configuration can be achieved by locking a cavity resonance to the CW pump laser. We implement a derivative spectroscopy stabilization method [175]; its setup is presented in gray box in figure (4.2c). Locking technique was explained in section (1.5.1). The actuator consists in a piezoelectric (PZT) ceramic cylinder wrapped by few meters of fiber. Varying the voltage on the piezoelectric cell implies a modification of the cavity length and then a control of the frequency position of the cavity resonances. We apply a slow modulation of 10 kHz on the PZT through a high-voltage amplifier, which creates a derivative error signal from the lock-in amplifier. Actuator signal is produced by sending the error signal to a PID controller. Using this technique, the cavity is maintained in resonance with the pump laser during MBL operation.

As can be seen in figure (4.2a), from the observation at the Brillouin optical spectrum analyzer (BOSA), a multi-Stokes spectrum contains higher-order Stokes waves when the pump power injected approaches 200 mW in a MBL_{HQ} cavity. The first-order Brillouin offset is about 10.87 GHz. In conclusion, we introduce the Brillouin laser architecture and cavity parameters, which will be used for the analysis of the power and RIN dynamics of the laser. In the next section, we will introduce the theoretical model for the analysis of resonant Brillouin laser dynamics.

4.4 Theoretical model

Cascaded Brillouin models are reported in the literature [3, 33, 34, 116]. To study the dynamics of the cascade Brillouin process, we used the coupled-mode formalism to describe the SBS interaction between the pump, Stokes and density waves for a ring resonator. W. Loh *et al.* [4] described single Stokes generation of Brillouin laser model with the help of a three wave equations. Irina Balakireva (post-doc in our lab) extended the model

into a multi-Stokes Brillouin laser (MBL) configuration [174]. The model, based on the coupled modes formalism [176], depicts the temporal dynamics of $2N+1$ coupled-mode equations where N is the maximum number of Stokes waves under consideration:

$$\frac{\partial A_0}{\partial t} = -\frac{1}{\tau}A_0 - iq_0\omega_0 A_1\rho_1 + \sqrt{\frac{2}{\tau_e}}Se^{i\sigma_0 t}, \tag{4.1}$$

$$\frac{\partial A_\eta}{\partial t} = -\frac{1}{\tau_\eta}A_\eta - iq_\eta\omega_\eta\left[A_{\eta-1}\rho_\eta^* + \delta_{\eta\neq N}A_{\eta+1}\rho_{\eta+1}\right], \tag{4.2}$$

$$\frac{\partial \rho_\eta}{\partial t} = i\frac{\Omega_B^2-\Omega_\eta^2}{2\Omega_\eta}\rho_\eta - \frac{\Gamma_B}{2}\rho_\eta - ip_\eta A_{\eta-1}A_\eta^*. \tag{4.3}$$

Here A_η, ω_η, and τ_η are called the amplitude, frequency and the lifetime of the generated Stokes wave label η (with $\eta \in [1,N]$). $|A_\eta|^2$ is proportional to an energy. Eq. (4.1) describes the dynamics of the pumped mode A_0, with an angular frequency emitting in the C band fixed to $\omega_0 = 1.22\times10^{15}$ rad/s. ρ_η and Ω_η are the amplitude and frequency of the density wave labeled η. Γ_B and Ω_B are the angular loss rate and frequency related to Brillouin gain bandwidth and frequency shift described before. These two parameters are experimentally extracted (see section 2.3.1). For sake of simplicity, we will consider a constant Brillouin Stokes shift over the cascaded process, which means, $\Omega_\eta = \Omega_B$, then the $\omega_\eta = \omega_{\eta-1} + \Omega_B$ for all η. Coefficients q_η and p_η are:

$$q_\eta = \frac{\gamma_e}{4n_0^2\rho_0}\Lambda_\eta, \quad \text{and} \quad p_\eta = \frac{\epsilon_0\gamma_e n_0^2\Omega_\eta}{4v^2}\Lambda_{\rho_\eta}, \tag{4.4}$$

where $\gamma_e = 1.5$ is the electrostrictive constant, ϵ_0 is the vacuum permittivity, n_0 is the refractive index for silica, ρ_0 is the equilibrium density of the material, v is the velocity of the acoustic wave.

In the present work, the resonator is composed of fibers. We can reasonably consider that modes are similarly confined in the fiber and we can then fix the value of mode overlaps Λ_η and Λ_{ρ_η} to 1. From this assumption, equations (4.4) will be simplified as q_η is constant and equal to q for all waves as it is for $p_\eta = p$ as we assume an equal Brillouin shift for all orders. The amplitude of the pump wave is $S = \sqrt{P_{in}/(V_{ph}\epsilon_0)}$ (W/m^2) , where P_{in} is the power of the laser (in Watts) and $V_{ph} = 1.56\times10^{-9}$ m^3 is the optical mode volume of the fiber ring cavity. P_S is the optical power for the Stokes. We will introduce in the following P_C as the clamping power.

As we have seen in chapter 2 (section 2.4), the total lifetime τ_η of each Stokes waves can be found by $1/\tau_\eta = 1/\tau_{0\eta} + 1/\tau_{e\eta}$ where $\tau_{0\eta}$ is the intrinsic lifetime (cavity losses) and $\tau_{e\eta}$ is the coupling lifetime. We consider the lifetimes equal for all waves, and we

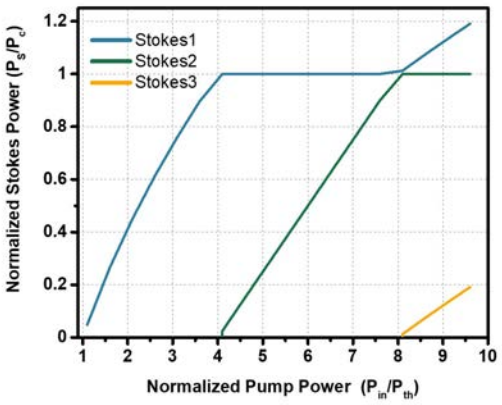

Figure 4.3: Steady-state laser powers for the Stokes components, obtained from the simulation.

write $\tau_\eta = \tau$, $\tau_{0\eta} = \tau_0$, $\tau_{e\eta} = \tau_e$. These last equations have to be linked to the former assumption concerning the confinement. As far as we consider similar confinement, p and q are the same for all waves.

The stationary response can be found by setting all derivatives in Eqs.(4.2) & (4.3) to zero and by finding the joint solutions of the equations. The stationary solutions can be found for any N using three equations. Two of them do not depend on the parity of N:

$$|A_{N-1}|^2 = \frac{K_N}{\omega_N}, \tag{4.5}$$

$$|A_{\eta+2}|^2 = |A_\eta|^2 - \frac{K_{\eta+1}}{\omega_{\eta+1}}. \tag{4.6}$$

Another one is changing following the parity of maximum Stokes order N:

$$|A_0|^2 = \frac{2\tau^2}{\tau_e}|S|^2 \times \left[K^{-1}\omega_0|A_1|^2 + 1\right]^{-2}, \text{ if } N = 2,4,6... \tag{4.7}$$

$$|A_1|^2 = \left[\frac{\tau}{\sqrt{\tau_e/2}}\frac{|S|}{|A_0|} - 1\right]\frac{K}{\omega_0}, \qquad \text{if } N = 1,3,5... \tag{4.8}$$

here K_η equals to $\Gamma_B/(2\tau p_\eta q)$. The technique to calculate the amplitude of the laser emission is the following. First, we calculate $|A_{N-1}|^2$ using Eq. (4.5), and after using Eq. (4.6) we find $|A_{N-3}|^2, |A_{N-5}|^2$ etc. until A_0 if N is odd or A_1 if N is even. After we use Eqs. 4.7 or 4.8 and finish the calculations of missing lines amplitude by Eq. (4.6) until $|A_N|^2$.

We plot in figure (4.3), the evolution of various Stokes order versus a S1-threshold-normalized input pump power. For a normalized pump power $P_{pump} = P_{in}/P_{th}$ lower

than 1, the transmitted pump power evolved linearly. At $P_{pump} = 1$, the transmitted pump is clamped. This operating point corresponds to the onset of coherency in the first Stokes order. Indeed, the Brillouin gain, induced by the pump, balances the linear losses experience by the mode A_1. An efficient stimulated Brillouin emission occurs (blue line). When the power in S1 reaches the normalized output power needed to compensate linear losses of S2, coherent emission also takes place for S2 (green line), then the cascaded process is activated.

The cascaded generation of multiple Stokes waves has been treated analytically by Toyama *et al.* [116] considering resonant pumping of the cavity and constant Brillouin gain for all Stokes orders. The model gives rise to similar results than previously reported models in the literature [3, 116]. We will see in the following that this analytical model gives good matches with the experimental results.

4.5 Power characterization of multi-Stokes Brillouin fiber laser

This section is dedicated to the experimental analysis of the power dynamics of the MBL and its comparison with analytical results presented in the above section. In Fresnel's thesis [34], the power characterization of 4 Stokes orders and a study of the efficiency and threshold have been reported. A similar power dynamics is reported in microsonator [147] and integrated ring Brillouin laser [163]. These recent studies give quantitative picture of the power dynamics of the Brillouin laser. In this section, we explicitly detail power dynamics of the MBL as it is of fundamental importance for MBL noise analysis, which are closely interconnected. Moreover, we will compare experimental and theoretical results. Also we will present the influence of the photon lifetime on the threshold and output power of Stokes signals.

The experimental setup of MBL has been detailed in section (4.3); for power characterization study, we locked pump-laser frequency on MBL_{LQ} cavity by a top-of-fringe method. The pump power is varied from zero to 200 mW, Stokes signal is filtered and measured using a power meter. The evolution of output Stokes lines 1, 2, and 3 as a function of the input pump power is given for the low-Q factor cavity in figure (4.4a). We obtain 26.5 mW of threshold for S1 signal. The S1 signal linearly increases above this

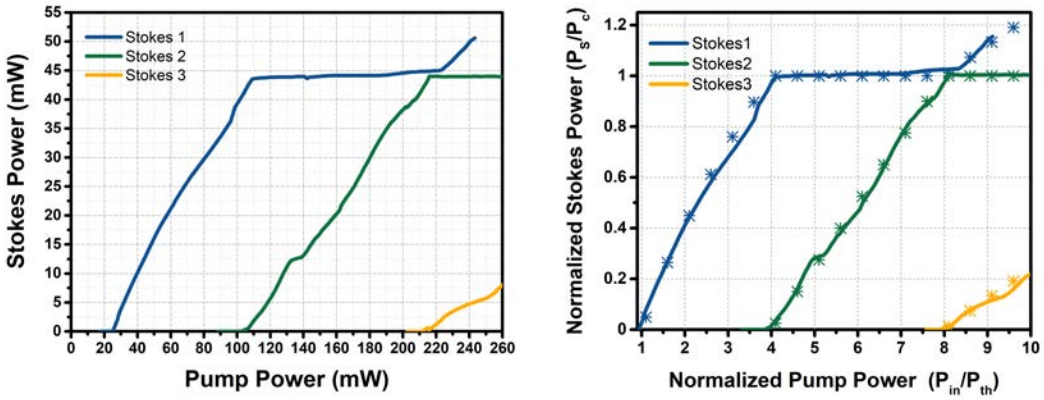

(a) (b)

Figure 4.4: (a) Power characterization of MBL_{LQ} cavity (b) Normalized Power characterization of MBL_{LQ} cavity with its input power, P_c: clamping power, P_{th}: threshold power of S1

threshold for increasing pump power. At 4 times the threshold corresponding to 105 mW, the S2 linearly increases with input pump because it overcomes the linear cavity losses. At the same pump power, S1 experiences a clamping effect. That maintains constant the S1 output power until the onset of coherency for S3 line for a normalized pump power equals to 212 mW (8 Pth). Similarly, the cascaded process takes place. In figure (4.4b), a comparison is drawn between experiment and theory for MBL_{LQ}. Straight lines and stars correspond to experimental results and numerical simulations, respectively. The pump power P_{in} is normalized to the first Stokes power threshold. Also the Stokes output power (P_s) is normalized with the clamping power (P_c). When the power in S1 reaches the normalized output power needed to compensate S2 linear losses, coherent emission (green line) also takes place.

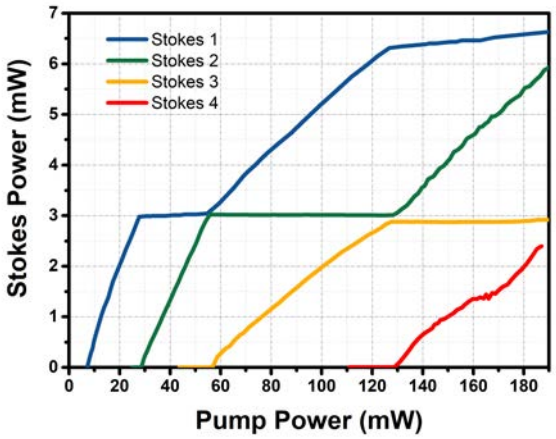

Figure 4.5: Power characterization of MBL_{HQ} cavity

It is worth to mention that when the output power of a Stokes order $(N+1)$ evolves monotonically with the pump power, the output power of the pumping Stokes order (N) is constant due to the clamping effect [177]. Stokes lines output power alternates between monotonous evolution and continuous power emission when the gain clamping occurs due to the onset of coherent radiation on the $N+1$ Stokes wave.

In order to study the influence of the photon lifetime, we have characterized the High-Q cavity (MBL_{HQ}) and shown the Stokes output power as a function of the input pump power in figure (4.5),(lines 1, 2, 3 and 4). The first Stokes (S1) laser threshold reduced from 26.5 mW to 7.2 mW by using a high-Q resonator ($Q_{\mathrm{h}} = 6 \times 10^8$) instead of a low-Q resonator ($Q_{\mathrm{l}} = 2 \times 10^8$). Stokes thresholds are summarized in the table (4.2). Similarly, slope efficiency of S1 is reduced from 37 % (low-Q) to 13 % (high-Q) because the output coupling power is decreased.

Table 4.2: Threshold of resonant BFL cavity

order	P_{in}/P_{th}	$MBL_{HQ}(mW)$	$MBL_{LQ}(mW)$
$S1$	1	7.2	26.2
$S2$	4	28.7	104.8
$S3$	8	57.2	209.4
$S4$	18	130.1	–

In conclusion, we study the stationary response of a resonantly pump fiber cavity through the Stokes output power as a function of the input pump power. We recall the principle of the cascaded generation of Brillouin Stokes waves in such a resonator. We have seen that the output power of a Stokes order (N) evolved monotonically with the pump power. Simultaneously, the output power of the pumping Stokes order $(N-1)$ is constant due to the clamping effect [178]. Thus, Stokes lines output power alternate between monotonous evolution and continuous power emission. In this section, we have shown the power dynamics of the MBL laser, which are reported in different articles [3, 34, 116]. The recall of this study helps to identify the various operating regimes of the MBL (monotonous and clamping regime). This clarification is of great importance to the following studies of RIN and frequency noise behaviors. The intensity noise dynamics of MBL will be discussed in the next section.

4.6 Relative intensity noise of resonant Brillouin laser

In optical communications, intensity noise affects the quality of the signal transmissions. So the intensity noise is an important parameter to characterize a laser. In resonant Brillouin laser, there are few experimental and theoretical results that are reported on RIN. A study shows a 20 dB RIN reduction at lower offset frequencies when compared to pump noise [34]. Similarly 15 dB RIN reduction was observed in higher offset frequency (2-18 GHz) [179].

This section reports one of the main contribution of this thesis regarding the intensity noise evolution of a multi-Stokes Brillouin laser. Since our objective is to determine the Brillouin laser RIN transfer function, we choose to make measurements independent of the pump RIN behavior by normalizing our Stokes RIN measurement with respect to the input pummp RIN. This normalization permits to get rid of the pump-RIN features, as for example intrinsic relaxation frequency, which do not relate to the Brillouin processes themselves. This normalization simplifies the identification of RIN features. Moreover, it allows our experimental observations to be compared to numerical simulations, for which an ideal white frequency noise is considered for the pump RIN.

In the following, we will present RIN simulations and its overall evolution for the Stokes waves S1, S2, and S3, as a function of the input pump power. Afterwards, we will focus on the RIN behavior for individual Stokes lines. Then we will discuss the impact of the cavity Q-factor on the MBL RIN. Finally, the impact of gain detuning will be evaluated. All experimental RIN results will be compared to numerical simulations performed with experimentally extracted parameters.

4.6.1 RIN simulations

To calculate RIN numerically, we introduce noise in the pump term of Eq.(4.1) as $S = S_0 + f_r$. Here f_r represents the fluctuations of the pump amplitude approximated by a Langevin white Gaussian noise source with $\langle f_r(t) f_r^*(t') \rangle = C\delta(t - t')$, where C is the auto-correlation strength of f_r. C is directly linked to the noise properties of the pump. Parameter C is used as a fitting parameter. This parameter disappears after the normalization of the Stokes RIN by the input pump RIN. Numerical simulations

correspond to time streams of 7 ms with a time resolution of 3 ns. The corresponding quite large number of events justify the use of a Gaussian distribution, instead of a Poissonian one through the central limit theorem [180]. Then we take the amplitudes fluctuations $\delta|A_\eta| = |A_\eta| - |A_\eta|_{\text{Steady}}$, and find their spectral densities $S^p_{\delta|A_\eta|}$ by converting them in the frequency domain and multiplying by the complex conjugated. RIN is finally determined by [4]:

$$\text{RIN} = \frac{8S^p_{\delta|A_\eta|}}{|A_\eta|^2_{\text{Steady}}} \tag{4.9}$$

RIN curves result from the averaging over 20 computations. Numerical and experimental RIN will be discussed in the following section.

4.6.2 RIN versus the cascade process

The usual measurement method of intensity noise characterization consists in the acquisition of the power spectral density of the intensity noise of the laser line. We use an electrical spectrum analyzer to obtain the PSD of the electrical signal at the detection level. The intensity noise measurement bench is explained in section (1.3). We used this technique to measure RIN of MBL.

As a first step in the study of RIN in MBL, we discuss the behavior of the RIN at 4 kHz from the carrier. An extended study at different frequencies was made in [34]. We report in figure (4.6 (right axis)) the RIN behavior of the three first individual Stokes lines as a function of the input pump power. Dotted lines correspond to measured RIN and starred lines to numerical simulations. We first focus on the $S1$ RIN. For a normalized input pump power of 1, corresponding to the $S1$ threshold, $S1$ RIN highlights 20 dB excess RIN with respect to that of normalized input pump. As mentioned before, the pump clamping between 1 P_{th} and 4 P_{th}, implies a transfer of pump fluctuations towards $S1$ [181]. Those fluctuations are amplified through the Brillouin gain explaining the excess noise. While going away from the threshold, the $S1$ output power increases implying a progressive decrease of the RIN towards the input pump RIN level. It is worth to notice that, in single mode Brillouin laser, the output Stokes RIN can even be lower than the input pump RIN. The noise reduction is strongly dependent on the cavity and Brillouin gain coefficient [125], and on the laser sensitivity to environmental perturbations as in a usual laser. In the present work, we take advantage of the SBS cascade effect to reduce Stokes noise level below the input pump RIN as described in the following.

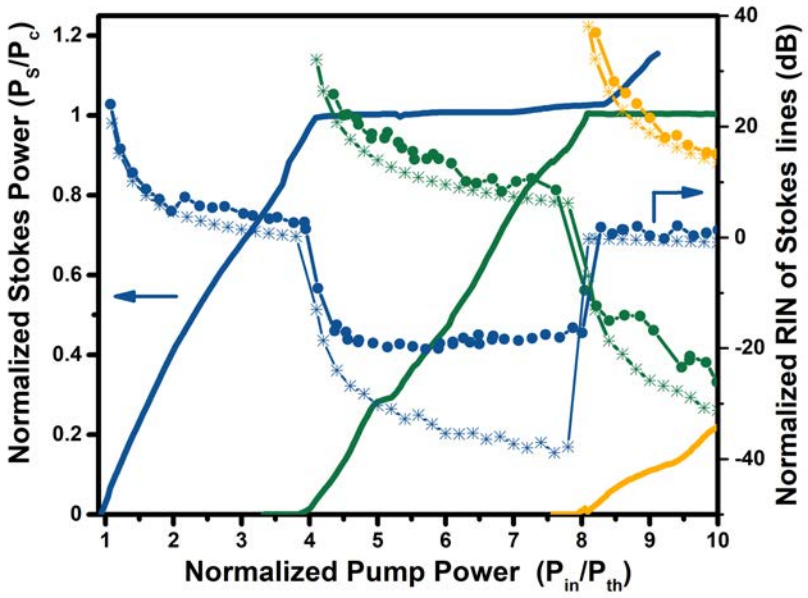

Figure 4.6: Left axis : Output Stokes power (P_s) normalized to the circulating power (P_c) versus input pump power (P_{in}) normalized to the Stokes 1 lasing threshold (P_{th}). Right axis: RIN of Stokes lines normalized to the input pump RIN. RIN amplitude is measured at 4 kHz from the carrier. Straight lines and full dots are experimental results. Stars are simulation results. Results are obtained with the "low-Q cavity" Brillouin laser, $P_{th} = 26.5$ mW.

Above $4P_{th}$, which corresponds to the $S2$ lasing threshold, the $S1$ experiences an abrupt RIN reduction up to 20 dB compared to the input pump RIN level. This reduction originates from the clamping effect of $S1$ due to the appearance of the stimulated $S2$ emission. In that regime, the "gain=losses" condition acts as a driving force to maintain the $S1$ output power constant (See Eq. (4.5)). Thereby, any intensity fluctuations of $S1$ are attenuated. At $8P_{th}$, coherent $S3$ emission arises. $S2$ becomes an efficient pump for $S3$, and similarly, intensity noise reduction occurs for $S2$ above the $S3$ lasing threshold power. Since $S2$ output power is clamped, $S1$ output power increases again proportionally to the input pump power. Consequences on the $S1$ RIN are instantaneous and manifest an increase of noise towards the input pump noise. Concerning the $S3$ RIN, close to the threshold, its RIN reaches 36 dB in excess to the pump laser RIN and progressively shortens towards the input pump RIN level. This high RIN level can be attributed to the noise transfer through the cascade effect. Indeed, SBS process implies energy conservation between involved waves. Then, RIN of uphill waves are transfered, and even amplified, to downhill waves. Moreover, as mentioned by Behunin [3] spontaneous anti-Stokes emission

can also degrade RIN of Stokes waves (which is not taken into account in our model).

Numerical simulations (starred lines) are superimposed on the experimental measurements. RIN behavior is very well reproduced by the numerical simulations in particular: (i) the monotonous reduction of RIN in single mode regime and (ii) the sudden reduction in the clamping regime. A discrepancy in the RIN reduction amplitude between the model and the experiment exists in the clamping regime. The model expects up to 40 dB reduction when the experimental results tend to -20 dB. As it will be demonstrated in the following of this thesis, this discrepancy is due to the gain detuning of the Brillouin laser. There is also a possible contribution coming from the anti-Stokes. Note however this AS noise increase is screened out by the noise contribution due to detuning.

In this section, we have shown the substantial impact of the clamping effect on the intensity noise properties of the laser. In other words, once the Stokes line labeled $N+1$ reaches the lasing threshold power, the "gain=losses" condition implies the clamping of the Stokes wave N that is playing the role of a pump. In this regime, fluctuations of Stokes N are sharply reduced, and up to 20 dB reduction compared to the RIN of the input pump laser is experimentally observed. Similar noise fluctuations reduction have been demonstrated in semiconductor optical amplifier (SOA) used in the saturation regime [182, 183, 184]. In the following section, we describe in detail the RIN behavior of individual Stokes order for various operating point to show the rich dynamics of RIN when MBL emission takes place.

4.6.3 RIN of individual Stokes lines

To get more insight on the intensity noise of individual Stokes lines, we propose to study the complete RIN noise behavior for various input pump powers. We organized this section into two parts. Firstly, we present RIN in the single mode regime, which is obtained for a pump power below 4 P_{th}. Secondly, we will explain the S1 and S2 RIN for a pump power above 4 P_{th}, which is called the "cascaded regime".

4.6.3.1 Single mode regime

The single mode regime is identified by a pumping rate between $1P_{th}$ to $4P_{th}$. In this regime, S1 wave is predominant in the cavity. In this first region, RIN decreases along with increasing pumping rate but it remains above the pump RIN level. We plot the RIN

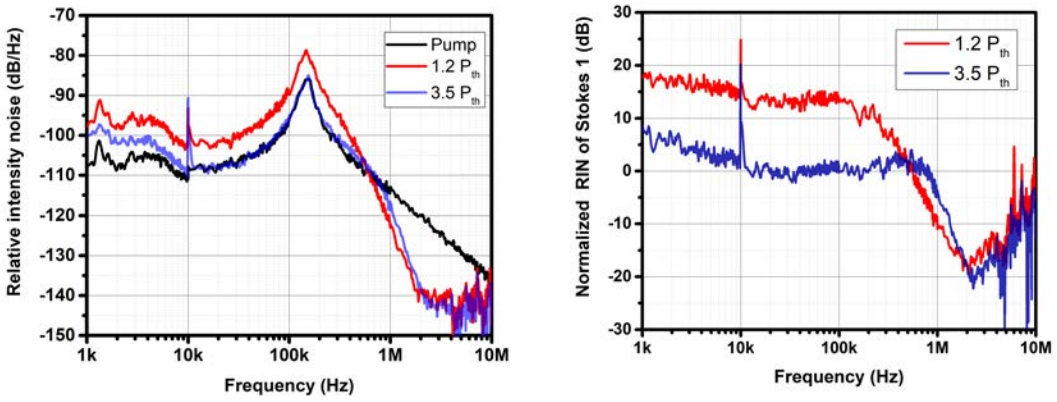

(a) (b)

Figure 4.7: Relative intensity noise reduction of the MBL Stokes1 when it is compared to the pump (a) Brillouin laser S1 intensity noise decreases with the injected pump power. (b) RIN of S1 normalized by the pump RIN.

of pump and S1 between 1 kHz and 10 MHz on figure (4.7 a) for a pump power below 4 P_{th}. In the present study, we used a Koheras laser as the pump laser and plotted in black. Due to the relaxation frequency of pump RIN at 154 kHz, it is difficult to interpret the real dynamics of Stokes RIN at different pumping rate. It is why we normalize the Stokes RIN with respect to its pump RIN as shown in figure (4.7 b). Now the S1 transfer function is clearly seen. As a matter of fact, this approach is valid only when the laser has a RIN level in excess to the intrinsic fundamental Brillouin noise.

As we can see on figure (4.7 b), the noise of S1 is constant over a range between 1 kHz to 600 kHz; at high frequencies, it decreases with around 20 dB per decade and reaches the noise measurement limit. The RIN follows the usual noise distribution of a class B laser featuring an oscillation of relaxation. Its origin comes from the coupling between phonons and photons similarly to photons and electrons in a class B diode laser [180]. An analytical expression for the relaxation frequency in single Stokes regime (P_{in} from 1 to 4 P_{th}) can be expressed as [4, 174]

$$f_{\text{R}} = \frac{1}{2\pi}\sqrt{\frac{|A_1|^2}{|A_0|^2} \times \frac{2\Gamma_B}{\tau^2}\left(\frac{2}{\tau} + \frac{\Gamma_B}{2}\right)^{-1}} \tag{4.10}$$

Figure (4.8) yields extracted frequency of relaxation from Stokes 1 in MBL_{LQ} (deep blue). The results of calculations of Eq.(4.10) are plotted in lines while experimental measurements are reported as points. The relaxation frequency evolves proportionally to the square root of the pump term as for a class B diode laser [185]. It shows an excellent match between the analytical expressions and experimental results.

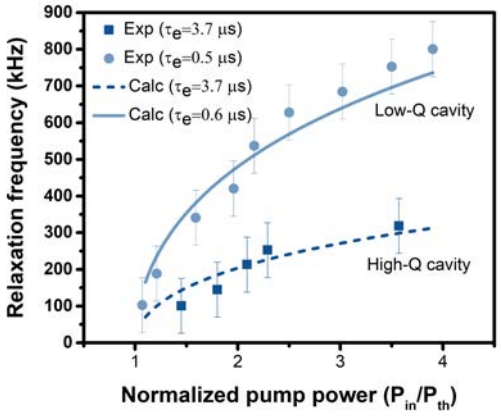

Figure 4.8: Relaxation frequency as a function of the normalized pump power for low-Q (light blue) and high-Q (deep blue) cavities. Lines represent the results of calculation of Eq. (4.10). Error bars (±75 kHz) represent the possible misreading of relaxation frequency on RIN curve.

In conclusion, we do not observe any RIN reduction in single mode regime. In resonant Brillouin laser, cascade effect will impact the noise dynamics, which is explained in the next section.

4.6.3.2 Cascaded regime

The cascaded regime is obtained for a pumping rate above $4P_{th}$. In this regime, higher Stokes waves are lasing in the cavity. For sake of simplicity, this cascaded regime is classified into clamping and monotonous regimes. Clamping regime is observed for S1, between $4P_{th}$ and $8P_{th}$. Similarly, S2 will be clamped for a pump power between $8P_{th}$ and $18P_{th}$ (see figure (4.4b)). These threshold values have been largely discussed in [34]. In monotonous regime, S1 and S2 are linearly increasing with pump power. We plot in figure (4.9) the RIN of $S1$ (blue color) and $S2$ (green color) between 1 kHz and 10 MHz for these two different operating regimes: i) clamping regime (Figure 4.9 (a) and (d)) ii) and monotonous regime (Figure 4.9 (b) and (c)). We will first focus on light colored curves corresponding to the low Q-factor cavity.

In the clamping regime (Figure 4.9 (a) and (d)), a 20 dB reduction of the $S1$ and $S2$ RIN occurs at low offset frequency (< 100 kHz). As explained previously, the onset of laser emission on S_{N+1} implies the clamping of S_N power and then the attenuation of its RIN amplitude. In the monotonous regime (Figure 4.9 (b) and (c)) Stokes power increases monotonically with the input pump power. At low offset frequencies Stokes

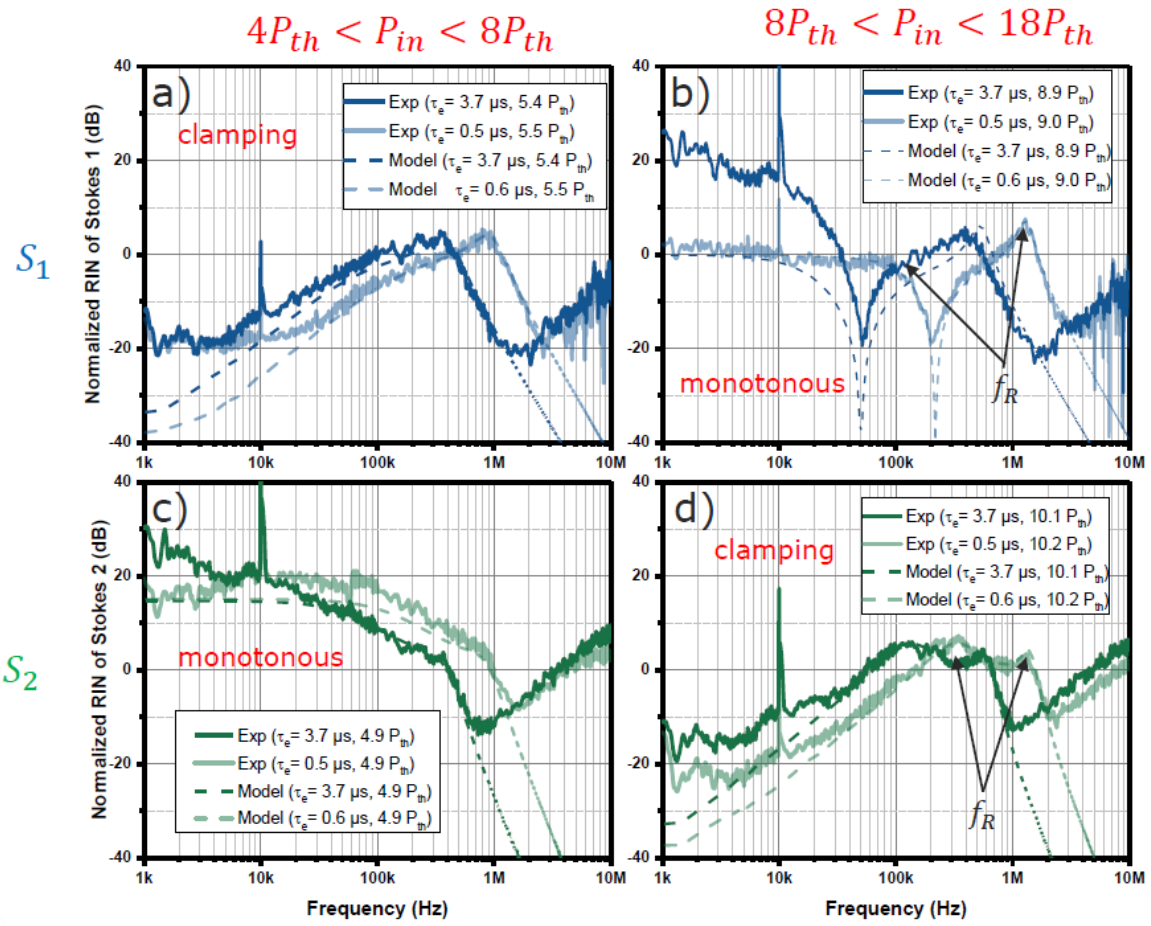

Figure 4.9: Normalized RIN of Stokes 1 (a, b) and Stokes 2 (c, d) lines for various input pump power. Full and dashed lines hold for experimental and simulation results respectively. Deep and light colors refered to high ($\tau_0 = 1.4$ μs, $\tau_e = 3.7$ μs) and low-Q factors ($\tau_0 = 1.4$ μs, $\tau_e = 0.5$ μs) respectively.

RIN rise to at least the pump RIN level. In this regime the noise transfer channel from "pump" to Stokes line is open. It corresponds to noise transfer from input pump towards $S1$ in figure (4.9 b) or from $S1$ towards $S2$ in figure (4.9 d).

For $P_{\text{in}} > 4P_{\text{th}}$ the laser shifts from single to multi-Stokes Brillouin lasing and then Eq. (4.10) is not valid anymore. The onset of $S3$ line for $P_{\text{in}} > 8P_{\text{th}}$ implies the appearance of multiple frequencies of relaxation originating from the complex Stokes waves coupling [3, 174]. In Figure (4.9 b), we can observe multiple relaxation frequencies from 100 kHz to 1.3 MHz due to the interaction of the photon and higher order Stokes phonons shown on the RIN of Stokes 1. Similarly, in Figure (4.9 d), the Stokes 2 has relaxation frequencies inside the interval [330 kHz, 1.4 MHz].

As shown in Figure (4.9), our experimental observations are well reproduced by numerical simulations based on our model. In particular noise reduction at low offset

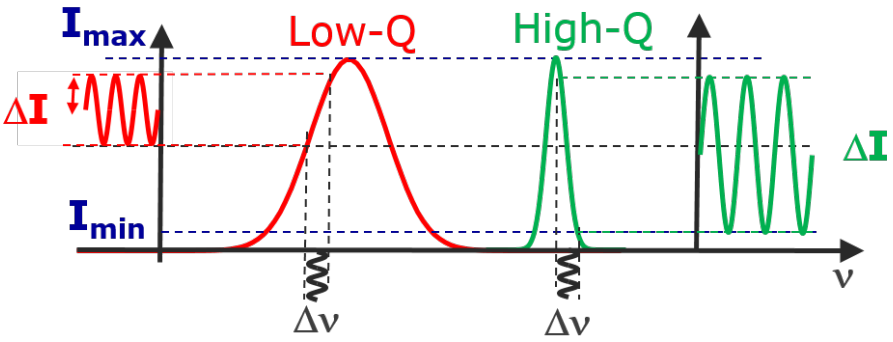

Figure 4.10: Schematic presentation of frequency fluctuations converted into intensity fluctuations cavity Q-factors.

frequencies, complex relaxation frequency shape and position and noise amplitude are reproduced. Similar RIN behavior is observed experimentally for incoming Stokes orders alternating sequences of low RIN level at low frequency offset when the Stokes line is clamped and high RIN level when the noise of previous Stokes order is efficiently coupled through SBS process. We studied the RIN dynamics of the MBL in single and cascaded region along the pump power. Now we are going to study the influences of the cavity parameters on RIN dynamics.

4.6.4 Impact of photon lifetime

In this section, we highlight the fundamental role of the cavity parameters on the RIN properties of the MBL. For this purpose, we recall the cavity parameters, which have been introduced in section (4.3.1). In order to obtain two different cavities, we vary the coupling coefficients to modify the coupling lifetime τ_e from $\tau_e = 0.5$ μs (low-Q) to $\tau_e = 3.7$ μs (high-Q). The intrinsic lifetime, τ_0 of the resonator remains the same since no additional losses are introduced ($\tau_0 = 1.39$ μs).

As it was mentioned in the previous section, figure (4.9) reports the RIN behavior for these two cavity configurations. The light and deep colored curves refer to the low-Q (shorter photon lifetime) and high-Q (longer photon lifetime) resonator configurations respectively. By comparing the RIN of both configurations, two main features may be associated with the total photon lifetime values.

Firstly, the frequency of the relaxation resonance is directly determined by the phonon lifetime and the total photon lifetime of the cavity as shown by Eq. (4.10). Indeed, the shorter cavity lifetime (low-Q) systematically highlights a larger relaxation frequency for

$S1$ and $S2$ lines. This behavior has been reported in figure (4.8), showing the relaxation frequency shift versus input pump power (1 and 4 P_{th}) for both configurations.

Secondly, low-offset-frequency Stokes-RIN levels are systematically higher in experiments for high-Q resonator. As an example, the $S1$ RIN in the high-Q configuration (deep blue) presents an excess noise of 25 dB with respect to the low-Q configuration (light blue) and to the simulations (figure 4.9 b). A possible explanation can be found in the relative frequency fluctuations between the input pump laser and the cavity resonance, for which the linewidth are then of the same order. The thinner the cavity resonance is, the worse the frequency fluctuations are. They are resulting in intensity fluctuations. Figure (4.10) shows the schematic presentation of frequency fluctuations converted in to intensity fluctuations in high-Q and low-Q cavities. Resonances of the cavity are presented in red and green colors for low Q-factor and high Q-factor cavities respectively. Resonances width of the high Q-factor cavities are thin and this leads into large intensity fluctuations from small frequency fluctuations. For low Q-factor cavity, the broader resonance implies a conversion factor from frequency to intensity, which is smaller. It is why the high-Q resonator RIN is more sensitive to thermal [4] and mechanical noises [125] and favor the transfer of low frequency pump fluctuations.

Those effects are not taken into account in the present model, which explains the discrepancy in the RIN level observed at low offset frequency in figure (4.9). In the next section, we will explain the discrepancy of the experimental and numerical results in the clamping regime due to the detuning of the gain bandwidth.

4.6.5 Influence of detuning

In the numerical simulations presented in the previous sections, we consider a zero-detuning operation of the S1 wave, which corresponds to a match between the frequency of the density wave Ω and the frequency of the maximum of the gain Ω_B. This configuration is very difficult to obtain since it implies that the SBS shift corresponds exactly to a multiple integer of the cavity FSR. Schematic presentation of gain detuning of Brillouin cavity is given in figure (4.11). In general, zero detuning condition is not fulfilled, even if a judicious choice of the pump wavelength helps to reach it, as the Brillouin shift Ω_B is dependent on the pump wavelength by $\Omega_B = 4\pi n V_A/\lambda_p$, also the SBS process is temperature dependent (see section (3.2)). To evaluate the impact of a gain detuning, we

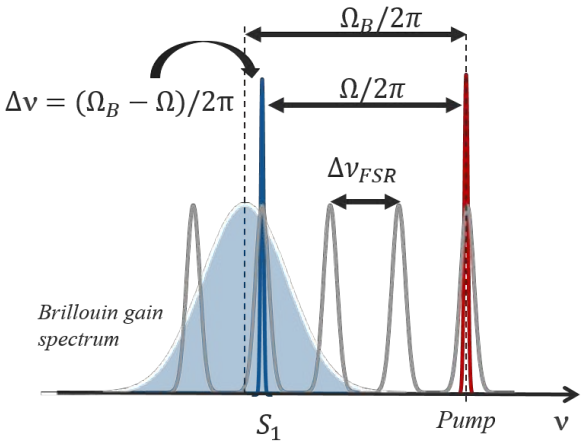

Figure 4.11: Schematics presentation of gain detuning of Brillouin cavity.

include in numerical simulations the gain detuning $\Delta\nu = (\Omega_B - \Omega)/2\pi$. This detuning implies that SBS Stokes waves are resonant at a frequency, which does not correspond to the frequency of the maximum Brillouin gain. Figure (4.12) focuses on the impact of the gain detuning on the RIN features of the S1 in (a) the clamped regime and (b) monotonous regime for the "low-Q cavity" configuration. Including the gain detuning allows one to fit much better the experimental results. Indeed, on figure (4.12a), we fit the S1 RIN by including a gain detuning of 500 kHz in the numerical simulations. This RIN at low frequency is much better reproduced suggesting that, even a weak detuning (500 kHz) with respect to the gain linewidth (27.5 MHz), strongly impacts the RIN-reduction performances of the S1 by 20 dB at 1 kHz. Similarly, at $9P_{th}$, by including a gain detuning of $\Delta\nu = 300$ kHz in the numerical simulations of the S1 RIN, the sharp deep profile observed around 200 kHz is attenuated and tends to that of the measurements. The discrepancy between experiment and simulations in the pump range $4P_{th}$ to $8P_{th}$ have to be attributed to the slight gain detuning that strongly limits the overall RIN-reduction performances of the MBL by up to 20 dB in the present study (see figure 4.6). These results suggest that further investigations have to be done to design optimized cavity that satisfies zero detuning conditions. In next section, we will confirm the presence of gain detuning in SBS cavity by pump-probe method.

Confirmation of detuning

A measurement setup realized to confirm the detuning of Brillouin cavity is shown on figure (4.13a). It enables to check the frequency position of a cavity resonance as a

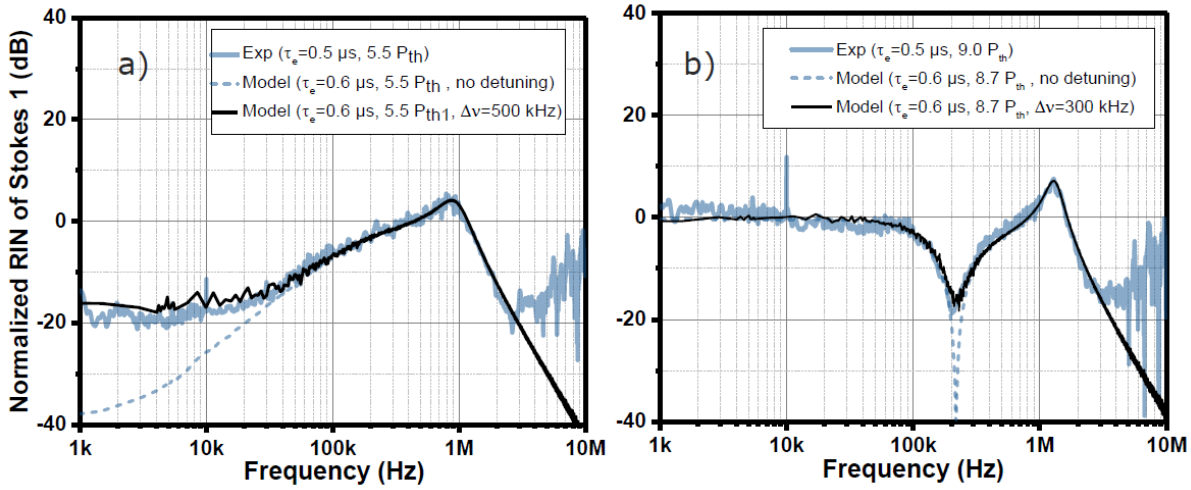

Figure 4.12: Evolution of the Stokes 1 RIN as a function of the gain detuning for a pump power of a) 5.5 P_{th} and b) 9 P_{th} in the low-Q cavity configuration.

function of a linear increase of the pump power. As we have seen in the section (2.4.2), resonances of the cavity can be measured using a probe signal. When a cavity resonance experiences gain, then this resonance will experience amplification. In case of Brillouin laser, the resonances under the gain bandwidth will experience amplification. As we have seen before, our FSR is 10 MHz, which is smaller than the gain bandwidth 27.5 MHz. If the resonance is at zero detuning condition, the central resonance at the maximum gain will be amplified; otherwise, for non-zero detuning, more than one resonance may be amplified.

The cavity is stabilized onto the pump laser-frequency for the generation of SBS. The resonances are scanned by the probe signal. In order to minimize the influence of the probe on the resonator operation, we attenuate the probe-signal power down to less than 1 mW. resolution. Firstly, we reduce the pump power and scan the resonance linewidth by the probe signal. Then we increased the pump power and measure its transfer function. These scanned signals are observed on an oscilloscope.

Figure (4.13b) shows measurements at different pump powers. At low pump power, the four identical cavity resonances are observed (black curve). When the pump power is increased, some of the resonances experiences SBS amplification. While the coupling regime is moving from under-coupling toward over-coupling regime (blue line). At higher pump power (red signal), the amplification of one resonance is clearly seen. Finally, at 14.4 mW, two modes are amplified; this shows that with this configuration, the S1 signal is not generated at the maximum gain position, because in that case, two side

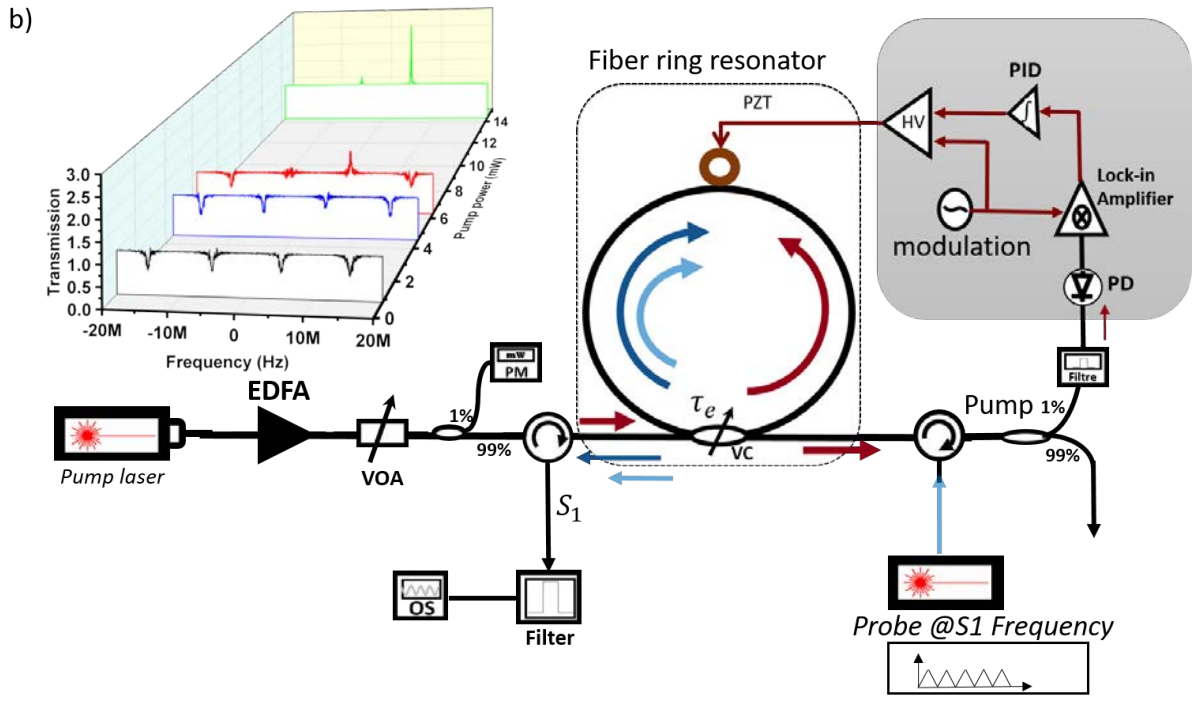

Figure 4.13: Experimental setup for gain detuning measurements; Koheras laser (brown) creates Brillouin scattering (dark blue) in the cavity and the probe laser (light blue) slowly scans the Brillouin gain. b) In the inset, different optical spectra measured thanks to an oscilloscope are given for different input pump powers.

modes would appear symmetrically around the central frequency. For the green line of the figure (4.13b), the main resonant laser frequency is thus detuned from the gain maximum. In order to reduce this detuning, the cavity length or pump wavelength has to be adjusted.

However, zero detuning is difficult to achieve for a long ring cavity. One solution is to have a servo-loop to discriminate the different modes [170]. Another solution is to implement a short cavity that can control the detuning by a pump-wavelength change. (which enables a fine control as a resolution of 1 pm will enable a control of the Brillouin shift with a resolution of 7 kHz).

In conclusion, gain detuning is an important factor. It has to be optimized for better noise performances. These studies are taken under the consideration of high pump-RIN.

4.6.6 Conclusion

In conclusion, we explicitly studied the RIN behavior of the Brillouin laser in a single mode and cascaded regime. We demonstrate that the S1 RIN is significantly reduced in the cascaded regime compare to the single-mode regime due to the clamping effect of the

pump power. Our study shows that the photon lifetime of the Brillouin cavity and a very small change of the detuning strongly modifies the relaxation oscillation frequencies and RIN reduction respectively. At higher pumping power, multiple relaxation oscillation frequencies are observed due to the interaction of different set of photon and phonon waves. These experimental observations are well supported by our numerical simulations. Moreover, we have shown that the pump RIN noise is less significant in the resonant Brillouin laser; it is more dependent on the cavity design and pumping power. In the next section, the frequency noise of the Brillouin laser will be experimentally studied.

4.7 Frequency noise of resonant Brillouin laser

Low-noise laser is widely required for different applications from coherent optical communications, defense, health, environment to basic sciences like optical-atomic clocks, precision spectroscopy and quantum sensing. Frequency noise reduction of single-mode Brillouin laser is well known and reported in literature.

In 2006, Geng *et al.* [126] studied the intensity and frequency noise of the resonant Brillouin fiber laser of S1. They showed a 10 dB reduction in S1 frequency noise compared to the pump frequency noise. Later in 2012, chip-based Brillouin laser was demonstrated using an ultra-high-Q micro-cavity [147]. They demonstrated that the fundamental frequency noise of S1 can reach 0.06 Hz^2/Hz. A dual microcavity Brillouin laser have been realized in 2015 [186], which exhibits a white frequency noise floor at 0.3 Hz^2/Hz. In this last example, the laser architecture is divided in two parts: one is a silica microdisk, which provides the Brillouin laser (S1), the second part is a large mode volume micro-rod cavity, which is used to stabilize the S1 line. This last part helps to reduce the laser flicker noise. In 2018, Brillouin laser was demonstrated on integrated Si_3N_4 waveguide platform with fundamental noise floor of 0.23 Hz^2/Hz [163].

All these lasers have very low intrinsic linewith, but integrated linewidth of these lases are relatively large because of sensitivity to temperature fluctuations, which spreads the linewidth. To overcome this problem, a large mode volume fiber resonator can be used as demonstrated in [165]. The short fiber cavity suppressed the thermo-refractive fluctuations. They have shown that Brillouin laser can reach 20 Hz integrated linewidth with a fundamental noise floor of 2 Hz^2/Hz. Theoretical analysis of S1 Brillouin laser noise dynamics under 4 P_{th} (single-mode regime) was studied in [4]. All the above mentioned

experimental observations are below 4 P_{th} (single-mode regime) pump power, and are in agreement with theoretical results [4]. About the multi-Stokes Brillouin laser, there are very few experimental results on frequency noise dynamics.

In this section, we will explain the main features of the frequency noise dynamics of single-mode and cascaded regime of the MBL. In a population inversion laser, coherency is provided by the effect of resonance inside the cavity. The gain medium does not preserve the coherency of the laser pump. In a Brillouin laser, however, the initial coherence of the pump laser is transmitted or even improved by the nonlinear process. The initial phase of the pump laser is redistributed on the Stokes and anti-Stokes waves. There is a strong relationship between the phase of the pump laser and the phase of the Brillouin laser obtained by nonlinear interactions between the pump wave, the Stokes wave and the acoustic wave propagating in the fiber [34]. As we have seen in non-resonant Brillouin laser, frequency noise is strongly dependent on cavity losses, acoustic damping rate and initial pump phase noise. But in the case of resonant Brillouin laser, frequency noise depends not only on the acoustic damping rate and cavity losses, but also on the detuning of the gain bandwidth, and phase noise carried from spontaneous anti-Stokes. Detuning of the gain bandwidth will enhance noise coupling between amplitude and phase fluctuations. Another noise transferring channel is the cascading effect; the resonant cavity can make multiple Stokes orders, which allows the re-injection of the spontaneous anti-Stokes $(N+2)$ on Stokes (N). This increases the phase noise of Stokes wave. It will be discussed in the coming sections. As we will show in the following, we have studied the dynamics of MBL above 4 P_{th} in the cascaded region.

As we have seen in chapter 3, non-resonant Brillouin laser frequency noise is strongly dependent on cavity losses and acoustic damping rate and initial phase noise of the pump. In the case of resonant Brillouin laser, frequency noise is also dependent on the detuning between the gain maximum and the resonant frequency, which will enhance noise coupling between amplitude and phase fluctuations as shown in section (4.6). The detuning is thus an important factor to control in order to optimize the noise performances of the Brillouin laser. Zero detuning is difficult to obtain in a long cavity; so we build a short cavity for the study of frequency noise, which allows us to control the detuning by changing the pump wavelength. Our experimental setup will be explained in section (4.7.1). We will then discuss the frequency noise dynamics of individual Stokes lines and their dependence on the pump power. In particular we will demonstrate experimentally, as far as we know

for the first time, recent theoretical predictions [3] that underline the role of anti-Stokes waves, which contribute to increase the phase noise level of laser Stokes lines. Moreover, we will study the influence of the Q-factor and detuning of the gain bandwidth on the frequency noise of the Stokes waves.

4.7.1 Short Brillouin cavity

We have seen the impact of the detuning on the RIN dynamics of MBL. It is thus important to reduce its contribution for better noise performances. It is why we develop a short cavity for frequency noise study. In the following, the laser cavity is detailed as well as the procedure to find the minimum detuning condition. Brillouin laser is generated by a tunable external cavity laser (Tunics OM), of which the signal is injected into a high-Q optical fiber resonator. The resonator consists of an optical coupler with the two arms spliced together. The effective length of the resonator is 2 meters and corresponds to an FSR of 100 MHz. This ensure a single mode operation since the gain bandwidth is $27.5 \pm 2\ MHz$.

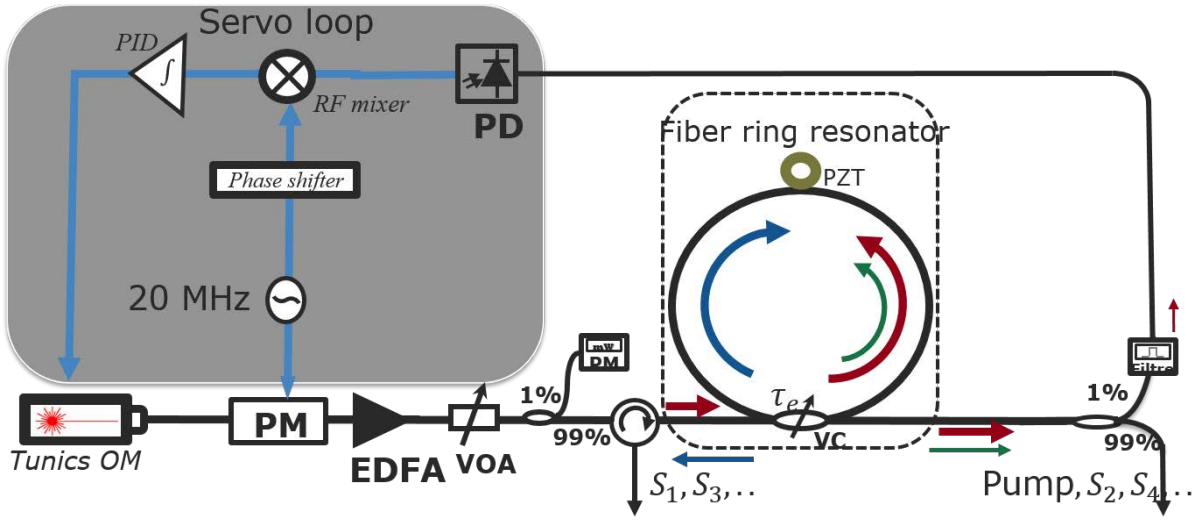

Figure 4.14: Experimental setup of the BFL cavity with PDH locking.

Figure (4.14) shows the experimental setup of Brillouin laser. Pump laser is stabilized on a cavity resonance by a PDH locking, which reduces the laser flicker noise as we discussed before in section (1.5.2). Pump laser frequency is phase modulated by radio frequency signal at a frequency of 20 MHz, which is much higher than the cavity response. The phase modulator (PM) will generate two side-band frequencies at 20 MHz. Cavity

transmitted signals are composed of resonant and off-resonant signals. The detected signals from the cavity produce a phase difference between the incident and cavity-stored signals through the beating between the carrier frequency and its side-bands. The signal is then demodulated with the same frequency, which is applied onto the phase modulator. The correction signal is sent to the laser current through a PID. The laser carrier-frequency follows the deviation of the cavity-resonance frequencies. Then it improves the light coupling into the cavity and generates a single Stokes wave.

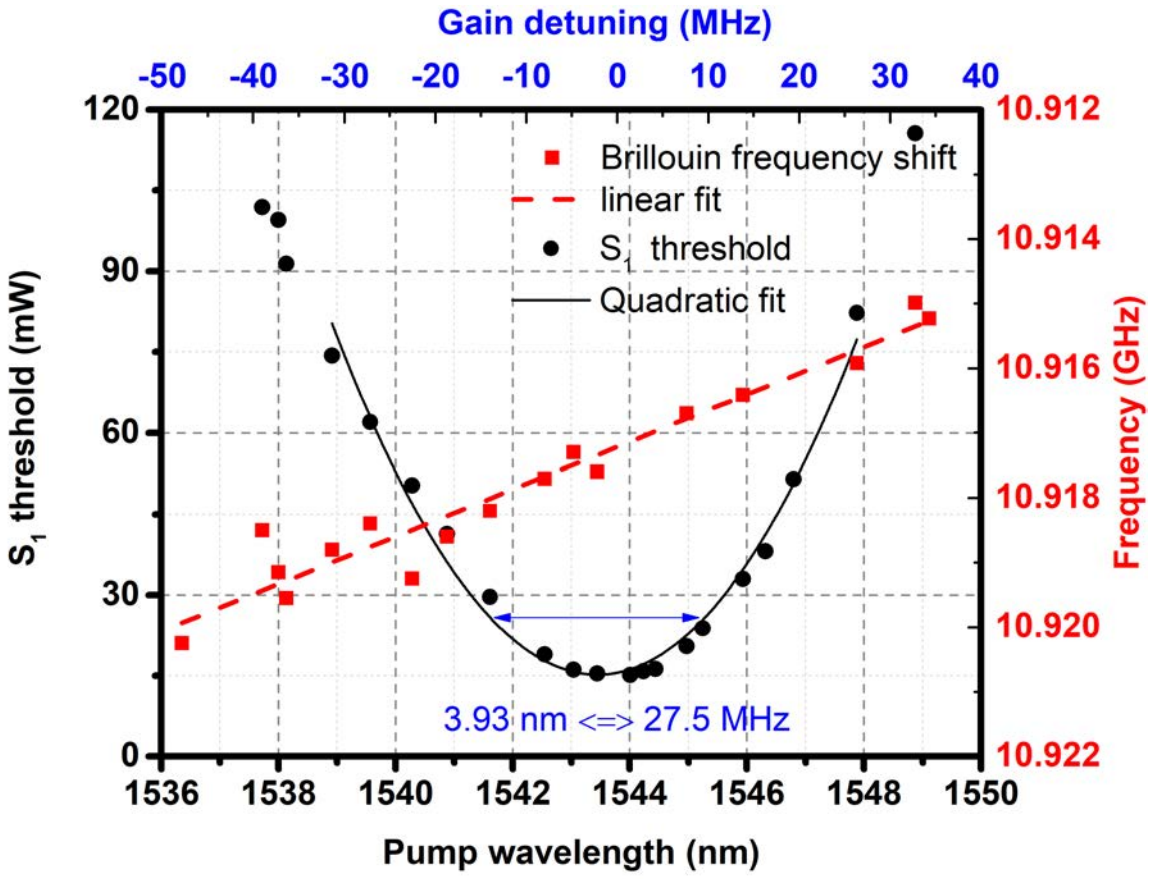

Figure 4.15: BFL detuning measurement: The measured Brillouin frequency shift (squares) and S1 threshold (dot) are plotted as a function of pump wavelength.

As mentioned before, the Brillouin laser efficiency is improved when the Brillouin shift is proportional to the cavity FSR. However it does not imply that the Stokes frequency is at the gain-maximum frequency due to temperature dependence of the Brillouin shift. In order to obtain this desired condition, the Brillouin shift may be adjusted by changing the pump wavelength or the cavity resonance thanks to a PZT. Reaching this condition of zero detuning, will also reduce the laser threshold. In the following, the detuning will be controlled by a change in the pump wavelength.

When the laser reaches a minimum threshold, we can conclude that the gain detuning is minimized ($\nu_B = n \times \Delta\nu_{FSR}$). The coupling ratio of the cavity is set at the critical coupling. Then the pump wavelength is varied from 1538 nm to 1548 nm. Simultaneously, the S1 threshold and the Brillouin frequency shift are measured. Figure (4.15) shows the experimental results of the threshold (black circles) and Brillouin frequency shift (red square dots) as a function of the pump wavelength. This Brillouin frequency shift is linear with a slope coefficient of $\frac{d\Omega_B}{d\lambda_P} = -2\pi \times 7MHz/nm$. The minimum threshold is 14.78 mW for the critical coupling. When changing the pump wavelength, the evolution of the S1 threshold is parabolic, which confirms the Brillouin gain bandwidth of 27.5 MHz [147] (1 nm corresponds to 7 MHz; the whole scan over 10 nm to 70 MHz).

From this analysis, we operated the pump laser at 1544 nm for minimizing the detuning in the following frequency noise studies. We have seen before in section (3.6) that Brillouin laser noise is dependent on the pump noise in non-resonant cavity. In resonant cavity it is also only dependent on the gain detuning, pump power and spontaneous anti-Stokes as it will be explained in the following section. For the sake of simplicity, firstly we will explain, in section (4.7.2), the influences of anti-Stokes spontaneous scattering on S1 frequency noise dynamics. Then we will detail influences of gain detuning on frequency noise spectrum of S1 and S2 in section (4.7.3). Finally, we will study the impact of photon lifetime in noise reduction and we will compare our results with other Brillouin lasers in section (4.7.4).

4.7.2 Frequency noise versus the cascaded process

Objective of this section is to detail the frequency noise dynamics of Brillouin laser in presences of higher order Stokes inside the cavity. We will explain the role of anti-Stokes generation in cascaded process and the associated enhancement of frequency noise.

4.7.2.1 Role of anti-Stokes wave

Recent theoretical results [3] have shown that the reduction of frequency noise will be affected by the coexistence of anti-Stokes waves in resonant Brillouin laser. The schematic picture of anti-Stokes generation in MBL is shown in figure (4.16). The x-axis is for the frequency and the dotted line are the cavity resonances, which are separated by the FSR ($\Delta\nu_{FSR}$). When the pump frequency (in red) is locked onto a cavity resonance, it

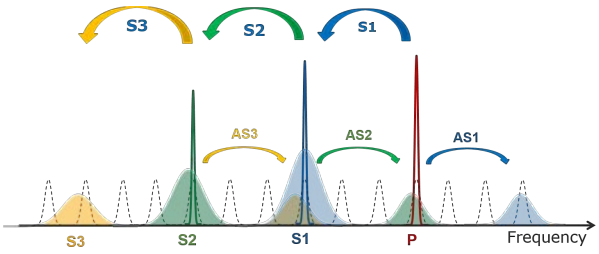

Figure 4.16: Schematic of anti-Stokes generations in cascaded Brillouin laser; dotted line : resonance of the cavity; shaded spectrum are Brillouin gain profiles for Stokes and anti-Stokes: S1 (blue), S2 (green), S3 (yellow); sharp peaks are Stokes stimulated laser lines and pump (green for S2, blue for S1, red for the pump).

will interact with thermally agitated phonons and it will create spontaneous Brillouin scattering. This spontaneous scattering will generate the Stokes (S1) and anti-Stokes (AS1) in the cavity (blue spectrum) [77]. When the pump power increases above the S1 threshold, the Brillouin process enters into the stimulated regime; note that to create one anti-Stokes photon, both a pump photon and a phonon have to be virtually absorbed [78]. This last condition lowers the efficiency of the anti-Stokes generation. Recall that for the generation of a Stokes photon, a pump photon is virtually absorbed and a phonon is created. Similarly, when the S1 power reaches P_{th}, spontaneous Stokes (S2) and anti-Stokes (AS2) are generated with a frequency respectively downward and upward shifted with respect to that of S1 (figure (4.16)). The upward shifted anti-Stokes (AS2) frequency is at the pump resonance frequency (small green spectrum). Similarly, when S2 reaches the threshold, which means at 4 P_{th}, spontaneous Stokes (S3) and anti-Stokes (AS3) are created (small yellow spectrum). This anti-Stokes wave will enhance the S1 frequency and intensity noise in the cascaded process (figure (4.17) extracted from reference [3]). In order to confirm the influences of anti-Stokes, we will study the frequency noise of S1 as a function of the input pump power in the following section. Recall that the intensity noise increase is screened out by the detuning effect. We clearly show that there is an effect on frequency noise.

4.7.2.2 Experimental results

The cavity is pumped by a tunable laser at 1544 nm, and the pump frequency is stabilized onto one cavity resonance using a PDH locking. The coupling ratio is fixed at 2 % (light coupled inside the cavity) and gives a threshold of 15 mW when detuning between Brillouin gain maximum and S1 resonance is minimum (figure (4.15)). The intrinsic

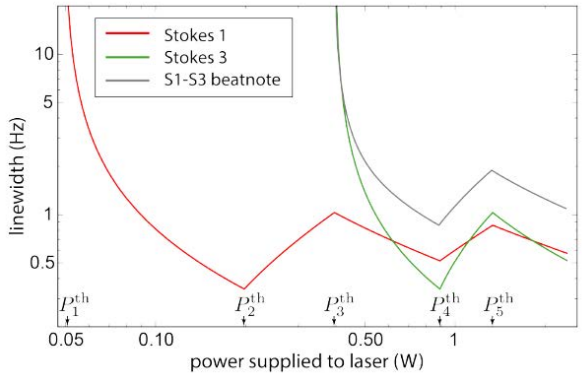

Figure 4.17: Theoretical results from [3] showing the degradation of linewidth of different Stokes components due to AS. This degradation can be equivalently observed in frequency noise (chapter 1, section 1.4.2).

photon lifetime is then $\tau_0 = 0.29\ \mu s$, which is equivalent to a Q-factor of 129 millions. The MBL S1 output is filtered using a 6 GHz bandwidth optical filter. As we have seen in section (1.4), the frequency noise of S1 is characterized using a fiber-based Mach-Zehnder Interferometer, which acts as an optical frequency discriminator. The experimental setup was explained in section (1.4.3). Here, we used a 200-meter fiber as a delay line for measuring the S1 frequency noise, which corresponds to a free spectral range of 1 MHz. The output of the MZI is detected and measured using photodetector and signal sources analyzer (FSW-13 GHz) respectively.

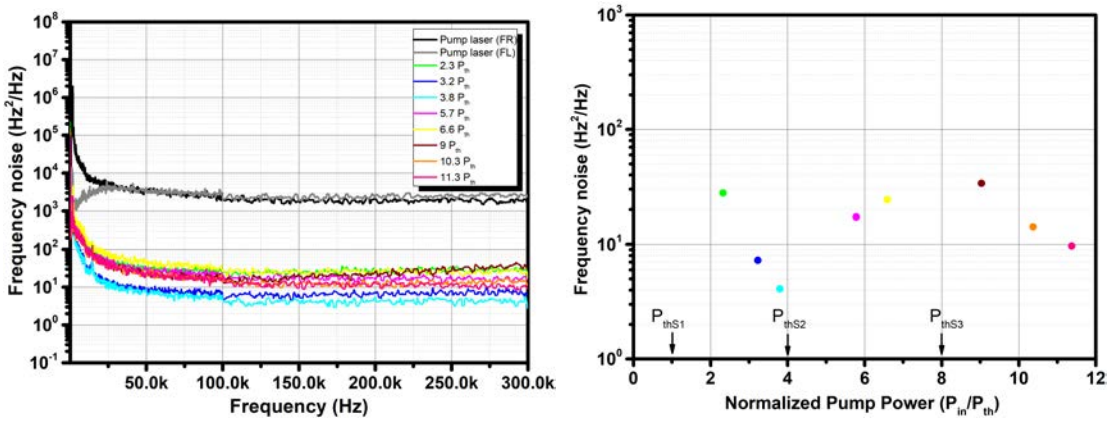

(a) (b)

Figure 4.18: Cascaded Brillouin laser frequency noise dynamics (a) S1 frequency noise at different pump powers in linear scale (b) S1 white noise at a fixed frequency of 200 kHz as a function of normalized pump power.

Figure (4.18a) shows the measured frequency noise of the pump and S1. The frequency noise of S1 is measured for different input pump powers. The interest is for the laser white noise. As we have seen before the Tunics OM laser has a white frequency noise of

2×10^3 Hz^2/Hz, which corresponds to an intrinsic linewidth of 6.28 kHz. Pump laser free-running (FR) is shown in black color and the frequency-locked (FL) pump laser is plotted in gray color, both lasers experience the same white noise level. S1 frequency noise is shown at different pumping rates from 2.3 P_{th} to 11.3 P_{th}. Experimental results reveal again the expected significant reduction in S1 frequency noise when compared to that of the pump noise; it also clearly demonstrates that reduction is varying with the input pump power. The white frequency noise of S1 reaches 4 Hz^2/Hz at 3.8 P_{th} pumping power; this gives a 26 dB reduction in frequency noise when compared to the pump noise level.

Figure (4.18b) shows the frequency noise level of S1 at a fixed frequency of 200 kHz as a function of the normalized input pump power. The S1 frequency noise decreases exponentially with the input pump power when the cavity is below the S2 threshold. A decrease of one decade corresponds to a variation of the normalized pump of 1.5 = 22.2 mW. At a normalized pump power of 2.32 corresponding to 34.8 mW (2.32 × 15), the noise level is 27.8 Hz^2/Hz; at 3.8 (57 mW) the noise level is 4.09 Hz^2/Hz. Once, it reaches the S2 threshold, frequency noise increases sharply from 4 P_{th} to 8 P_{th}. As explained before, for pump-power between 4 P_{th} and 8 P_{th}, S1 experiences a clamping effect in its output power, which lowers its noise. However an extra noise source is injected through the spontaneous anti-Stokes scattering AS3 due to the S2 Stokes wave. That will increase the S1 noise and will decrease the reduction factor "pump linewidth over S1 linewidth". Note that as shown in figure (4.16), the AS2 upward frequency (small green spectrum) is at the pump frequency while AS3 frequency (small yellow spectrum) is at the S1 downward frequency. The AS3 photons are feeding the S1 frequency and will absorb phonons, that are necessary for this AS3 generation. It leads to a frequency noise increase in the 4 P_{th} to 8 P_{th} region. Similarly, when S1 reaches 8 P_{th}, the frequency noise is decreasing inversely along with the pump power because S2 reaches the clamping regime that reduces the anti-Stokes presence in the cavity, which implies a noise reduction of S1 above 8 P_{th}. This result shows that the cascaded process may degrade the S1 linewidth up to one order of magnitude in presences of higher order Stokes in the cavity. Also, to the best of our knowledge, it is the first experimental validation of this theoretical study [3]. In the following section, we will explain the frequency noise spectrum of the Stokes waves.

4.7.3 Frequency noise of individual Stokes lines

In this section, we will study the individual Stokes signals frequency noise. The objectives of this section are to discuss the main advantages and limitations of noise reduction in MBL, at the view that we are now able to master the detuning between S1 and the gain maximum. The main problem in such analysis is the fact that the noise floor is a limitation that is quickly reached. To overcome this limitation, in the following studies we will use a low-Q cavity.

4.7.3.1 Analysis of low-Q cavity

A low-Q cavity will decrease the linewidth reduction and will permit to get a S2 frequency noise above the noise floor. It is why we investigate frequency noise of MBL by changing the coupling ratio. This allows us to increase the output power of S2. The cavity is set into under-coupling with an extrinsic photon lifetime of $\tau_e = 0.15\ \mu s$, and this implies that 13 % of the light is coupled into the cavity, leading to a decrease of Q-factor of 59.8 millions. The S1 MBL threshold is increased to 31.6 mW. To measure the frequency noise of the MBL laser, we use the same frequency noise characterization bench based on an MZI. However, to enlarge the measurement bandwidth up to 20 MHz, we reduce the branch asymmetry by using a fiber spool of 10 meters. This configuration allows the observation of detuning effects in Stokes lines frequency noise.

4.7.3.2 Analysis of S1 and S2 lines

Figure (4.19a), shows the single-mode and clamped regions of S1 frequency noises in the low-Q cavity configuration. As we discussed before in section (1.5.2), by doing PDH locking on a cavity resonance, pump low-frequency-noise can be reduced. In free-running operation, the laser pump exhibits a $186 \pm 18\ kHz$ integrated linewidth (with 10 ms observation time). By locking the pump laser frequency onto a cavity resonance, the flicker noise is reduced and corresponding the integrated linewidth was improved down to $6.28 \pm 0.6\ kHz$ for 10 ms observation time. Moreover, the SBS laser will again reduces flicker frequency noise then the S1 integrated linewidth is improved to a value lower than $2\ kHz$. However, the measured flicker frequency noise is limited by the noise floor of the measurement bench below 8 kHz Fourier frequency (see figure (4.19) gray dotted lines).

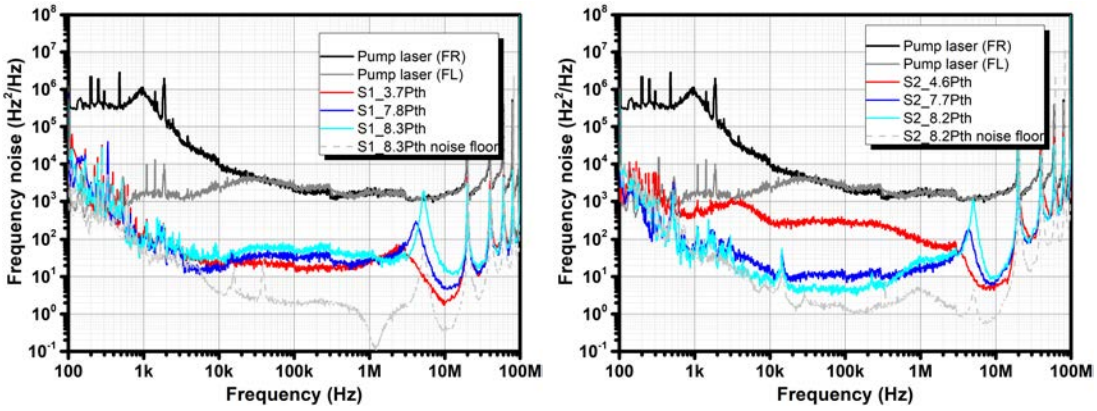

(a) (b)

Figure 4.19: (a) S1 frequency noise (b) S2 frequency noise for different regimes.

We are now interested in analyzing the white noise of the Brillouin laser. Below 4 P_{th} (single-mode regime), the frequency noise of S1 (shown in red color in figure (4.19a) has a white frequency noise of 20 Hz^2/Hz. The peak at 2.6 MHz can be explained by the theoretical results of Loh *et al.* [4] and will be discussed in the next section. Above 4 P_{th} (cascaded regime), S1 white frequency noise is increased due to an excess noise of spontaneous anti-Stokes S3. Similarly, S2 frequency noise is shown in figure (4.19b) at different pumping rates. Close to threshold, S2 frequency noise is limited to 2×10^2 Hz^2/Hz at 100 kHz. Along with increasing pump power, the S2 noise decreases by 3 dB down to 10 Hz^2/Hz at 7.7 P_{th} with a resonance frequency located close to 4.5 MHz. Close to the S3 threshold, the frequency noise of S2 reaches 4 Hz^2/Hz. The resonance peak in the experimental results will be explained in the next section.

4.7.3.3 Transfer function

The transfer function of pump frequency noise to Stokes frequency noise is shown in figure (4.20a) for a pump power of 1 mW with no detuning. The major trends of this transfer function were underlined in [4, 123]. At low frequency, it is constant up to a resonance frequency of 5 MHz, which corresponds to the relaxation frequency of the cavity. At higher frequencies, noise transfer decays with a -40 dB/decade slope. Similarly, figure (4.20)b shows the transfer of frequency noise from the pump to the Stokes when the pump frequency and SBS gain are detuned from the resonance [4]. At low frequencies, the pump noise to Stokes transfer function is constant like the zero detuning configuration. At higher frequencies the system has a sharp resonance near 5 MHz when the detuning is

nonzero. This resonance peak may be due to an amplitude-phase coupling between the pump amplitude noise and the the pump resonant frequency noise, of which the phase of the Stokes signal is related [4]. When the resonance is detuned from the gain maximum, then this noise transfer will be enhanced.

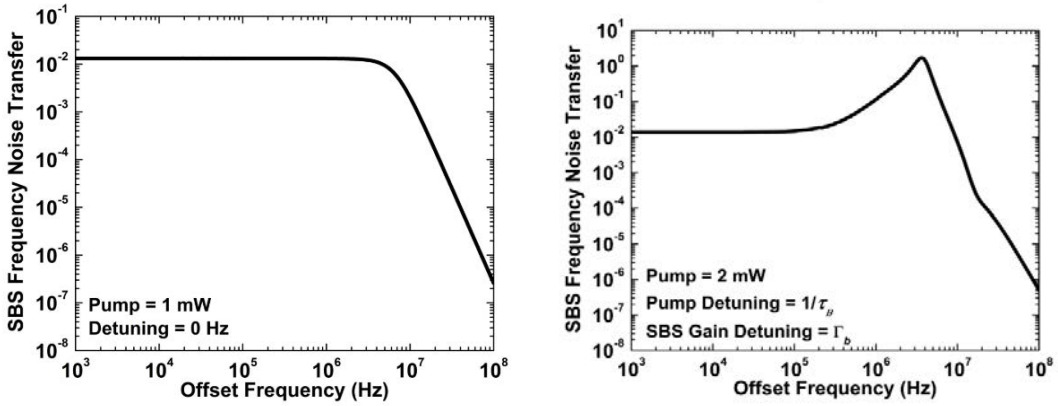

(a) (b)

Figure 4.20: The pump frequeny noise to Stokes frequency noise (a) zero detuning (b) with pump and SBS gain detuning [4].

The resonance frequency shifts in the figure (4.19) may be then explained by the pump power and detuning dependencies of the relaxation frequency. We have shown that the model that we introduce is able to perfectly match the experimental and theoretical RIN by adjusting the detuning and by inference the relaxation peak and its dependencies to detuning and pump power (report to figure (4.12), Eq. (4.10) for $P_{th} < P_{in} < 4\ P_{th}$). Thus the observation of the peak shift in the frequency noise when the detuning is nonzero along with the pump power may be interpreted at the view of our results on the RIN evolution with pump power and detuning. First of all, when the power is increased, there is a temperature increase inside the cavity that will imply a modification of cavity length and then of Brillouin-frequency shift and of detuning. Secondly if we made the assumption that there is an amplitude-phase coupling between intensity and phase noise, then the dependence of the relaxation frequency peak in the frequency-noise spectra may be understood by our results on RIN dependence. Thirdly, the peak in the the RIN spectra is a very complex function of power and detuning that could be simplified in simple cases (for instance Eq. (4.10) for $P_{th} < P_{in} < 4\ P_{th}$). It is perfectly simulated by our model that we have introduced and it can quantitatively explain the evolution of the resonant peak.

4.7.3.4 Frequency noise comparison of S1, S2

Figure (4.21) compares the frequency noise of S1 and S2 at the same pumping rate. We have seen, as expected that the noise of S1 is higher compared to that of S2 when the pump power is close to the S3 threshold. S1 frequency noise experiences an excess noise from the spontaneous anti-Stokes of S3 at 8.3 P_{th}. Also, a large resonance peak is obtained at 5 MHz due to a strong coupling between amplitude and phase noise, which confirms that cavity is no longer at zero detuning [4, 174]. Since the linewidth and frequency noise of a laser are closely related (section (1.4)), we observed that the Lorentzian linewidth of S1 reaches 125.6 Hz, S1 is acting as a pump for S2, which reduces the linewidth down to 12.56 Hz. In figure (4.21), the dotted lines gives the noise floors for the system, which was measured using a balance MZI with 10 m fiber in both arm of the MZI (the experimental setup is detailed in the section (1.4.4)). Above 20 kHz, S1 and S2 frequency noise are above the noise floor of the measurement bench. Below the 20 kHz, the measurement is suffering noise from the fiber in MZI. Unfortunately, the measurements are then limited below 20 kHz from the carrier. However it can be clearly seen that the frequency noise at the resonant peak is the same for S1 and S2, which is clearly a limitation in the reduction process, and that in the range [20 kHz, 300 kHz], the reduction ratio S1-pump frequency noise is around 16.9 dB while 10 dB is reached in the reduction ratio S2-S1 frequency noise. The ideal case will report a same reduction in the cascaded process, which is a nice way to reduce the frequency noise by operating on higher-order Stokes waves. As it was underlined in the Fresnel's thesis [34], the Brillouin shift is dependent on the Stokes order as it is dependent on the wavelength. It is why if a zero detuning is realized between

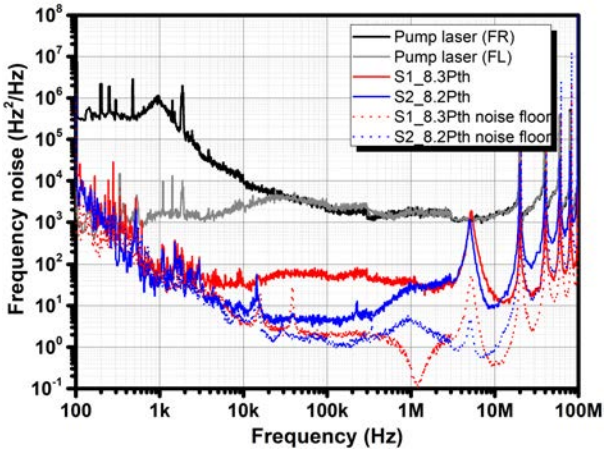

Figure 4.21: Comparison of frequency noise of S1 and S2 at 8.3 P_{th}

the pump and S1 in order to get the best performances in terms of noise as shown in figure (4.21), the detuning cannot be zero for the higher order Stokes (See appendix D). This will degrade the performances of frequency-noise reduction for higher orders. Note that the Brillouin shift is also dependent on the acoustical velocity in the medium. At constant pressure and temperature, it is constant.

4.7.3.5 Conclusion

We have experimentally studied the MBL frequency noise dynamics in single-mode and cascaded regimes. The Stokes frequency noise is filtered by the SBS process. We have implemented a locking, which reduces the flicker-noise of the pump laser. By using the combination of PDH and SBS process, we have achieved a low noise laser in terms of short and long term stability. Also, we have experimentally shown that spontaneous anti-Stokes of $(N + 2)$ enhances the noise of N th order Stokes, which confirms the theoretical prediction of [3]. Gain detuning induces additional noise to the Stokes signal [4, 174]. Also, we have underlined that the detuning effect is inherent to the cascaded laser. In the next sections, we are studying the impact of photon lifetime on the frequency noise of the S1.

4.7.4 Impact of photon lifetime

In this section, we will highlight the role of cavity parameters on the frequency noise of the Brillouin laser. For this study, we will compare the S1 frequency noise of two cavities with different coupling coefficients at 3.8 P_{th}. Cavity Q-factor is tuned by the coupling coefficient, as specified before; one is over-coupled with a Q-factor of 129 million, and the other under coupling regime with a Q-factor of 59.8 millions. Figure (4.22) reports the frequency noise of the S1 and the pump for the two-cavity configurations. The green and blue colored curves refer to high-Q and low-Q resonator configurations, respectively. The S1 frequency noise is sharply reduced in both configurations due to the combined influences of the photon decay rate and acoustical damping [123]. By increasing the photon lifetime in the cavity, the frequency noise reduction is improved by 6.9 dB from 20 dB to 26.9 dB, which is in agreement with theoretical values estimated using Eq. (3.5). In low-Q cavity, the estimated reduction factor is 20.5 dB, for a high-Q cavity it is 26.4 dB. This equation is only valid in single-mode SBS laser, especially at $4P_{th}$ above this

pump power, other noise enhancement channels are opened. In this example, S1 reaches a Lorentzian linewidth of 62.8 Hz for low-Q and 12.5 Hz for high-Q cavity configurations.

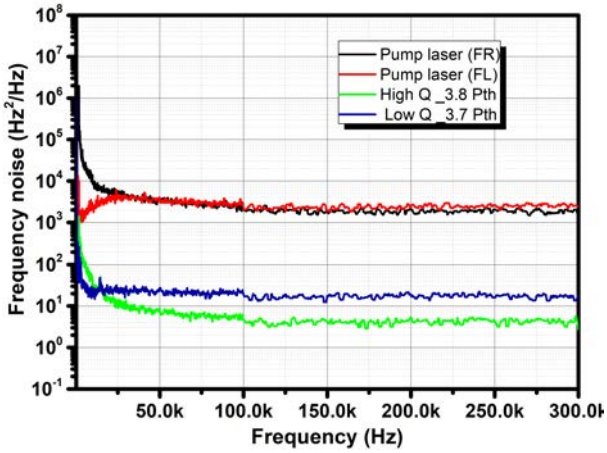

Figure 4.22: Impact of the photon lifetime in S1 frequency noise at a given pumping rate

In this thesis, we are studying the dynamics of the Brillouin laser noise, more than the ultimate noise limit. Even though it is interesting to compare our S1 frequency noise to reported Brillouin laser frequency noises in single mode regime. Table (4.3) sums up some of Brillouin laser linewidths from different articles.

Table 4.3: Comparison of S1 linewidth in different cavities

Cavity	Q-factor	Pump linewidth (Hz)	S1 linewidth (Hz)	Reduction (dB)	Frequency noise @ 100 Hz (Hz^2/Hz)	Output power @ $4P_{th}$ (mW)
Ultrahigh-Q wedge disk (silica on silicon)[147]	1.4×10^8	942	0.18	37	10^5	0.035
Si_3N_4 chip [163]	2.8×10^7	163	0.72	23.5	10^7	20
2 m Silica fiber (our)	1.3×10^8	6280	12.5	26.9	5×10^3	25

We are comparing three different Brillouin lasers: the first one is made of a silicon micro-disk, which gives a fundamental linewidth of 0.18 Hz with 37 dB reduction compared to that of the pump laser. The drawback of this laser is a very small S1 output power (micro watts) and high flicker noises. The second one is a Si_3N_4 integrated chip Brillouin laser with a fundamental linewidth of 0.72 Hz. Output power of the this laser is of the order of 10's of mW. The main disadvantage of this laser is a large flicker noise due to thermorefractive noise. For our laser, S1 linewidth is much larger compared to

presented value in table (4.3). Indeed, as stated in this thesis, the linewidth is strongly dependent on the pump laser linewidth. It turns out that our pump laser has a larger linewidth (6.28 kHz) when compared to those used in table (4.3). However the reduction factor is better than the integrated chip Brillouin laser. Even-though we were not able to estimate the integrated linewidth as the noise floor is reached below 20 kHz. Estimated integrate linewidth is 2 kHz at 10 ms. A similar architecture fiber Brillouin laser shows that S1 linewidth can reaches 20 Hz with a simple PDH lock, also it can be further reduced to 2 Hz by suppressing thermal fluctuations [165]. These results shows that fiber based Brillouin laser have great potential to realize stable single frequency lasers.

4.8 Conclusion

We have explained cascaded Brillouin fiber laser, in terms of noise and power dynamics by comparing experimental and analytical results. Theoretical results are obtained with the help of the modified coupled-mode equations. We define two regimes of operation depending on the pump power: single-mode regime and clamping regime, showing that low offset frequency RIN of considered Stokes lines can be strongly attenuated when operating in the clamping regime when pump RIN is larger. When working in a single-mode regime, our study of the impact of photon lifetime on the relaxation frequency shows an analogy between Brillouin fiber laser and Class B laser behavior. Experimental observations are well supported by numerical simulations that reproduced the main features of multi-Stokes RIN. Moreover, we have analyzed the significant influences of the gain detuning, which degrades the multi-Stokes RIN. Similarly, we studied the frequency noise dynamics in the cascaded region, which give nontrivial power dynamics; this behavior originated from the new noise channel open by the cascaded process. The experimental results have shown that this noise channel increases the linewidth of S1 at a higher pumping rate. However, the cascaded Brillouin laser exhibits excellent noise reduction in frequency. We reach a linewidth of the 12.5 Hz with a 129 millions Q-factor cavity. This results can be improved by using a low noise pump sources and high-Q cavity. Also, we demonstrated that the resonant Brillouin configuration suffers from noise coupling between amplitude and phase when it is detuned from the maximum of the gain bandwidth. From these experiments, we observed that SBS laser has excellent performances in frequency noise; its RIN characteristics appear worse compared to semiconductor lasers.

Our study gives inputs to design optimized Brillouin fiber laser in terms of RIN and frequency noise reduction.

General Conclusion

My Ph.D work is devoted to the understanding of noise dynamics in Brillouin fiber-ring lasers.
The first chapter of this manuscript presents generalities about laser noise. The relative intensity noise of lasers is theoretically explained and experimentally measured using a commercial DFB laser (KOHERAS). As well, the frequency noise of lasers is explained and related to the laser linewidth. An illustration is given thanks to a tunable laser (Tunics OM) and the linewidth is measured using the so-called $\beta - line$ technique, which is compared to a self-heterodyne technique. One important characterization of such noise qualifications is the evaluation of the noise floor of the bench and its analysis. This analysis was carried out using different delay lengths in the interferometer, which is used as an intensity converter for frequency fluctuations. This was discussed in details. In addition, in order to obtain long-term stability (on the order of a few hours) and to facilitate our measurements, we have demonstrated the stabilization of a laser on a fiber optic resonator using the Pound-Drever-Hall (PDH) technique. This technique allowed us to reduce the line width of the laser from 203 kHz down to 2 kHz.

In the second chapter, we have presented a general introduction of spontaneous and stimulated Brillouin scatterings. We have discussed and measured the key parameters of Brillouin scatterings, which are gain bandwidth, frequency shift, and Brillouin gain coefficient (maximum gain). A new Brillouin gain characterization method based on cavity ring-down method (CRDM) was introduced. The cavity characterization using CRDM, which helps to identify the coupling regime and intracavity losses of the resonator was also explained. Finally, we showed that the estimated Brillouin gain coefficient using CRDM is in good agreement with the results obtained from the self-heterodyne method. The CRDM method offers the possibility to obtain the material gain and cavity parameters, in a single experiment, using optical pump powers of the order of tens of

milliWatts, for cavities of short length (meter, millimeter, micrometer).

In the third chapter, we reviewed Brillouin laser development over the last few decades. This ranges from fiber ring laser to integrated chip-based Brillouin lasers. After explaining the difference between a resonant-pumped and non-resonant-pumped Brillouin laser, the single-mode or multimode character of the Brillouin laser operation is explained. Mod-hops of the non-resonant Brillouin laser are demonstrated using a 20-meter Brillouin cavity. We showed the suppression of mode hopping using a PDH locking technique. It allowed us to obtain a non-resonant Brillouin laser with long-term stability ($\sim$ hours). Moreover we are able to control key parameters such as cavity factors (Q-factor, coupling losses, internal losses), the detuning between the laser Stokes resonance and the gain maximum (or equivalently the Brillouin shift), pump noise. All these improvements allowed us to have a fine control of the laser, which has a long term stability, and to make a qualitative and quantitative comparison between theory and experiments. The analysis in this third chapter is made using standard model of noise transfer for non resonant Brillouin lasers. We demonstrated that our system can reach intrinsic linewidth of 1.3 Hz with a 37 ± 1 dB reduction when compared to the pump laser linewidth. Furthermore, we also showed that the intrinsic linewidth of the Brillouin laser can reach the level of mHz by cascading of two non-resonant Brillouin lasers.

In the last chapter, the noise dynamics of the resonant Brillouin laser is investigated experimentally using a fiber ring cavity. A model generalized to multi-Stokes Brillouin lasers was developed at Foton Institute; We have shown that our experimental measurements are in good agreement with the numerical simulations for the Brillouin laser. The RIN of Brillouin lasers with multi-Stokes orders was then experimentally and numerically studied in terms of pumping power, photon lifetime and gain detuning. We have confirmed that in the cascade regime of MBL, and for certain frequency ranges, the RIN can be reduced compared to single-mode regimes. This reduction is due to the saturation of the intracavity pump power due to the lasing process.

The photon cavity lifetime changes mainly the MBL relaxation frequency.

The detuning between the laser Stokes resonance and the Brillouin gain maximum has a great influence on the response of the RIN, even for small values ($\sim$ some 100 kHz). We detail theoretically and experimentally the increase of RIN by the influence of gain detuning.

Finally we tried to explore the limitations in frequency noise reduction using two

Brillouin lasers. We have shown that it is possible to cascade frequency-noise reduction by cascading two Brillouin lasers. However our bench noise floor is rapidly reached and prevented us to explore experimentally any limitation in noise reduction even if the thermal noise will be in any case a fundamental limitation. Nevertheless intrinsic linewidth of the order of 100 mHz is easy to get in a single-Stokes configuration or in a multi-Stokes configuration.

Other techniques are currently being explored to overcome the noise floor limitations of our frequency noise measurement benches in order to allow us to reach the fundamental limits of noise reduction for the intrinsic linewidth. It goes without saying that the low frequency noise (flicker noise, random walk) associated to thermal and mechanical fluctuations necessitates a slaving on a metrological reference to achieve small integrated linewidths. We succeeded to reach the kHz integrated linewidth using, as a reference, the resonance frequency of an fibered interferometer.

However, we have pointed out that there are fundamental limitations for Brillouins lasers with several Stokes orders. We have experimentally demonstrated, in agreement with theoretical predictions showing the penalty caused by anti-Stokes waves, that a degradation of frequency noise is observed. This can be lowered by operating far from the threshold of the analyzed Stokes order. Moreover the Brillouin shift is dependent on the Stokes order as its frequency shift is wavelength dependent. That will generate an inherent detuning when the Stokes order is increased. As precisely shown in this thesis, this detuning is degrading the RIN and the frequency noise by amplitude-phase coupling within the nonlinear process. It turns out that it is a severe limitation for Brillouin lasers with several Stokes orders, as a small detuning (less than 1 MHz) will affect both RIN and frequency noise.

The bad news is that controlling such a detuning on the MHz range seems to be out of reach of a low cost system, as it was expected in the project FUI SOLBO with partners IDIL, Lumibird, THALES, Photonics Bretagne, ISCR. The good news is that this work allows the engineering and sizing of these Brillouin laser systems and whether it can meet specifications in terms of RIN and frequency noise. Despites these limitations, interesting performances (Hz, 100 mHz intrinsic linewidth, kHz integrated linewidth) could be reached by designing properly the laser system.

As shown by many very recent publications on this topic, many groups around the world have understood the interest of Brillouin lasers to get very coherent wave. This

work is a contribution to the understanding of Brillouin fiber lasers with multi-Stokes orders.

Appendix A

Fresnel representation of laser noise

In figure (A.1a) shows the Fresnel representation of the complex field $\vec{E}(t)$ of the laser signal. The initial magnitude of field is $\vec{E}_0(t)$. Then the addition of a noise event, having magnitude of $\vec{\delta}E(t)$ due to spontaneous emission process. This will results in perturbation of both amplitude and phase of the original oscillating field.

The parallel component $\delta\vec{E}_{\parallel}(t)$ models the variation of the amplitude of the field $\vec{\delta}E(t)$. In a laser, such a variation will be systematically corrected by the phenomenon of gain saturation relative to the amplifying medium. This phenomenon decreases any increase in the amplitude of the field, so the amplitude fluctuations caused by the spontaneous emission are reduce. The gain saturation phenomenon therefore acts as a restoring force that tends to stabilize the amplitude of the wave.

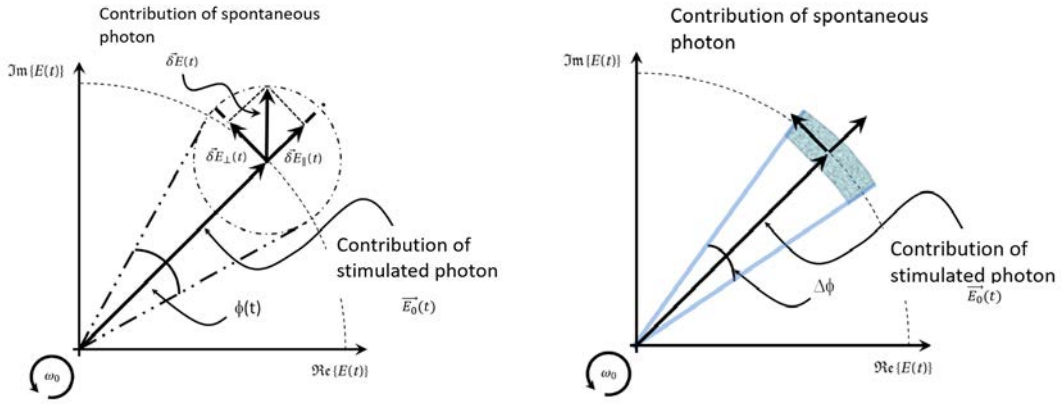

(a) (b)

Figure A.1: (a) Schematic representation of spontaneous emission of laser field (b) Contribution of stimulated emission generated by optical amplification and filtered by an optical cavity.

The variation of the phase is modeled by the component $\delta\vec{E}_{\perp}(t)$, perpendicular to the field $\vec{E}_0(t)$. Unlike intensity variation, no phenomenon equivalent to that of gain saturation exists to damp a phase variation in a laser. It is therefore understandable that the phase variations will accumulate thus making the phase of the field evolve according to a diffusion process. The phase of a laser follows the process of a random walk. These phase fluctuations prevent the power spectrum of a laser from having a infinitely linewidth (i.e., zero) but rather from a fundamental linewidth.

Figure (A.1b) gives an image of the Fresnel vector of the laser field, in a rotating at the average optical pulsation of the laser field filtered by an optical cavity. The uncertainty on the field is represented by a ring arc. As has been explained previously, the radial component gives the intensity noise generated and attenuated by the saturation of the laser gain. The tangential component gives the phase noise. This arc is moving erratically due to temperature or acoustical noise on slow dynamics. It could take minutes to cover a portion of the circle by a slow erratic drift of the arc with a stochastic signal containing many frequencies. The angle arc is actually limited because it is related to the fineness of the hot cavity, typically 10^5 for a DFB semiconductor laser, given for a 1 MHz linewidth and a free spectral range of 100 GHz. In fact, a flicker noise would lead to a random rotation of this Fresnel vector (with its ring arc) in a low frequency range.

Appendix B

g_{th} - factor

The analytical equation for threshold and its detailed derivations can be found in [86]

$$P_{th} = \frac{g_{th} A_{\text{eff}}}{k_{polar} g_B L_{\text{eff}}} \tag{B.1}$$

$$g_{th} = \Psi \left(1 + \frac{\frac{3}{2} ln(\Psi)}{\Psi - \frac{3}{2}} \right) \tag{B.2}$$

$$\Psi = -ln \left[\frac{2\sqrt{\pi}\gamma\Theta}{\mu\alpha} e^{-\alpha_f L} (1 - e^{-\alpha_f L}) \right] \tag{B.3}$$

$$\Theta = \frac{T.\nu_p.\Delta\nu_B}{k_{polar} 2.\nu_B} \tag{B.4}$$

$$\gamma = \frac{g_B k_{polar}}{A_{\text{eff}}} \tag{B.5}$$

In 1972, Smith et al.[187] approximated the value of g_{th} is 21 in silica fiber with $\mu = 1$ and large fiber losses coefficient. This value is over-estimated due to the available fibers in 1972 [33]. $\mu = 1$ means that the input pump and the Stokes power are the same order. In the manuscript $\mu = .01$ because it enables to be at the middle of the transition between the spontaneous ans stimulated regime. This ratio means that the Brillouin threshold is reached when the back-scattered power is equal to 1% of the pump power [83, 84]. We estimate g_{th} equal to 11.24 for 26 km SMF-28, considering a Brillouin gain coefficient extracted using the self-Heterodyne method and material parameters (see table 2.3,2.2).

Appendix C

Gain distribution

Then the expression of the gain for a stimulated Brillouin regime is Gaussian shape:

$$g_B(\nu) = \exp\left[- ln(2)\Big(2\frac{\nu}{\Delta\nu_B}\Big)^2\right] \tag{C.1}$$

for

$$\nu = \pm\Delta\nu_B/2 \tag{C.2}$$

$$g = g_B \exp(-ln(2)) = g_B/2 \tag{C.3}$$

If the ratio between modes under the Brillouin gain is 20 dB, then the corresponding frequency is written:

$$g_B = \exp\left[- ln(2)\Big(2\frac{\nu}{\Delta\nu_B}\Big)^2\right] = \frac{g_B}{100} \tag{C.4}$$

So that

$$\exp\left[- ln(2)\Big(2\frac{\nu_\pm}{\Delta\nu_B}\Big)^2\right] = \exp(4605) \tag{C.5}$$

And

$$\exp\left[- ln(2)\Big(2\frac{\nu_\pm}{\Delta\nu_B}\Big)^2\right] = \exp(-4605) \tag{C.6}$$

Finally,

$$\nu_\pm = \pm\frac{1}{2}\sqrt{\frac{4605}{ln(2)}}\Delta\nu_B = \pm 1289\Delta\nu_B \tag{C.7}$$

To consider a side-mode suppression (SMSR) of 20 dB, the FSR has to be greater than 2.58 $\Delta\nu_B$ (see figure(C.1)). In practice, as the gain cannot be considered as homogeneous, it is difficult to fix a ratio between FSR and the gain bandwidth in order to assure a single-mode operation. It turns out that a ratio of $\Delta\nu_{FSR}/\Delta\nu_B$ is a good indication to have a single mode operation even if there could be situation where it is not a sufficient one. Then we will consider in the following the ratio $\Delta\nu_{FSR}/\Delta\nu_B$ as a reference.

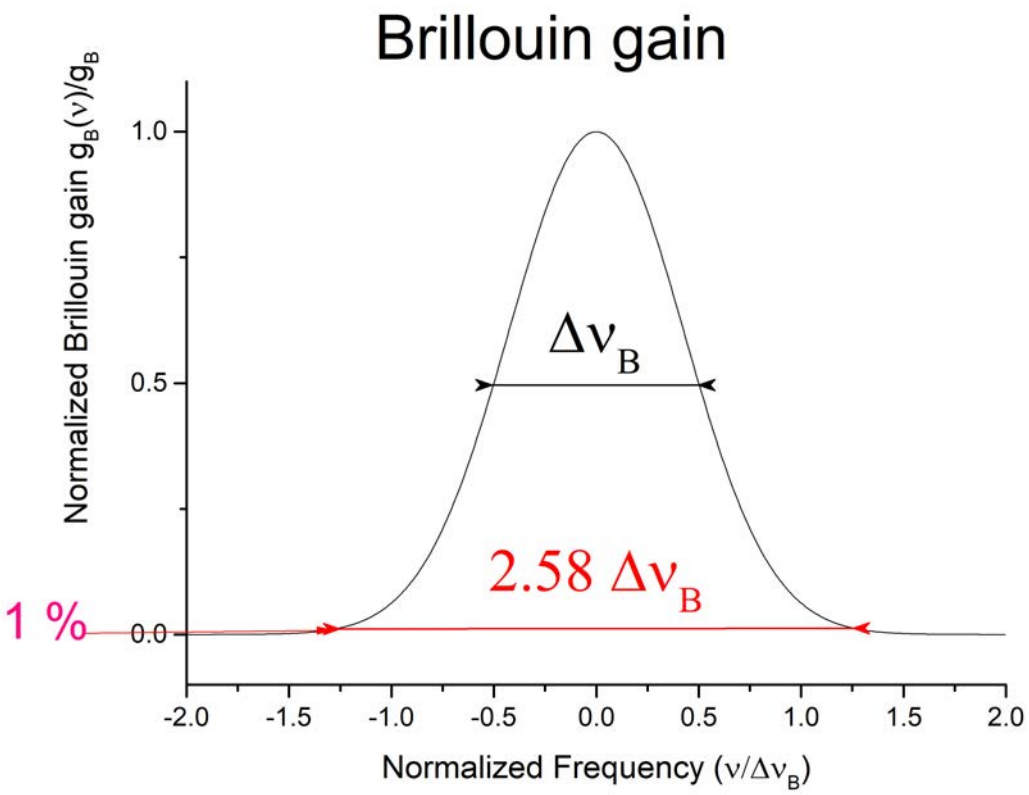

Figure C.1: Representation of the Brillouin gain and side mode suppression

Appendix D

Brillouin shift and gain detuning in multi-Stokes Brillouin laser

Gain detuning is inherent in the multi-Stokes Brillouin lasers. The Brillouin laser is realized by the matching of the $N \times \Delta\nu_{FSR}$ of the cavity and Brillouin shift ν_B. It depends on the refractive index, acoustic wave velocity of the medium and pump wavelength.

$$\nu_B = \frac{2nV_A}{\lambda_P} \tag{D.1}$$

The Brillouin shift varies with pump wavelength by ratio of 7 MHz/nm. As we know that the each generated Stokes waves are downshift from the pump frequency, so the Brillouin shift will be change from Stokes 1 to Stokes 2. Figure (D.1) gives a picture of

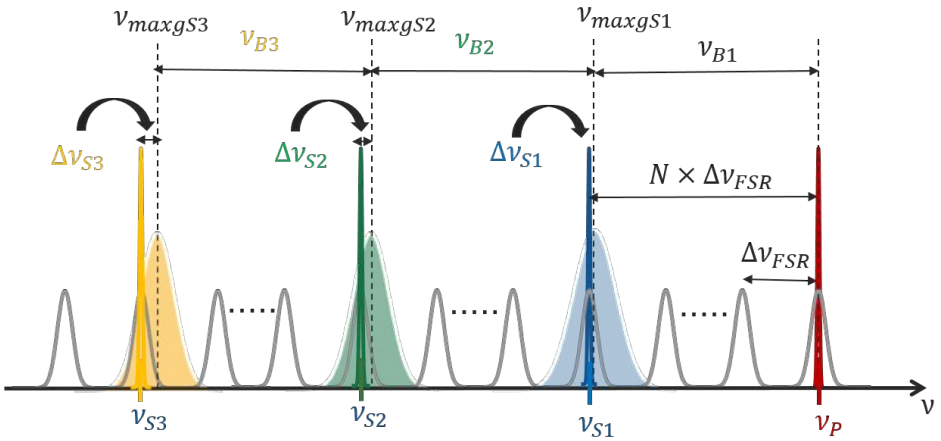

Figure D.1: Illusation of gain detuning in multi-Stokes Brillouin laser

detuning in multi-Stokes Brillouin laser. The pump laser frequency ν_P (red) is in red while resonant modes are in gray color. Shared region is the Brillouin gain line, sharp

peaks are the Stokes orders. Here we assume that ideal conditions like constant pressure and temperature so that V_A remains constant.

The Brillouin shift ν_{B1} due to the pump ($\nu_p = c/\lambda_p$) may be written as:

$$\nu_{B1} = Z_A \nu_p \tag{D.2}$$

with $Z_A = \frac{2nV_A}{c}$.

Then the frequency ν_{maxgS1} of the gain maximum for Stokes 1 is at:

$$\nu_{maxgS1} = \nu_p - \nu_{B1} = \nu_p - Z_A \nu_p \tag{D.3}$$

And the Stokes frequency ν_{S1} is given by:

$$\nu_{S1} = \nu_p - N\Delta\nu_{FSR} \tag{D.4}$$

The detuning $\Delta\nu_{S1}$ is for the first order Stokes:

$$\Delta\nu_{S1} = \nu_{S1} - \nu_{maxgS1} = Z_A\nu_p - N\Delta\nu_{FSR} \tag{D.5}$$

N is the number of free spectral range necessary to have a resonance under the gain curve. When the Stokes 2 is generated from the first order Stokes, the associated Brillouin shift is slightly different from ν_{B1} and is written:

$$\nu_{B2} = Z_A\nu_{S1} = Z_A\nu_p - Z_A N\Delta\nu_{FSR} \tag{D.6}$$

The frequency of the maximum gain is then:

$$\nu_{maxgS2} = \nu_{maxgS1} - \nu_{B2}\nu_{maxgS2} = \nu_p - 2Z_A\nu_p + Z_A N\Delta\nu_{FSR} \tag{D.7}$$

And the Stokes frequency is written as:

$$\nu_{S2} = \nu_p - 2N\Delta\nu_{FSR} \tag{D.8}$$

The detuning $\Delta\nu_{S2}$ is for the second order Stokes:

$$\Delta\nu_{S2} = \nu_{S2} - \nu_{maxgS2} = 2Z_A\nu_p - Z_A N\Delta\nu_{FSR} - 2N\Delta\nu_{FSR} \tag{D.9}$$

$$\Delta\nu_{S2} = \nu_{S2} - \nu_{maxgS2} = 2Z_A\nu_p - (Z_A + 2)N\Delta\nu_{FSR} \tag{D.10}$$

For Stokes 3,

$$\nu_{B3} = Z_A\nu_{S2} = Z_A\nu_p - Z_A 2N\Delta\nu_{FSR} \tag{D.11}$$

$$\nu_{maxgS3} = \nu_{maxgS2} - \nu_{B3} \tag{D.12}$$

$$\nu_{maxgS3} = \nu_p - 3Z_A\nu_p + Z_A N\Delta\nu_{FSR} + Z_A 2N\Delta\nu_{FSR} \tag{D.13}$$

$$\nu_{maxgS3} = \nu_p - 3Z_A\nu_p + 3Z_A N\Delta\nu_{FSR} \tag{D.14}$$

$$\nu_{S3} = \nu_p - 3N\Delta\nu_{FSR} \tag{D.15}$$

$$\Delta\nu_{S3} = \nu_{S3} - \nu_{maxgS3} = 3Z_A\nu_p - Z_A 3N\Delta\nu_{FSR} - 3N\Delta\nu_{FSR} \tag{D.16}$$

$$\Delta\nu_{S3} = \nu_{S3} - \nu_{maxgS3} = 3Z_A\nu_p - 3(Z_A - 1)\Delta\nu_{FSR} \tag{D.17}$$

The general expressions for the order ζ are then given by:

For the Stokes frequency

$$\nu_{S\zeta} = \nu_p - \zeta N\Delta\nu_{FSR} \tag{D.18}$$

For the Brillouin shift

$$\nu_{B\zeta} = Z_A\nu_{S(\zeta-1)} = Z_A\nu_p - Z_A(\zeta - 1)N\Delta\nu_{FSR} \tag{D.19}$$

For the frequency of the gain maximum

$$\nu_{maxgS\zeta} - \nu_{maxgS(\zeta-1)} = -\nu_{B\zeta} \tag{D.20}$$

or

$$\nu_{maxgS\zeta} - \nu_{maxgS(\zeta-1)} = -Z_A\nu_p + (\zeta - 1)Z_A N\Delta\nu_{FSR} \tag{D.21}$$

With

$$\nu_{maxgS0} = \nu_p \tag{D.22}$$

Which gives from series law

$$\nu_{maxgS\zeta} = \nu_p - \zeta Z_A\nu_p + \frac{1}{2}\zeta(\zeta - 1)Z_A N\Delta\nu_{FSR} \tag{D.23}$$

It follows that the detuning is equal to:

$$\Delta\nu_{S\zeta} = \nu_{S\zeta} - \nu_{maxgS\zeta} = \zeta Z_A\nu_p - \frac{1}{2}\zeta(\zeta - 1)Z_A N\Delta\nu_{FSR} - \zeta N\Delta\nu_{FSR} \tag{D.24}$$

When the first detuning is null, then $Z_A\nu_p = N\Delta\nu_{FSR}$ and the detuning is then written as:

$$\Delta\nu_{S\zeta} = \nu_{S\zeta} - \nu_{maxgS\zeta} = \zeta Z_A\nu_p - \frac{1}{2}\zeta(\zeta-1){Z_A}^2\nu_p - \zeta Z_A\nu_p \tag{D.25}$$

It follows the general formula for the detuning

$$\boxed{\Delta\nu_{S\zeta} = -\frac{1}{2}\zeta(\zeta-1){Z_A}^2\nu_p} \tag{D.26}$$

Variable	Expression
Stokes frequency	$\nu_{S\zeta} = \nu_p - \zeta N\Delta\nu_{FSR}$
Brillouin Shift	$\nu_{B\zeta} = Z_A\nu_p - Z_A(\zeta-1)N\Delta\nu_{FSR}$
Frequency of the maximum gain	$\nu_{maxgS\zeta} = \nu_p - \zeta Z_A\nu_p + \frac{1}{2}\zeta(\zeta-1)Z_AN\Delta\nu_{FSR}$
Detuning	$\Delta\nu_{S\zeta} = \zeta Z_A\nu_p - \frac{1}{2}\zeta(\zeta-1)Z_AN\Delta\nu_{FSR} - \zeta N\Delta\nu_{FSR}$
Detuning if S1 detuning is 0	$\Delta\nu_{S\zeta} = -\frac{1}{2}\zeta(\zeta-1){Z_A}^2\nu_p$

From these equations, we can obtain Stokes detuning for any stokes orders. In table (D.1) gives the values of detuning, wavelength and the Brillouin shift for Stokes order up to 5. These detuning are in the MHz range. It has thus an important influence on the noise properties. For Stokes 2, the detuning is 610 kHz. The detuning is increasing with number of Stokes orders.

Table D.1: Gain detuning in cascaded Brillouin laser

Order	wavelength (nm)	$\nu_{B\zeta}$ (MHz)	$\Delta\nu_{S\zeta}$ (MHz)
S1	1550.09	10869.93	0
S2	1550.17	10869.32	.61
S3	1550.26	10868.71	1.83
S4	1550.35	10868.10	3.66
S5	1550.44	10867.49	6.10

Appendix E

List of Publications

Journal papers

- **Ananthu Sebastian**, Stéphane Trebaol, Pascal Besnard; *Intracavity Brillouin gain characterization based on cavity ringdown spectroscopy* OSA Continuum, OSA Publishing, 2019, 2 (12), pp.3539-3545.

- **Ananthu Sebastian**, Irina V. Balakireva, Schadrac Fresnel, Stéphane Trebaol, and Pascal Besnard; *Relative intensity noise in a multi-Stokes Brillouin laser* Optics Express, Optical Society of America, 2018, 26 (26), pp.33700-33711.

Conferences contributions

- **Ananthu Sebastian**, Irina V Balakireva, Stéphane Trebaol, Pascal Besnard; *Relative intensity noise in a multi-Stokes Brillouin laser*, Workshop on OptoMechanics and Brillouin Scattering (WOMBAT). March 2019, Tel-Aviv, Israel.

- **Ananthu Sebastian**, Stéphane Trebaol, Pascal Besnard; *Intracavity Brillouin Gain Characterization* , International Topical Meeting on Microwave Photonics (MWP), Oct 2018, Toulouse, France

- **Ananthu Sebastian**, Schadrac Fresnel, Stéphane Trebaol, Frederic Ginovart, Pascal Besnard; *Improvement of noise reduction in fiber Brillouin lasers due to multi-Stokes operation*, SPIE Photonics Europe 2018, Apr 2018, Strasbourg, France.

- Frederic Ginovart, Schadrac Fresnel, **Ananthu Sebastian**, Stéphane Trebaol, Sophie La Rochelle, Pascal Besnard; *Phase-Variance reduction of high order Stokes lines in Brillouin fiber lasers*, Conference on Lasers and Electro-Optics Europe and European Quantum Electronics Conference 2017 (CLEO-Europe/EQEC 2017), Jun 2017, Munich, Germany.

- Schadrac Fresnel, **Ananthu Sebastian**, Stéphane Trebaol, Christelle Pareige, Frederic Ginovart, Pascal Besnard, Sophie La Rochelle; *Laser Brillouin Multi-Stokes pour la réduction du bruit de fréquence et d'intensité.* JNOG 2017, Limoges France.

Bibliography

[1] Stéphane Trebaol. *Etudes expérimentales des propriétés dispersives de structures photoniques à base de micro-résonateurs pour la réalisation de fonctions optiques.* PhD thesis, Université Rennes 1, 2010.

[2] Alphonse Rasoloniaina, Vincent Huet, Thi Kim Ngan Nguyen, Elodie Le Cren, Michel Mortier, Laurent Michely, Yannick Dumeige, and Patrice Féron. Controling the coupling properties of active ultrahigh-q wgm microcavities from undercoupling to selective amplification. *Scientific Reports*, 4:4023, 2014.

[3] Ryan O. Behunin, Nils T. Otterstrom, Peter T. Rakich, Sarat Gundavarapu, and Daniel J. Blumenthal. Fundamental noise dynamics in cascaded-order Brillouin lasers. *Physical Review A*, 98(2):1–17, 2018.

[4] William Loh, Scott B. Papp, and Scott A. Diddams. Noise and dynamics of stimulated-Brillouin-scattering microresonator lasers. *Physical Review A*, 91(5), 2015.

[5] Corning. Corning SMF-28 ultra optical fiber. Technical report, 2019.

[6] Léon Nicolas Brillouin. Diffusion de la lumière et des rayons X-par un corps transparent homogène. influence de l'agitation thermique. *Ann. Phys. (Paris)*, 17:88–122, 1922.

[7] E. Gross. Change of wave-length of light due to elastic heat waves at scattering in liquids. *Nature*, 126(3171):201–202, 1930.

[8] LI Mandelstam. Light scattering by inhomogeneous media. *Zh. Russ. Fiz-Khim. Ova*, 58:381, 1926.

[9] Theodore H Maiman. Stimulated optical radiation in ruby. *Nature*, 187(4736):493–494, 1960.

[10] RY Chiao, CH Townes, and BP Stoicheff. Stimulated brillouin scattering and coherent generation of intense hypersonic waves. *Physical Review Letters*, 12(21):592, 1964.

[11] E. P. Ippen and R. H. Stolen. Stimulated Brillouin scattering in optical fibers. *Applied Physics Letters*, 21(11):539–541, 1972.

[12] MF Ferreira, JF Rocha, and JL Pinto. Analysis of the gain and noise characteristics of fibre brillouin amplifiers. *Optical and quantum electronics*, 26(1):35–44, 1994.

[13] KO Hill, BS Kawasaki, and DC Johnson. CW Brillouin laser. *Applied Physics Letters*, 28(10):608–609, 1976.

[14] Wei Wei, Lilin Yi, Yves Jaouën, and Weisheng Hu. Bandwidth-tunable narrowband rectangular optical filter based on stimulated brillouin scattering in optical fiber. *Optics express*, 22(19):23249–23260, 2014.

[15] David Marpaung, Blair Morrison, Mattia Pagani, Ravi Pant, Duk-Yong Choi, Barry Luther-Davies, Steve J Madden, and Benjamin J Eggleton. Low-power, chip-based stimulated brillouin scattering microwave photonic filter with ultrahigh selectivity. *Optica*, 2(2):76–83, 2015.

[16] Xiaoyi Bao, Jabulani Dhliwayo, Nicol Heron, David J Webb, and David A Jackson. Experimental and theoretical studies on a distributed temperature sensor based on brillouin scattering. *Journal of Lightwave Technology*, 13(7):1340–1348, 1995.

[17] Xiaoyi Bao, M DeMerchant, A Brown, and T Bremner. Tensile and compressive strain measurement in the lab and field with the distributed brillouin scattering sensor. *Journal of Lightwave Technology*, 19(11):1698, 2001.

[18] Peter So. Brillouin bioimaging. *Nature Photonics*, 2(1):13–14, 2008.

[19] Giuliano Scarcelli and Seok Hyun Yun. Confocal brillouin microscopy for three-dimensional mechanical imaging. *Nature Photonics*, 2(1):39–43, 2008.

[20] Giuliano Scarcelli and Seok Hyun Yun. In vivo brillouin optical microscopy of the human eye. *Optics Express*, 20(8):9197–9202, 2012.

[21] Ravi Pant, Christopher G Poulton, Duk-Yong Choi, Hannah Mcfarlane, Samuel Hile, Enbang Li, Luc Thevenaz, Barry Luther-Davies, Stephen J Madden, and Benjamin J Eggleton. On-chip stimulated Brillouin scattering. *Optics Express*, 19:8285–8290, 2011.

[22] Flavien Gyger, Junqiu Liu, Fan Yang, Jijun He, Arslan S Raja, Rui Ning Wang, Sunil A Bhave, Tobias J Kippenberg, and Luc Thévenaz. Observation of stimulated Brillouin scattering in silicon nitride integrated waveguides. *Physical Review Letters*, 124(1):013902, 2020.

[23] Kazi S Abedin. Observation of strong stimulated Brillouin scattering in single-mode As_2Se_3 chalcogenide fiber. *Optics Express*, 13(25):10266–10271, 2005.

[24] Kazi S Abedin. Stimulated Brillouin scattering in single-mode tellurite glass fiber. *Optics Express*, 14(24):11766–11772, 2006.

[25] S P Smith, F Zarinetchi, and S Ezekiel. Narrow-linewidth stimulated Brillouin fiber laser and applications. *Optics Letters*, 16(6):393–395, 1991.

[26] François Mihelic. *Diffusion Brillouin stimulée dans les fibres optiques: amplification Brillouin large bande et laser Brillouin.* PhD thesis, Lille 1, 2008.

[27] V. Lecoeuche, P. Niay, M. Douay, P. Bernage, S. Randoux, and J. Zemmouri. Bragg grating based Brillouin fibre laser. *Optics Communications*, 177(1):303–306, 2000.

[28] Jae Chul Yong, Luc Thévenaz, and Byoung Yoon Kim. Brillouin fiber laser pumped by a DFB laser diode. *Journal of Lightwave Technology*, 21(2):546–554, 2003.

[29] Vasily V. Spirin, Patrice Mégret, and Andrei A. Fotiadi. Passively Stabilized Doubly-Resonant Brillouin Fiber Lasers. *Fiber Laser*, (January 2017), 2016.

[30] Gregory J Cowle and Dmitrii Yu Stepanov. Hybrid Brillouin/erbium fiber laser. *Optics Letters*, 21(16):1250–1252, 1996.

[31] Yoshihiro Honda, Wataru Yoshiki, Tomohiro Tetsumoto, Shun Fujii, Kentaro Furusawa, Norihiko Sekine, and Takasumi Tanabe. Brillouin lasing in coupled silica toroid microcavities. *Applied Physics Letters*, 112(20), 2018.

[32] Matthew Puckett, Debapam Bose, Karl Nelson, and Daniel J Blumenthal. Higher order cascaded SBS suppression using gratings in a photonic integrated ring resonator laser. In *CLEO: Science and Innovations*, pages SM4O–1. Optical Society of America, 2019.

[33] Kenny Hey Tow. *Laser Brillouin à fibre microstructurée en verre de chalcogénure*. PhD thesis, Université Rennes 1, 2013.

[34] Schadrac Fresnel. *Lasers á fibre Brillouin multi-stokes : cohérence et caractérisation en bruit*. PhD thesis, Université Rennes 1 / Université Laval (Québec, Canada), 2017.

[35] Frank E Goodwin. A review of operational laser communication systems. *Proceedings of the IEEE*, 58(10):1746–1752, 1970.

[36] Farhan S Ujager, SMH Zaidi, and Usman Younis. A review of semiconductor lasers for optical communications. In *7th International Symposium on High-capacity Optical Networks and Enabling Technologies*, pages 107–111. IEEE, 2010.

[37] Christine Spiegelberg, Jihong Geng, Yongdan Hu, Yushi Kaneda, Shibin Jiang, and N Peyghambarian. Low-noise narrow-linewidth fiber laser at 1550 nm. *Journal of Lightwave Technology*, 22(1):57–62, 2004.

[38] RJ Rafac, BC Young, James A Beall, Wayne M Itano, David J Wineland, and JC Bergquist. Sub-dekahertz ultraviolet spectroscopy of 199 Hg+. *Physical Review Letters*, 85(12):2462, 2000.

[39] Nathan Hinkley, Jeff A Sherman, Nathaniel B Phillips, Macro Schioppo, Nathan D Lemke, Kyle Beloy, Marco Pizzocaro, Christopher W Oates, and Andrew D Ludlow. An atomic clock with 10^{-18} instability. *Science*, 341(6151):1215–1218, 2013.

[40] BJ Bloom, TL Nicholson, JR Williams, SL Campbell, M Bishof, X Zhang, W Zhang, SL Bromley, and J Ye. An optical lattice clock with accuracy and stability at the 10^{-18} level. *Nature*, 506(7486):71–75, 2014.

[41] Xiaopeng Xie, Romain Bouchand, Daniele Nicolodi, Michel Lours, Christophe Alexandre, and Yann Le Coq. Phase noise characterization of sub-hertz linewidth lasers via digital cross correlation. *Optics Letters*, 42(7):1217–1220, 2017.

[42] Pierre Grüning, Amine Chaouche-Ramdane, Karim Manamanni, Thinhinane Aoudjit, Vincent Roncin, and Frédéric Du-Burck. All-fiber ring-cavity for frequency stability transfer at 1.55 μm. *Applied Optics*, 58(6):1502–1507, 2019.

[43] M.C Amann. Phase noise limited resolution of coherent LIDAR using widely tunable laser diodes. *Electronics Letters*, 28(18):1694–1696, 1992.

[44] Tara M Fortier, Matthew S Kirchner, F Quinlan, J Taylor, JC Bergquist, T Rosenband, N Lemke, A Ludlow, Y Jiang, CW Oates, et al. Generation of ultrastable microwaves via optical frequency division. *Nature Photonics*, 5(7):425, 2011.

[45] James Anderson Barnes. *Models for the interpretation of frequency stability measurements*, volume 13. Department of Commerce, National Bureau of Standards, Time and Frequency , 1976.

[46] Jacques Rutman. Characterization of phase and frequency instabilities in precision frequency sources: Fifteen years of progress. *Proceedings of the IEEE*, 66(9):1048–1075, 1978.

[47] Charles Henry. Theory of the linewidth of semiconductor lasers. *IEEE Journal of Quantum Electronics*, 18(2):259–264, 1982.

[48] Enrico Rubiola. *Phase noise and frequency stability in oscillators*. Cambridge University Press, 2009.

[49] Fritz Riehle. *Frequency standards: basics and applications*. John Wiley & Sons, 2006.

[50] Mohamed Omar Sahni. *Contributioná l'étude de techniques pour l'affinement spectral de lasers : application aux diodes á blocage de modes destinées aux télécommunications optiques cohérentes*. PhD thesis, Universite de Rennes 1, 2018.

[51] FN Hooge, TGM Kleinpenning, and LKJ Vandamme. Experimental studies on 1/f noise. *Reports on progress in Physics*, 44(5):479, 1981.

[52] AL McWhorter. 1/f noise and germanium surface properties, semiconductor surface physics. *Philadelphia: University of Pennsylvania Press*, 1057:207, 1957.

[53] Bruno Pellegrini. Diffusion, mobility fluctuation, and island models of flicker noise. *Physical Review B*, 26(4):1791, 1982.

[54] Julien Poette, Stéphane Blin, G Brochu, Laurent Bramerie, R Slavik, J-C Simon, Sophie LaRochelle, and Pascal Besnard. Relative intensity noise of multiwavelength fibre laser. *Electronics Letters*, 40(12):724–726, 2004.

[55] Irène Joindot. *Bruit relatif d'intensité des lasers à semiconducteur*. PhD thesis, Montpellier 2, 1990.

[56] Arthur L Schawlow and Charles H Townes. Infrared and optical masers. *Physical Review*, 112(6):1940, 1958.

[57] Gianni Di Domenico, Stephane Schilt, and Pierre Thomann. Simple approach to the relation between laser frequency noise and laser line shape. *Applied Optics*, 49:4801–4807, 2010.

[58] G. M. Stéphan, T. T. Tam, S. Blin, P. Besnard, and M. Têtu. Laser line shape and spectral density of frequency noise. *Physical Review A*, 71(4):1–9, 2005.

[59] DS Elliott, Rajarshi Roy, and SJ Smith. Extracavity laser band-shape and bandwidth modification. *Physical Review A*, 26(1):12, 1982.

[60] Max Schiemangk, Stefan Spießberger, Andreas Wicht, Götz Erbert, Günther Tränkle, and Achim Peters. Accurate frequency noise measurement of free-running lasers. *Applied Optics*, 53(30):7138–7143, 2014.

[61] Motonobu Kourogi and Motoichi Ohtsu. Novel optical frequency discriminator for FM noise reduction of semiconductor lasers. *Optics Communications*, 81(3-4):204–208, 1991.

[62] F. V. Kowalski J. Hough G. M. Ford A. J. Munley H. Ward R. W. P. Drever, J. L. Hall. Laser phase and frequency stabilization using an optical resonator. *Applied Physics B*, 31(2):97–105, 1983.

[63] P Tremblay and R Ouellet. Frequency response of a Fabry-Perot interferometer used as a frequency discriminator (semiconductor laser application). In *Conference on Precision Electromagnetic Measurements*, pages 252–253. IEEE, 1990.

[64] Wojciech Gawlik and Jerzy Zachorowski. Stabilization of diode-laser frequency to atomic transitions. *Optica Applicata*, 34(4):607–618, 2004.

[65] Stefano Camatel and Valter Ferrero. Narrow linewidth CW laser phase noise characterization methods for coherent transmission system applications. *Journal of Lightwave Technology*, 26(17):3048–3055, 2008.

[66] Dan Xu, Fei Yang, Dijun Chen, Fang Wei, Haiwen Cai, Zujie Fang, and Ronghui Qu. Laser phase and frequency noise measurement by Michelson interferometer composed of a 3× 3 optical fiber coupler. *Optics Express*, 23(17):22386–22393, 2015.

[67] Olivier Llopis, Pierre-Henri Merrer, Houda Brahimi, Khaldoun Saleh, and Pierre Lacroix. Phase noise measurement of a narrow linewidth CW laser using delay line approaches. *Optics Letters*, 36(14):2713–2715, 2011.

[68] Takanori Okoshi, Kazuro Kikuchi, and A Nakayama. Novel method for high resolution measurement of laser output spectrum. *Electronics Letters*, 16(16):630–631, 1980.

[69] Olivier Llopis, Zeina Abdallah, Vincent Auroux, and Arnaud Fernandez. High spectral purity laser characterization with a self-heterodyne frequency discriminator. In *2015 Joint Conference of the IEEE International Frequency Control Symposium & the European Frequency and Time Forum*, pages 602–605. IEEE, 2015.

[70] Timothy Day, Eric K Gustafson, and Robert L Byer. Sub-hertz relative frequency stabilization of two-diode laser-pumped Nd:YAG lasers locked to a Fabry-Perot interferometer. *IEEE Journal of Quantum Electronics*, 28(4):1106–1117, 1992.

[71] Warren Nagourney. *Quantum electronics for atomic physics and telecommunication*. OUP Oxford, 2014.

[72] Richard W Fox, Chris W Oates, and Leo W Hollberg. 1. Stabilizing diode lasers to high-finesse cavities. In *Experimental methods in the physical sciences*, volume 40, pages 1–46. Elsevier, 2003.

[73] Wojciech Lewoczko-Adamczyk, Christoph Pyrlik, Johannes Häger, Sven Schwertfeger, Andreas Wicht, Achim Peters, Götz Erbert, and Günther Tränkle. Ultra-

narrow linewidth DFB-laser with optical feedback from a monolithic confocal Fabry-Perot cavity. *Optics Express*, 23(8):9705–9709, 2015.

[74] Fang Wei, Fei Yang, Xi Zhang, Dan Xu, Meng Ding, Li Zhang, Dijun Chen, Haiwen Cai, Zujie Fang, and Gu Xijia. Subkilohertz linewidth reduction of a DFB diode laser using self-injection locking with a fiber Bragg grating Fabry-Perot cavity. *Optics Express*, 24(15):17406–17415, 2016.

[75] Eric D. Black. An introduction to Pound–Drever–Hall laser frequency stabilization. *American Journal of Physics*, 69(1):79–87, 2001.

[76] M Nickerson. A review of Pound-Drever-Hall laser frequency locking. *JILA, University of Colorado and NIST*, 2019.

[77] Govind P Agrawal. *Nonlinear fiber optics*. Academic press, 5th edition, 2013.

[78] Robert W Boyd. *Nonlinear optics*. Academic press, 2003.

[79] Peter D Dragic. Brillouin gain reduction Via B_2O_3 doping. *Journal of Lightwave Technology*, 29(7):967–973, 2011.

[80] M Nikles, L Thevenaz, and P A Robert. Brillouin gain spectrum characterization in single-mode optical fibers. *Journal of Lightwave Technology*, 15:1842–1851, 1997.

[81] Rogers H Stolen. Polarization effects in fiber Raman and Billouin lasers. *IEEE Journal of Quantum Electronics*, 15:1157–1160, 1979.

[82] M Oskar Van Deventer and Andre J Boot. Polarization properties of stimulated Brillouin scattering in single-mode fibers. *Journal of Lightwave Technology*, 12(4):585–590, 1994.

[83] P Bayvel and P M Radmore. Solutions of the SBS equations in single mode optical fibres and implications for fibre transmission systems. *Electronics Letters*, 26(7):434–436, 1990.

[84] Jean-Charles Beugnot, Thibaut Sylvestre, Dario Alasia, Hervé Maillotte, Vincent Laude, A Monteville, Laurent Provino, Nicholas Traynor, S Foaleng Mafang, and Luc Thévenaz. Complete experimental characterization of stimulated Brillouin scattering in photonic crystal fiber. *Optics Express*, 15(23):15517–15522, 2007.

[85] A L Gaeta and R W Boyd. Stochastic Dynamics of Stimulated Brillouin Scattering in an Optical Fiber. *Physical Review A*, 44(5):3205–3209, 1991.

[86] Andrey Kobyakov, Michael Sauer, and Dipak Chowdhury. Stimulated Brillouin scattering in optical fibers. *Advances in Optics and Photonics*, 2(1):1, 2010.

[87] Marc Niklès, Philippe Alain Robert, and Others. *La diffusion Brillouin dans les fibres optiques : lètude et application aux capteurs distribulès*. PhD thesis, EPFL, 1997.

[88] Yohann Léguillon, Kenny Hey Tow, Alain Mugnier, David Pureur, Pascal Besnard, and Martine Doisy. Effets d'une faible contre-réaction optique sur des lasers à fibre DFB pour applications capteurs. In *Optique Marseille 2011 - 30è Journées Nationales d'Optique Guidée (JNOG 2011)*, Optique Marseille 2011 - recueil des communications JNOG, pages 257–259, Marseille, France, July 2011.

[89] Birgit Stiller. *Brillouin scattering in photonic crystal fiber: from fundamentals to fiber optic sensors*. PhD thesis, SPIM, Ecole Doctorale and Photonique, Spécialité Optique and, 2011.

[90] Catalin Florea, Mark Bashkansky, Zachary Dutton, Jasbinder Sanghera, Paul Pureza, and Ishwar Don Aggarwal. Stimulated Brillouin scattering in single-mode As_2S_3 andAs_2Se_3 chalcogenide fibers. *Optics Express*, 14(25):12063–12070, 2006.

[91] Kwang Yong Song, Kazi S Abedin, Kazuo Hotate, Miguel González Herráez, and Luc Thévenaz. Highly efficient Brillouin slow and fast light using As_2Se_3 chalcogenide fiber. *Optics Express*, 14(13):5860–5865, 2006.

[92] N Shibata, R G Waarts, and R P Braun. Brillouin-gain spectra for single-mode fibers having pure-silica, GeO_2-doped, and P_2O_5-doped cores. *Optics Letters*, 12(4):269–271, 1987.

[93] Robert W Tkach, Andrew R Chraplyvy, and RM Derosier. Spontaneous Brillouin scattering for single-mode optical fiber characterization. In *Optical Fiber Communication Conference*, page WH4. Optical Society of America, 1987.

[94] Kazi S Abedin. Stimulated Brillouin scattering in single-mode tellurite glass fiber. *Optics Express*, 14(24):11766–11772, 2006.

[95] Yosuke Mizuno, Zuyuan He, and Kazuo Hotate. Dependence of the Brillouin frequency shift on temperature in a tellurite glass fiber and a bismuth-oxide highly-nonlinear fiber. *Applied Physics Express*, 2(11):112402, 2009.

[96] Yosuke Mizuno and Kentaro Nakamura. Brillouin Scattering in polymer optical fibers: Fundamental properties and potential use in sensors. *Polymers*, 3(2):886–898, 2011.

[97] Yannick Dumeige, Stéphane Trebaol, Laura Ghis, Thi Kim, Ngân Nguyên, Hervé Tavernier, and Patrice Féron. Determination of coupling regime of high- Q amplifiers. *Journal of the Optical Society of America B*, 25(12):2073–2080, 2008.

[98] Stéphane Trebaol, Yannick Dumeige, and Patrice Féron. Ringing phenomenon in coupled cavities: Application to modal coupling in whispering-gallery-mode resonators. *Physical Review A*, 81(4), 2010.

[99] Alphonse Rasoloniaina, Vincent Huet, Monique Thual, Stéphane Balac, Patrice Féron, and Yannick Dumeige. Analysis of third-order nonlinearity effects in very high-Q WGM resonator cavity ringdown spectroscopy. *Journal of the Optical Society of America B*, 32(3):370–378, 2015.

[100] Anatoliy A. Savchenkov, Andrey B. Matsko, Makan Mohageg, and Lute Maleki. Ringdown spectroscopy of stimulated Raman scattering in a whispering gallery mode resonator. *Optics Letters*, 32(5):497–499, Mar 2007.

[101] G Nunzi Conti, S Berneschi, F Cosi, S Pelli, S Soria, GC Righini, M Dispenza, and A Secchi. Planar coupling to high-Q lithium niobate disk resonators. *Optics Express*, 19(4):3651–3656, 2011.

[102] Rémi Henriet, Guoping Lin, Aurélien Coillet, Maxime Jacquot, Luca Furfaro, Laurent Larger, and Yanne K Chembo. Kerr optical frequency comb generation in strontium fluoride whispering-gallery mode resonators with billion quality factor. *Optics Letters*, 40(7):1567–1570, 2015.

[103] Ananthu Sebastian, Stéphane Trebaol, and Pascal Besnard. Intracavity brillouin gain characterization based on cavity ringdown spectroscopy. *OSA Continuum*, 2(12):3539–3545, 2019.

[104] Amnon Yariv. Coupled-mode theory for guided-wave optics. *IEEE Journal of Quantum Electronics*, 9(9):919–933, 1973.

[105] Amnon Yariv. Universal relations for coupling of optical power between microresonators and dielectric waveguides. *Electronics Letters*, 36(4):321–322, 2000.

[106] Zacharias K Ioannidis, PM Radmore, and IP Giles. Dynamic response of an all-fiber ring resonator. *Optics Letters*, 13(5):422–424, 1988.

[107] HJ Schmitt and H Zimmer. Fast sweep measurements of relaxation times in superconducting cavities (correspondence). *IEEE Transactions on Microwave Theory and Techniques*, 14(4):206–207, 1966.

[108] Jérôme Poirson, Fabien Bretenaker, Marc Vallet, and Albert Le Floch. Analytical and experimental study of ringing effects in a Fabry–Perot cavity. Application to the measurement of high finesses. *Journal of the Optical Society of America B*, 14(11):2811–2817, 1997.

[109] K Ogusu, H P Li, and M Kitao. Brillouin-gain coefficients of chalcogenide glasses. *Journal of the Optical Society of America B*, 21:1302–1304, 2004.

[110] N. Lagakos, J. A. Bucaro, and R. Hughes. Acoustic sensitivity predictions of single-mode optical fibers using Brillouin scattering. *Applied Optics*, 19(21):3668, 1980.

[111] K. O. Hill, D. C. Johnson, and B. S. Kawasaki. CW generation of multiple Stokes and anti-Stokes Brillouin-shifted frequencies. *Applied Physics Letters*, 29(3):185–187, 1976.

[112] K O Hill, B S Kawasaki, and D C Johnson. CW Brillouin laser. *Applied Physics Letters*, 28(10):608–609, 1976.

[113] Donald R Ponikvar and Shaoul Ezekiel. Stabilized single-frequency stimulated Brillouin fiber ring laser. *Optics Letters*, 6(8):398–400, 1981.

[114] L F Stokes, M Chodorow, and H J Shaw. All-fiber stimulated Brillouin ring laser with submilliwatt pump threshold. *Optics Letters*, 7(10):509–511, 1982.

[115] P Bayvel and I P Giles. Evaluation of performance parameters of single-mode all-fiber Brillouin ring lasers. *Optics Letters*, 14(11):581–3, 1989.

[116] P Nicati BY Kim HJ Shaw. K Toyama, S Huang. Generation of multiple Stokes waves in a Brillouin fiber ring laser. In *Optical Fiber Sensors Conference*, 1993.

[117] P.A Nicati, K Toyama, S Huang, and Herbert J Shaw. Temperature effects in a Brillouin fiber ring laser. *Optics Letters*, 18(24):2123–2125, 1993.

[118] P. A. Nicati, K. Toyama, S. Huang, and H. J. Shaw. Frequency Pulling in a Brillouin Fiber Ring Laser. *IEEE Photonics Technology Letters*, 6(7):801–803, 1994.

[119] P.A. Nicati, K. Toyama, and H.J. Shaw. Frequency stability of a Brillouin fiber ring laser. *Journal of Lightwave Technology*, 13(7):1445–1451, 1995.

[120] S. Randoux, V. Lecoeuche, B. Ségard, and J. Zemmouri. Dynamical analysis of Brillouin fiber lasers: An experimental approach. *Physical Review A*, 51(6):4345–4348, 1995.

[121] V. Lecoeuche, S. Randoux, B. Ségard, and J. Zemmouri. Dynamics of a Brillouin fiber ring laser: Off-resonant case. *Physical Review A*, 53(4):2822–2828, 1996.

[122] Carlos Montes, Derradji Bahloul, Isabelle Bongrand, Jean Botineau, Gérard Cheval, Abdellatif Mamhoud, Eric Picholle, and Antonio Picozzi. Self-pulsing and dynamic bistability in cw-pumped Brillouin fiber ring lasers. *Journal of the Optical Society of America B*, 16(6):932–951, 1999.

[123] Alexis Debut, Stéphane Randoux, and Jaouad Zemmouri. Linewidth narrowing in Brillouin lasers: Theoretical analysis. *Physical Review A*, 62(2):1–4, 2000.

[124] Alexis Debut, Stéphane Randoux, and Jaouad Zemmouri. Experimental and theoretical study of linewidth narrowing in Brillouin fiber ring lasers. *Journal of the Optical Society of America B*, 18(4):556–567, 2001.

[125] L Stepien, S Randoux, and J Zemmouri. Intensity noise in Brillouin fiber ring lasers. *Journal of the Optical Society of America B*, 19(5):1055–1066, 2002.

[126] Jihong Geng, Sean Staines, Zuolan Wang, Jie Zong, Mike Blake, and Shibin Jiang. Highly stable low-noise Brillouin fiber laser with ultranarrow spectral linewidth. *IEEE Photonics Technology Letters*, 18(17):1813–1815, 2006.

[127] Jihong Geng and Shibin Jiang. Pump-to-Stokes transfer of relative intensity noise in Brillouin fiber ring lasers. *OFC/NFOEC 2007 - Optical Fiber Communication and the National Fiber Optic Engineers Conference 2007*, 32(1):2006–2008, 2007.

[128] Jihong Geng and Shibin Jiang. Pump-to-Stokes transfer of relative Intensity noise in Brillouin fiber ring lasers. *Optics Letters*, 32:11–13, 2007.

[129] Mo Chen, Zhou Meng, Xiaobo Tu, and Huijuan Zhou. Low-noise, single-frequency, single-polarization Brillouin/erbium fiber laser. *Optics Letters*, 38(12):2041–3, 2013.

[130] Mo Chen, Zhou Meng, Xiaobo Tu, and Yichi Zhang. Fast-tuning, low-noise, compact Brillouin/erbium fiber laser. *Optics Letters*, 39(3):689–92, 2014.

[131] Mo Chen, Chenyu Wang, Jianfei Wang, Hong Luo, and Zhou Meng. 53-dB phase noise suppression and Hz-range linewidth emission in compact Brillouin/erbium fiber laser. *Optics Express*, 25(16):19216, 2017.

[132] Chaodu Shi, Quan Sheng, Shijie Fu, Shuai Sun, Junxiang Zhang, Wei Shi, and Jianquan Yao. Power scaling and spectral linewidth suppression of hybrid Brillouin/thulium fiber laser. *Optics Express*, 28(3):2948–2955, 2020.

[133] Birgit Stiller and Thibaut Sylvestre. Observation of acoustically induced modulation instability in a Brillouin photonic crystal fiber laser. *Optics Letters*, 38(9):1570–1572, 2013.

[134] Guanshi Qin, Hideyuki Sotobayashi, Masahiro Tsuchiya, Atsushi Mori, Takenobu Suzuki, and Yasutake Ohishi. Stimulated Brillouin scattering in a single-mode tellurite fiber for amplification, lasing, and slow light generation. *Journal of Lightwave Technology*, 26(5):492–498, 2008.

[135] Dinghuan Deng, Weiqing Gao, Tonglei Cheng, Edmund E Samuel, Takenobu Suzuki, and Yasutake Ohishi. Highly efficient fast light generation in a tellurite fiber embedded in Brillouin laser ring cavity. *IEEE Photonics Technology Letters*, 26(17):1758–1761, 2014.

[136] Moïse Deroh, Bertrand Kibler, Arnaud Lemiere, F Desevedavy, F Smektala, Hervé Maillotte, Thibaut Sylvestre, and J-C Beugnot. 2-μm Brillouin laser based on infrared nonlinear glass fibers. *Applied Optics*, 58(23):6365–6369, 2019.

[137] Kazi S Abedin. Brillouin amplification and lasing in a single-mode As_2Se_3 chalcogenide fiber. *Optics Letters*, 31(11):1615–1617, 2006.

[138] Kenny Hey Tow, Yohann Léguillon, Schadrac Fresnel, Pascal Besnard, Laurent Brilland, David Méchin, Denis Trégoat, Johann Troles, and Perrine Toupin. Linewidth-narrowing and intensity noise reduction of the 2nd order Stokes component of a low threshold Brillouin laser made of $Ge_{10}As_{22}Se_{68}$ chalcogenide fiber. *Optics Express*, 20(26):B104–B109, 2012.

[139] Kenny Hey Tow, Yohann Leguillon, Schadrac Fresnel, Pascal Besnard, Laurent Brilland, David Méchin, Perrine Toupin, and Johann Troles. Toward more coherent sources using a microstructured chalcogenide Brillouin fiber laser. *Photonics Technology Letters, IEEE*, 25(3):238–241, 2013.

[140] E Garmire and CH Townes. Stimulated Brillouin scattering in liquids[1]. *Applied Physics Letters*, 5(4):84–86, 1964.

[141] EE Hagenlocker and WG Rado. Stimulated Brillouin and Raman scattering in gases. *Applied Physics Letters*, 7(9):236–238, 1965.

[142] K Kieu, D Churin, L Schneebeli, Robert A Norwood, and N Peyghambarian. Brillouin lasing in integrated liquid-core optical fibers. *Optics Letters*, 38(4):543–545, 2013.

[143] Fan Yang, Flavien Gyger, and Luc Thévenaz. Giant Brillouin amplification in gas using hollow-core waveguides. *arXiv*, pages arXiv–1911, 2019.

[144] Matthew Tomes and Tal Carmon. Photonic micro-electromechanical systems vibrating at X-band (11-GHz) rates. *Physical Review Letters*, 102(11):113601, 2009.

[145] Ivan S. Grudinin, Andrey B. Matsko, and Lute Maleki. Brillouin lasing with a CaF_2 whispering gallery mode resonator. *Physical Review Letters*, 102(4):1–4, 2009.

[146] Hansuek Lee, Tong Chen, Jiang Li, Ki Youl Yang, Seokmin Jeon, Oskar Painter, and Kerry J. Vahala. Chemically etched ultrahigh-Q wedge-resonator on a silicon chip. *Nature Photonics*, 6(6):369–373, 2012.

[147] Jiang Li, Hansuek Lee, Tong Chen, and Kerry J. Vahala. Characterization of a high coherence, Brillouin microcavity laser on silicon. *Optics Express*, 20(18):20170, 2012.

[148] Jiang Li, Hansuek Lee, and Kerry J Vahala. Microwave synthesizer using an on-chip Brillouin oscillator. *Nature communications*, 4(1):1–7, 2013.

[149] Jiang Li, Myoung-Gyun Suh, and Kerry Vahala. Microresonator Brillouin gyroscope. *Optica*, 4(3):346–348, 2017.

[150] Yu-Hung Lai, Yu-Kun Lu, Myoung-Gyun Suh, and Kerry Vahala. Enhanced sensitivity operation of an optical gyroscope near an exceptional point. *arXiv preprint arXiv:1901.08217*, 2019.

[151] Jiang Li, Hansuek Lee, and Kerry J. Vahala. Low-noise Brillouin laser on a chip at 1064 nm. *Optics Letters*, 39(2):287, 2014.

[152] Changlei Guo, Kaijun Che, Zhiping Cai, Shuai Liu, Guoqiang Gu, Chengxu Chu, Pan Zhang, Hongyan Fu, Zhengqian Luo, and Huiying Xu. Ultralow-threshold cascaded Brillouin microlaser for tunable microwave generation. *Optics Letters*, 40(21):4971–4974, 2015.

[153] Kaijun Che, Deyu Tang, Changyan Ren, Huiying Xu, Lujian Chen, Chaoyuan Jin, and Zhiping Cai. Thermal Characteristics of Brillouin Microsphere Lasers. *IEEE Journal of Quantum Electronics*, 54(3), 2018.

[154] William Loh, Joe Becker, Daniel C. Cole, Aurelien Coillet, Fred N. Baynes, Scott B. Papp, and Scott A. Diddams. A microrod-resonator Brillouin laser with 240 Hz absolute linewidth. *New Journal of Physics*, 18(4):0, 2016.

[155] Pascal Del'Haye, Scott A Diddams, and Scott B Papp. Laser-machined ultra-high-Q microrod resonators for nonlinear optics. *Applied Physics Letters*, 102(22):221119, 2013.

[156] Motoki Asano, Yuki Takeuchi, Sahin Kaya Ozdemir, Rikizo Ikuta, Lan Yang, Nobuyuki Imoto, and Takashi Yamamoto. Stimulated Brillouin scattering and Brillouin-coupled four-wave-mixing in a silica microbottle resonator. *Optics Express*, 24(11):12082–12092, 2016.

[157] Qijing Lu, Sheng Liu, Xiang Wu, Liying Liu, and Lei Xu. Stimulated Brillouin laser and frequency comb generation in high-Q microbubble resonators. *Optics Letters*, 41(8):1736–1739, 2016.

[158] Guoping Lin, Souleymane Diallo, Khaldoun Saleh, Romain Martinenghi, Jean Charles Beugnot, Thibaut Sylvestre, and Yanne K. Chembo. Cascaded Brillouin lasing in monolithic barium fluoride whispering gallery mode resonators. *Applied Physics Letters*, 105(23):6–10, 2014.

[159] Guoping Lin, Souleymane Diallo, John M. Dudley, and Yanne K. Chembo. Universal nonlinear scattering in ultra-high Q whispering gallery-mode resonators. *Optics Express*, 24(13):14880, 2016.

[160] Changlei Guo, Kaijun Che, Pan Zhang, Jinshu Wu, Yantang Huang, Huiying Xu, and Zhiping Cai. Low-threshold stimulated Brillouin scattering in high-Q whispering gallery mode tellurite microspheres. *Optics Express*, 23(25):32261–32266, 2015.

[161] A. Giorgini, S. Avino, P. Malara, P. De Natale, M. Yannai, T. Carmon, and G. Gagliardi. Stimulated Brillouin Cavity Optomechanics in Liquid Droplets. *Physical Review Letters*, 120(7):073902, 2018.

[162] Irina V. Kabakova, Ravi Pant, Duk-Yong Choi, Sukhanta Debbarma, Barry Luther-Davies, Stephen J. Madden, and Benjamin J. Eggleton. Narrow linewidth Brillouin laser based on chalcogenide photonic chip. *Optics Letters*, 38(17):3208, 2013.

[163] Sarat Gundavarapu, Grant M. Brodnik, Matthew Puckett, Taran Huffman, Debapam Bose, Ryan Behunin, Jianfeng Wu, Tiequn Qiu, Cátia Pinho, Nitesh Chauhan, Jim Nohava, Peter T. Rakich, Karl D. Nelson, Mary Salit, and Daniel J. Blumenthal. Sub-hertz fundamental linewidth photonic integrated Brillouin laser. *Nature Photonics*, 2018.

[164] Michael L Gorodetsky and Ivan S Grudinin. Fundamental thermal fluctuations in microspheres. *Journal of the Optical Society of America B*, 21(4):697–705, 2004.

[165] William Loh, Siva Yegnanarayanan, Frederick O'Donnell, and Paul W. Juodawlkis. Ultra-narrow linewidth Brillouin laser with nanokelvin temperature self-referencing. *Optica*, 6(2):152, 2019.

[166] William Loh, Jules Stuart, David Reens, Colin D Bruzewicz, Danielle Braje, John Chiaverini, Paul W Juodawlkis, Jeremy M Sage, and Robert McConnell. A Brillouin Laser Optical Atomic Clock. *arXiv preprint arXiv:2001.06429*, 2020.

[167] Kenny Hey Tow, Yohann Leguillon, Pascal Besnard, Laurent Brilland, Johann Troles, Perrine Toupin, David Mechin, Denis Tregoat, and Stephanie Molin. Relative intensity noise and frequency noise of a compact Brillouin laser made of $As_{38}Se_{62}$ suspended-core chalcogenide fiber. *Optics Letters*, 37:1157–1159, 2012.

[168] Küng Alain. *L'émission laser par diffusion Brillouin stimulée dans les fibres optiques*. PhD thesis, EPFL, 1997.

[169] François Mihélic, Denis Bacquet, Jaouad Zemmouri, and Pascal Szriftgiser. Ultra-high resolution spectral analysis based on a Brillouin fiber laser. *Optics Letters*, 35(3):432–434, 2010.

[170] Gwennaël Danion, Ludovic Frein, Denis Bacquet, Grégoire Pillet, Stéphanie Molin, Loïc Morvan, Guillaume Ducournau, Marc Vallet, Pascal Szriftgiser, and Mehdi Alouini. Mode-hopping suppression in long Brillouin fiber laser with non-resonant pumping. *Optics Letters*, 41(10):2362–2365, 2016.

[171] Gilles Bailly, Olivier Llopis, and Arnaud Fernandez. High spectral purity optical source stabilized on a fiber ring resonator. *IEEE Photonics Technology Letters*, 32(5):255–258, 2020.

[172] Thomas FS Büttner, Irina V Kabakova, Darren D Hudson, Ravi Pant, Enbang Li, and Benjamin J Eggleton. Multi-wavelength gratings formed via cascaded stimulated Brillouin scattering. *Optics Express*, 20(24):26434–26440, 2012.

[173] Heedeuk Shin, Wenjun Qiu, Robert Jarecki, Jonathan A Cox, Roy H Olsson III, Andrew Starbuck, Zheng Wang, and Peter T Rakich. Tailorable stimulated Brillouin scattering in nanoscale silicon waveguides. *Nature communications*, 4, 2013.

[174] Ananthu Sebastian, Irina V. Balakireva, Schadrac Fresnel, Stéphane Trebaol, and Pascal Besnard. Relative intensity noise in a multi-Stokes Brillouin laser. *Optics Express*, 26(26):33700–33711, Dec 2018.

[175] M Weel and A Kumarakrishnan. Laser-frequency stabilization using a lock-in amplifier. *Canadian Journal of Physics*, 80(12):1449–1458, 2002.

[176] H. Haus. *Waves and fields in optoelectronics.* Prentice-Hall, 1984.

[177] Frédéric Ginovart, Schadrac Fresnel, Ananthu Sebastian, Stephane Trebaol, Sophie LaRochelle, and Pascal Besnard. Phase variance reduction of high order Stokes lines in Brillouin fiber lasers. In *Conference on Lasers and Electro-Optics Europe and European Quantum Electronics Conference 2017 (CLEO-Europe/EQEC 2017)*, 2017 Conference on Lasers and Electro-Optics Europe & European Quantum Electronics Conference (CLEO/Europe-EQEC), Munich, Germany, June 2017. IEEE.

[178] Sebastian Ananthu, Schadrac Fresnel, Stéphane Trebaol, Frédéric Ginovart, and Pascal Besnard. Improvement of noise reduction in fiber Brillouin lasers due to multi-Stokes operation. In Proc.SPIE, editor, *Conference: Fiber Lasers and Glass Photonics: Materials through Applications*, volume 10683, 2018.

[179] Stephanie Molin, Ghaya Baili, Mehdi Alouini, Daniel Dolfi, and Jean-Pierre Huignard. Experimental investigation of relative intensity noise in Brillouin fiber ring lasers for microwave photonics applications. *Optics Letters*, 33:1681–1683, 2008.

[180] Klaus Petermann. *Laser diode modulation and noise*, volume 3. Springer Science & Business Media, 2012.

[181] William Loh, Matthew T Hummon, Holly F Leopardi, Tara M Fortier, Frank Quinlan, John Kitching, Scott B Papp, and Scott a Diddams. Microresonator Brillouin laser stabilization using a microfabricated Rubidium cell. *arXiv*, 332(6029):1214–1217, 2016.

[182] Sun-Jong Kim, Jung-Hee Han, Jae-Seung Lee, and Chang-Soo Park. Intensity noise suppression in spectrum-sliced incoherent light communication systems using a gain-saturated semiconductor optical amplifier. *IEEE Photonics Technology Letters*, 11(8):1042–1044, 1999.

[183] Kenji Sato and Hiromu Toba. Reduction of mode partition noise by using semiconductor optical amplifiers. *IEEE Journal of Selected Topics in Quantum Electronics*, 7(2):328–333, 2001.

[184] Gwennaël Danion, François Bondu, Goulc'hen Loas, and Mehdi Alouini. GHz bandwidth noise eater hybrid optical amplifier: design guidelines. *Optics Letters*, 39(14):4239–4242, Jul 2014.

[185] Govind P Agrawal and Niloy K Dutta. *Semiconductor lasers*. Springer Science & Business Media, 2013.

[186] William Loh, Adam A. S. Green, Fred N. Baynes, Daniel C. Cole, Franklyn J. Quinlan, Hansuek Lee, Kerry J. Vahala, Scott B. Papp, and Scott A. Diddams. Dual-microcavity narrow-linewidth Brillouin laser. *Optica*, 2(3):225, 2015.

[187] Richard G Smith. Optical power handling capacity of low loss optical fibers as determined by stimulated Raman and Brillouin scattering. *Applied Optics*, 11(11):2489–2494, 1972.

Dynamique de bruit dans les lasers Brillouin multi-Stokes

La diffusion Brillouin stimulée (SBS) est un processus d'interaction cohérent, pour lequel la lumière est diffusée à partir des ondes acoustiques générées optiquement. C'est un outil puissant pour le traitement des micro-ondes et des signaux optiques, la détection distribuée spatialement et la spectroscopie. Les lasers Brillouin suscitent un très grand intérêt pour leur capacité à produire des largeurs de raie très fines (de l'ordre du Hz-kHz ; lasers ultra-cohérents).

Cette thèse est consacrée à la compréhension des lasers à fibre Brillouin en anneau, fonctionnant avec plusieurs ordres de Stokes. Mon travail a été réalisé dans le cadre du projet SOLBO (SOurces Laser Brillouin cOhérent à faible bruit) de l'appel FUI (Fonds Unique Interministériel AAP20) avec l'aide de BPI France, le cluster "Images et réseaux" et en collaboration avec IDIL Fibre Optiques (chef de projet), Lumibird, THALES, ISCR (Institut des Sciences Chimiques de Rennes), Photonics Bretagne.
L'objectif principal était de concevoir un laser à fibre Brillouin à faible coût, avec une largeur de raie intégrée inférieure au kHz, par IDIL. Pour l'Instiut Foton, l'objectif était d'explorer la physique des lasers à fibre multi-Stokes Brillouin et d'essayer de connaître les limites fondamentales la réduction du bruit de fréquence pour ces sources, que ce soit pour des cavités avec un seul ordre Stokes simples ou avec plusieurs ordres Stokes. Dans cette thèse, je propose:

- une nouvelle technique de mesure de gain Brillouin, particulièrement adaptée aux cavités courtes et ne nécessitant pas de fortes puissances de pompage optique (quelques dizaines de milliWatts),

- une comparaison du fonctionnement du laser entre le pompage résonnant et non

résonnant,

- une modélisation de nos résultats expérimentaux par une approche analytique, permettant d'expliquer les mécanismes physiques de ces lasers,

- une discussion sur les limitations fondamentales de ces appareils et leurs avantages.

Le premier chapitre de ce manuscrit présente des généralités sur le bruit laser. Le bruit d'intensité relatif (RIN : Relative Intensity Noise) des lasers est théoriquement expliqué et mesuré expérimentalement à l'aide d'un laser DFB commercial (KOHERAS). De plus, le bruit de fréquence des lasers est expliqué et lié à la largeur de raie du laser. Une illustration est donnée grâce à un laser accordable (Tunics OM) et la largeur de ligne est mesurée en utilisant la technique dite $\beta - line$, qui est comparée à une technique auto-hétérodyne. Une caractérisation importante de ces qualifications de bruit est l'évaluation du bruit de fond du banc et son analyse. Cette analyse a été réalisée en utilisant différentes longueurs de retard dans l'interféromètre, qui est utilisé comme convertisseur d'intensité pour les fluctuations de fréquence. Cela a été discuté en détail. De plus, afin d'obtenir une stabilité à long terme (de l'ordre de quelques heures) et afin de faciliter nos mesures, nous avons démontré la stabilisation d'un laser sur un résonateur à fibre optique en utilisant la technique Pound-Drever-Hall (PDH) . Cette technique nous a permis de réduire la largeur intégrée de raie du laser de 203 kHz à 2 kHz.

Dans le deuxième chapitre, nous avons présenté une introduction générale des diffusions de Brillouin spontanées et stimulées. Nous avons discuté et mesuré les paramètres clés des diffusions de Brillouin, qui sont la largeur de bande de gain, le décalage de fréquence et le coefficient de gain de Brillouin (gain maximum). Une nouvelle méthode de caractérisation du gain de Brillouin basée sur la méthode de *cavity ring down* (CRDM) a été introduite. La caractérisation de la cavité à l'aide du CRDM, permet d'identifier le régime de couplage et les pertes intracavités du résonateur , soient le taux de couplage entre le coupleur et la cavité ainsi que les pertes linéiques intra-cavité. Ces mesures sont importantes car elles donnent directement accès aux paramètres utilisés dans notre modèle théorique. Enfin, nous avons montré que le coefficient de gain de Brillouin estimé à l'aide du CRDM est en bon accord avec les résultats obtenus par des méthodes standard (nous avons vérifié avec la méthode auto-hétérodyne). La méthode CRDM offre la possi-

bilité d'obtenir les paramètres de gain matériau (il s'agit du paramètre de gain matériau effectif correspondant aux modes acoustiques des fibres standard (SMF28)) et de cavité, en une seule expérience, en utilisant des puissances de pompe optique de l'ordre de quelques à dizaines de milliWatts, pour des cavités de faible longueur (mètre, millimètre, micromètre). C'est un intérêt significatif par rapport à d'autres méthodes.

Dans le troisième chapitre, nous avons passé en revue le développement du laser Brillouin au cours des dernières décennies. Cela va du laser en anneau à fibre aux lasers Brillouin intégrés à puce. Après avoir expliqué la différence entre un laser Brillouin sous pompage résonant et non résonant, le caractère, le caractère monomode ou multimode du fonctionnement du laser Brillouin est expliqué. Les sauts de modes (longitudinaux de la cavité) du laser Brillouin non résonant sont illustrés à l'aide d'une cavité Brillouin de 20 mètres. Nous montrons la suppression de ces sauts de mode à l'aide d'une technique de verrouillage PDH. Cela nous a permis d'obtenir un laser Brillouin non résonnant avec une stabilité à long terme de plusieurs heures. De plus, nous sommes en mesure de contrôler des paramètres clés tels que les facteurs de cavité (facteur Q, pertes de couplage, pertes internes), le désaccord entre la résonance de Stokes laser et le gain maximum (ou de manière équivalente le décalage Brillouin), le bruit de la pompe. Toutes ces améliorations nous ont permis d'avoir un contrôle fin du laser, et de faire une comparaison qualitative et quantitative entre les modèles et les résulats expérimentaux. L'analyse de ce troisième chapitre est réalisée à l'aide d'un modèle standard de transfert de bruit pour les lasers Brillouin non résonants. Nous avons démontré que notre système peut atteindre une largeur de raie intrinsèque de 1,3 Hz avec une réduction de 37 ± 1 dB par rapport à la largeur de raie du laser de la pompe. De plus, nous avons également montré que la largeur de raie intrinsèque du laser Brillouin peut atteindre le niveau de mHz en cascadant deux lasers Brillouin non résonants.

Dans le dernier chapitre, la dynamique du bruit du laser Brillouin résonnant est étudiée expérimentalement à l'aide d'une cavité en anneau de fibre. Un modèle généralisé aux lasers Brillouin multi-Stokes a été développé à l'Institut Foton; Nous avons montré que nos mesures expérimentales sont en bon accord avec les simulations numériques pour le laser Brillouin. Le RIN des lasers Brillouin à plusieurs ordres multi-Stokes a ensuite été étudié expérimentalement et numériquement en termes de puissance de pompage, de durée de vie des photons et de désaccord de gain. Nous avons confirmé que dans le régime que nous appelons en cascade et correspondant au fonctionnement avec plusieurs ordres

de Stokes, et pour certaines gammes de fréquences, le RIN peut être réduit par rapport aux régimes monomodes de façon très significative ($\sim$ 40 dB). Cette réduction est due à la saturation de la puissance de la pompe intracavité due au processus laser.

La durée de vie de la cavité photonique change principalement la fréquence de relaxation du laser Brillouin multi-Stokes.

Le désaccord entre la résonance de Stokes laser et le maximum de gain de Brillouin a une grande influence sur la réponse du RIN, même pour de petites valeurs de désaccord ($\sim$ environ 100 kHz). Nous détaillons théoriquement et expérimentalement l'augmentation de RIN par l'influence du désaccord de gain.

Enfin, nous avons tenté d'explorer les limites de la réduction du bruit de fréquence à l'aide de deux lasers Brillouin. Nous avons montré qu'il est possible de mettre en cascade la réduction fréquence-bruit en cascadant deux lasers Brillouin. Cependant notre plancher de bruit de banc est rapidement atteint et nous a empêché d'explorer expérimentalement toute limitation de réduction du bruit même si le bruit thermique sera en tout cas une limitation fondamentale. Néanmoins, une largeur de ligne intrinsèque de l'ordre de 100 mHz est facile à obtenir dans une configuration mono-Stokes ou dans une configuration multi-Stokes.

D'autres techniques sont actuellement explorées pour surmonter les limites de bruit de fond de nos bancs de mesure de bruit de fréquence afin de nous permettre d'atteindre les limites fondamentales de réduction du bruit pour la largeur de raie intrinsèque. Il va de soi que le bruit basse fréquence (bruit de scintillement, marche aléatoire) associé aux fluctuations thermiques et mécaniques nécessite un asservissement sur une référence métrologique pour obtenir de petites largeurs de raie intégrées. Nous avons réussi à atteindre la largeur de raie intégrée en kHz en utilisant, comme référence, la fréquence de résonance d'un interféromètre à fibres.

Cependant, nous avons souligné qu'il existe des limitations fondamentales pour les lasers Brillouins avec plusieurs ordres de Stokes. Nous avons démontré expérimentalement, en accord avec des prédictions théoriques montrant la pénalité causée par les ondes anti-Stokes, qu'une dégradation du bruit de fréquence est observée. Cela peut être abaissé en opérant loin du seuil de l'ordre de Stokes analysé.

De plus, le décalage de Brillouin dépend de l'ordre de Stokes car son décalage de fréquence dépend de la longueur d'onde. Cela générera un désaccord inhérent lorsque l'ordre de Stokes est augmenté. Comme le montre précisément cette thèse, ce désaccord

dégrade le RIN et le bruit de fréquence par couplage amplitude-phase au sein du processus non linéaire. Il s'avère que c'est une limitation sévère pour les lasers Brillouin avec plusieurs ordres de Stokes, car un petit désaccord (moins de 1 MHz) affectera à la fois le RIN et le bruit de fréquence.

Nous soulignons le fait que de nombreuses caractéristiques du bruit de fréquence sont liées aux propriétés RIN par un couplage entre intensité et phase.

Nous montrons que le processus en cascade modifie la dynamique du laser Brillouin par rapport à celles d'un laser Brillouin monomode avec une seule composante de Stokes du premier ordre. Nos résultats expérimentaux sont en excellent accord avec nos simulations numériques, obtenues grâce à notre système non linéaire décrivant le fonctionnement d'un laser Brillouin multi-Stokes. Ce bon accord est principalement dû à notre capacité à :

- obtenir des valeurs très précises des paramètres de la cavité et du coefficient de gain Brillouin en utilisant la technique CRDM ;
- atteindre une stabilité à long terme (plusieurs dizaines d'heures) ;
- contrôler finement le désaccord entre la résonance de Stokes du laser et la fréquence du maximum de gain Brillouin.

Nous démontrons expérimentalement pour la première fois que le bruit de fréquence est dégradé en présence de diffusion anti-Stokes Brillouin.

Nous montrons également qu'un désaccord de gain de l'ordre de quelques centaines de kHz peut dégrader la réduction du bruit d'intensité ou encore augmenter la largeur de raie par couplage amplitude-phase.

Toutes ces observations très fines permettent ainsi de fixer les limites fondamentales de tels systèmes laser telles que : l'augmentation du bruit due aux ordres anti-Stokes ; le rôle du bruit de la pompe et son éventuelle corrélation avec la finesse de la cavité ; l'effet du désaccord inhérent aux ordres de Stokes supérieurs.

Toutes ces conclusions sont essentielles à la conception et à l'ingénierie de ces lasers à fibre Brillouin, qui suscitent actuellement beaucoup d'intérêt comme en témoignent les travaux en cours dans la communauté scientifique.

Cette thèse contribue à une meilleure compréhension des lasers Brillouin multi-Stokes.